

**TECHNIQUES FOR ENHANCING WIND ENERGY GENERATION
-A CFD BASED MULTIBODY DYNAMICS APPROACH IN
HORIZONTAL AXIS WIND TURBINES**

Thesis submitted to

COCHIN UNIVERSITY OF SCIENCE AND TECHNOLOGY

in partial fulfillment of the requirements for the degree of

DOCTOR OF PHILOSOPHY

By

RAJENDRAN.C

(Reg.No: 3184)

Under the Supervision of

Prof.(Dr.) G.MADHU

DIVISION OF SAFETY AND FIRE ENGINEERING

SCHOOL OF ENGINEERING

COCHIN UNIVERSITY OF SCIENCE AND TECHNOLOGY

KOCHI – 22, KERALA, INDIA

September 2011

**TECHNIQUES FOR ENHANCING WIND ENERGY GENERATION –A CFD
BASED MULTIBODY DYNAMICS APPROACH IN HORIZONTAL AXIS
WIND TURBINES**

Ph.D Thesis

Author :

Rajendran. C
*Division of Safety and Fire Engineering
School of Engineering
Cochin University of Science and Technology
Kochi-682022, Kerala, India
Email :rajpcra@gmail.com*

Supervisor :

Prof. (Dr.) G.Madhu
*Professor and Head
Division of Safety and Fire Engineering
School of Engineering
Cochin University of Science and Technology
Kochi-682022, Kerala, India
E-Mail : profmadhu@rediffmail.com*

September 2011

Dedicated to
My Parents

Ref. No.

Date:

Certificate

This is to certify that the thesis entitled “**TECHNIQUES FOR ENHANCING WIND ENERGY GENERATION –A CFD BASED MULTIBODY DYNAMICS APPROACH IN HORIZONTAL AXIS WIND TURBINES**” is an authentic original work done by Rajendran.C under my supervision and guidance in School of Engineering, Cochin University of Science and Technology. No part of this thesis has been presented for any other degree from any other institution.

Prof. (Dr.) G.MADHU
Supervising Guide

DECLARATION

I hereby declare that the work presented in the thesis entitled **“TECHNIQUES FOR ENHANCING WIND ENERGY GENERATION –A CFD BASED MULTIBODY DYNAMICS APPROACH IN HORIZONTAL AXIS WIND TURBINES ”** is based on the original work done by me under the supervision of Prof. (Dr.) G. MADHU, Division of Safety and Fire Engineering, School of Engineering, Cochin University of Science and Technology. No part of this thesis has been presented for any other degree from any other institution.

Kochi-22

29th September 2011

RAJENDRAN.C

Acknowledgment

I pay my obeisance to the Almighty for having bestowed with an opportunity of being guided by Dr. G.Madhu, Professor and Head, Division of Safety and Fire Engineering, School of Engineering, Cochin University of Science and Technology, Kochi, Kerala. I feel highly elated in expressing my deep sense of gratitude for his eminent and adroit guidance with sustained interest, learned counsel, scintillating suggestions, benevolent and noble ideas, inestimable patience, cordiality and constant encouragement throughout the study period. His adorable patience in correcting my thesis is an example for the attitude of a good teacher, which I like to carry forward in my career. I wish to record my thanks to Professor Madhu for the freedom he has given me in carrying out the research work.

I am profoundly indebted to Professor Dr. P.S.Tide, Division of Mechanical Engineering, School of Engineering, Cochin University of Science and Technology for teaching me the techniques of CFD. His simple but elegant explanations on the intricacies of CFD helped me a lot in completing this piece of research. His valuable suggestions, encouragement and blessings always motivated me to move forward. I sincerely express my deep sense of gratitude and heartfelt thanks to him.

It is also my duty to express my sincere thanks to Dr.V.N. Narayanan Namboothiri, Head, Division of Mechanical Engineering, School of Engineering, Cochin University of Science and Technology and Doctoral committee member for his encouragement and support. My sincere thanks are due to the faculty members of the Division of

Safety and Fire engineering and Division of Mechanical Engineering for their encouragement throughout my research period.

*On my personal note my heartfelt thanks to my loving **Mother** and **Father** for showering mountains of love on me and who always stood by me in every step of my life. I thank the Lord Almighty for His divine mercy and ever enduring support throughout the course of my study.*

I am indebted to my loving wife Nandhini, daughters Tharani and Sasmitha for their affection, encouragement and prayers.

Rajendran.C

ABSTRACT

Wind energy has emerged as a major sustainable source of energy. The efficiency of wind power generation by wind mills has improved a lot during the last three decades. There is still further scope for maximising the conversion of wind energy into mechanical energy. In this context, the wind turbine rotor dynamics has great significance.

The present work aims at a comprehensive study of the Horizontal Axis Wind Turbine (HAWT) aerodynamics by numerically solving the fluid dynamic equations with the help of a finite-volume Navier–Stokes CFD solver. As a more general goal, the study aims at proving the capabilities of modern numerical techniques for the complex fluid dynamic problems of HAWT. The main purpose is hence to maximize the physics of power extraction by wind turbines.

This research demonstrates the potential of an incompressible Navier–Stokes CFD method for the aerodynamic power performance analysis of horizontal axis wind turbine. The National Renewable Energy Laboratory USA-NREL (Technical Report NREL/CP-500-28589) had carried out an experimental work aimed at the real time performance prediction of horizontal axis wind turbine.

In addition to a comparison between the results reported by NREL made and CFD simulations, comparisons are made for the local flow angle at several stations ahead of the wind turbine blades. The comparison has shown that fairly good predictions can be made for pressure distribution and torque. Subsequently, the wind-field effects on the blade aerodynamics, as well as the blade/tower interaction, were investigated. The selected case corresponded to a 12.5 m/s up-wind HAWT at zero degree of yaw angle and a rotational speed of

25 rpm. The results obtained suggest that the present method can cope well with the flows encountered around wind turbines. The aerodynamic performance of the turbine and the flow details near and off the turbine blades and tower can be analysed using these results.

The aerodynamic performance of airfoils differs from one another. The performance mainly depends on co-efficient of performance, co-efficient of lift, co-efficient of drag, velocity of fluid and angle of attack. This study shows that the velocity is not constant for all angles of attack of different airfoils. The performance parameters are calculated analytically and are compared with the standardized performance tests. For different angles of attack, the velocity stall is determined for the better performance of a system with respect to velocity.

The research addresses the effect of surface roughness factor on the blade surface at various sections. The numerical results were found to be in agreement with the experimental data.

A relative advantage of the theoretical aerofoil design method is that it allows many different concepts to be explored economically. Such efforts are generally impractical in wind tunnels because of time and money constraints. Thus, the need for a theoretical aerofoil design method is threefold: first, for the design of aerofoil that fall outside the range of applicability of existing catalogs; second, for the design of aerofoil that more exactly match the requirements of the intended application; and third, for the economic exploration of many aerofoil concepts. From the results obtained for the different aerofoils, the velocity is not constant for all angles of attack. The results obtained for the aerofoil mainly depend on angle of attack and velocity.

The vortex generator technique was meticulously studied with the formulation of the specification for the right angle shaped vortex generators-

VG. The results were validated in accordance with the primary analysis phase. The results were found to be in good agreement with the power curve. The introduction of correct size VGs at appropriate locations over the blades of the selected HAWT was found to increase the power generation by about 4 %.

Key words: Horizontal Axis Wind Turbines, Aerodynamics Aerofoil, Computational Fluid Dynamics CFD, Angle of Attack, Power Generation.

LIST OF SYMBOLS

a	-	Axial interference factor
A	-	Area of the circle swept by the rotor
a'	-	Rotational interference factor
B	-	Number of blades
BEM	-	Blade Element Momentum
C	-	Chord length of the local blade section
C_d	-	Coefficient of drag
CFD	-	Computerized Fluid Dynamics
CFL	-	Courant-Friedrich-Levy number
CFU	-	Common flow up
C_l	-	Coefficient of lift
C_P	-	Power coefficient
C_T	-	Thrust coefficient
D	-	Drag force acting on the airfoil
DES	-	Detached eddy simulations
DES	-	Detached Eddy Simulations
DFIG	-	Doubly Fed Induction Generator
E	-	Kinetic energy of an air mass
e	-	Kinetic energy for unit mass
FEA	-	Finite element analysis
FEM	-	Finite element method

FVM	-	Finite volume method
H/D	-	Tower-height/Rotor-diameter ratio
HAWT	-	Horizontal Axis Wind Turbine
kW	-	kilo Watt
L	-	Lift force acting on the airfoil
LES	-	Large Eddy Simulation
m	-	Air mass
MRF	-	Multiple Rotating Frames
NLF	-	Natural laminar flow
NREL	-	National Renewable Energy Laboratory
NS	-	Navier Stokes
P	-	Rated power
P_0	-	Instantaneous power
PIV	-	Particle image velocimetry
PIV	-	Particle image velocimetry
PMSG	-	Permanent Magnet Synchronous Generator
Q	-	Heat Energy
R	-	Radius of the blades
RANS	-	Reynolds Averaged Navier Stokes
SCIG	-	Squirrel Cage Induction Generator
SRF	-	Single Reference Frame
SST	-	Shear stress transport

T	-	Integral Thrust force acting on the rotor
U	-	Free stream velocity
U_{∞}	-	Undisturbed wind speed
V	-	Wind velocity
V_0	-	Mean wind speed
VAWT	-	Vertical Axis Wind turbine
W	-	Work done
$W(x)$	-	Induced velocity
\dot{m}	-	Mass flow
ρ	-	Air density
Δt	-	Time step
λ	-	Tip speed ratio
Σ	-	Turbine solidity
Ω	-	Angular velocity
ωR	-	Tip-speed
$\dot{\Gamma}$	-	Vortex strength around the airfoil

Contents

Chapter 1 INTRODUCTION	1-10
1.1 The Current Wind Energy Scenario	1
1.2 Motivation and Objectives of the Research	5
1.3 Overview of the Thesis	9
Chapter 2 WIND TURBINE FUNCTIONING AND THEIR AERODYNAMICS	11-30
2.1 Wind Power Technology	11
2.2 Functioning of HAWT	12
2.3 A Brief Review of the Aerodynamic Models	17
2.3.1 Basic Definitions	18
2.3.2 The BEM Method	23
2.3.3 Lifting Line, Panel and Vortex Methods	24
2.3.4 Actuator Disk Method	26
2.3.5 Navier-Stokes Solvers	27
2.4 Literature Review on Aerodynamics	29
Chapter 3 CFD AND WIND TURBINES	31-37
3.1 CFD Governing Equations	31
3.1.1 Lagrangian Description	31
3.1.2 Eulerian Description	32
3.1.3 Continuity Equation	32
3.1.4 Momentum Equation	33
3.1.5 Navier-Stokes Equation	33
3.2 Solution Procedure	35

3.2.1 Segregated Solution Procedure	35
3.2.2 Coupled Solution Procedure	35
3.3 Rotating Reference Frames	36
3.4 Post-Processing	36
3.5 LES and DES Approach	37
Chapter 4 CFD COMPUTATIONS FOR VALIDATION OF PERFORMANCE OF HAWT	39-86
4.1 Introduction	39
4.2 Assumptions Made	39
4.3 Blade Modeling	41
4.4 Discretization of Volumes	51
4.5 Multiple Rotating Frames	52
4.6 Boundary Conditions	54
4.6.1 Wall Boundaries	54
4.6.2 Solution Methods	55
4.6.3 Turbulence Model	56
4.7 Power calculation	57
4.8 Validation of CFD Approach for HAWT Analysis	58
4.9 Studies on HAWT Using CFD	59
4.10 CFD results Validation	63
4.11 Results and Discussion	65
4.12 Conclusions	84
4.13 Necessity for further techniques.	86

Chapter 5 EFFECT OF SURFACE ROUGHNESS ON PERFORMANCE OF WIND TURBINE.....	87-105
5.1 Introduction	87
5.2 Studies on Roughness	88
5.3 Methodology	91
5.4 Results & Discussion	95
5.5 Conclusions	104
Chapter 6 EFFECT OF GURNEY FLAPS AND WINGLETS ON THE PERFORMANCE OF THE HAWT	107-126
6.1 Introduction	107
6.2 Studies on Gurney Flaps and Winglets	108
6.3 Methodology	116
6.4 Results and Discussion	116
6.4.1 Effect of gurney flap	124
6.4.2 Effect of winglets.	125
6.5 Conclusions	126
Chapter 7 EFFECT OF VORTEX GENERATORS ON THE PERFORMANCE OF THE HAWT	127-159
7.1 Introduction	127
7.2 Problem Definition	128
7.3 Studies on Vortex Generators	129
7.4 Wind Turbine Blade Modeling	135
7.5 Design of Experiments	135
7.6 Localized Flow Separation of the Wind over the Blade Surface	137

7.7 Mathematical Model	141
7.8 Modeling of Blade with VG	144
7.9 CFD Analysis of HAWT Model with VGs	146
7.10 Results & Discussion	147
7.10.1 Comparison Study	157
7.12 Conclusions	159
Chapter 8 SUMMARY AND CONCLUSIONS	161-166
8.1 Summary	161
8.2 Conclusions	163
8.3 Scope for Future Research	165
REFERENCES	167-181
LIST OF PUBLICATIONS	
CURRICULUM VITAE	

LIST OF TABLES

Table 4.1	Co-ordinate values of airfoil S 816.....	42
Table — 4.1 (a)	Co-ordinate values of airfoil S 817	43
Table — 4.1 (b)	Co-ordinate values of airfoil S 818	44
Table 4.2	Blade details at various sections	45
Table 4.3	Pressure moment, viscous moment.....	58
Table 4.4	Pressure moment and viscous moment	65
Table 4.5	Comparison of Power generation.....	82
Table 4.6	Moments generated by the three Blades	83
Table 5.1	Various surface parts of the three Blades	93
Table 5.2	Area of seperated surface zones	94
Table 5.3	Comparison of pressure moment.....	96
Table 5.4	Comparison of viscous moment.....	99
Table 5.5	Comparisons of total moment generated by different rough surfaces.....	103
Table 6.1	Various moments generated by three blades with gurney flaps	117
Table 6.2	Various moments generated by three blades without gurney flaps.....	117
Table 6.3	Moments generated by three blades without winglets on Y axis	124
Table 6.4	Moments generated by three blades with winglets on Y axis.....	125
Table-7.1	Design of experiments —Combination	136
Table 7.2	Boundary Layer Separation values at various points.....	138
Table 7.3	Configuration of Vortex generator at various section of the Blade.....	140
Table 7.4	Moments generated by three blades with VG.....	153
Table 7.5	Moment generated by the three blades without VG.....	153
Table 7.6	Comparison of the moments generated.....	157
Table 7.7	Moments generated by the three blades	158

LIST OF FIGURES

Figure 1.1	Top ten cumulative wind power capacities as in December 2010.....	2
Figure 1.2	Top ten cumulative wind power capacities installed during January to December 2010.....	3
Figure 1.3	Global Cumulative Wind Power.....	4
Figure 1.4	Indian Cumulative Wind Power.....	5
Figure 2.1	Principle of wind energy.....	11
Figure 2.2	Relative velocity concepts.....	20
Figure 2.3	BEM annular control volumes.....	22
Figure 2.4	Wind power distributions.....	28
Figure 3.1	Lagrangian Description.....	32
Figure 3.2	Eulerian Description.....	32
Figure 3.3	Segregated Solution Procedures.....	35
Figure 4.1	Methodology for CFD analysis of HAWT.....	40
Figure 4.2	Profile of S816, S817 & S818 airfoil.....	41
Figure 4.3	Modeling the airfoils of the blade.....	46
Figure 4.4	Lofting of the airfoil sections.....	46
Figure 4.5	Blades modeling with suction and pressure sides.....	47
Figure 4.6	Assembly of blade and hub.....	48
Figure 4.7	Assembly constraints cone angle, tilt angle.....	48
Figure 4.8	Complete model of windmill.....	49
Figure 4.9	Discretization of parts of the HAWT.....	50
Figure 4.10	Cylindrical domains.....	51
Figure 4.11	Cubical domains.....	51
Figure 4.12	Location of wind turbine in the computational domain.....	52
Figure 4.13	Volume zones for analysis.....	53
Figure 4.14	MRF zone in the assembly of HAWT.....	54
Figure 4.15	Iteration statuses with convergence.....	55
Figure 4.16	Cross sectional view of the domain of analysis.....	56

Figure 4.17	Pressure vector contour.....	65
Figure 4.18	Velocity vector contour	66
Figure 4.19	Velocity vector contour along with Tower.....	66
Figure 4.20	Velocity vector contour along with Tower —sweep surface —Z direction	67
Figure 4.21	Velocity vector contour along with Tower —sweep surface —Y plane.....	68
Figure 4.22	Pressure vector contours of the three blades along with sweep surface in Z direction.....	69
Figure 4.23	Pressure vector contours of the three blades along with Tower —sweep surface in Z direction.....	69
Figure 4.24	Velocity vectors around the tower.....	70
Figure 4.25	Static pressure on the tower surface viewed from -Y direction.....	70
Figure 4.26	Static pressure on the tower surface viewed from X direction.....	71
Figure 4.27	Static pressure contour over the three blades viewed from the outlet side.....	71
Figure 4.28	Static pressure contour over the three blades viewed from air flow direction.....	72
Figure 4.29	Static pressure contour over the entire wind turbine viewed from air flow direction.....	73
Figure 4.30	Turbulence intensity.....	73
Figure 4.31	Contour velocity magnitude over the entire wind blades viewed from air flow direction.....	74
Figure 4.32	Contour velocity magnitude over the entire wind turbine viewed from air flow direction.....	75
Figure 4.33	Velocity vectors around the middle section of blade.....	76
Figure 4.34	Velocity vectors around the tip section of blade.....	77
Figure 4.35	Velocity vectors around the root section of blade.....	78
Figure 4.36	Raw data of power measurements	80
Figure 4.37	Power curve uncertainty contributions	80
Figure 4.38	Power curve of Zond 50 HAWT.....	81

Figure 4.39	Pressure and viscous moments generated by each blade.....	83
Figure 5.1	Blade A' s pressure side middle part surface.....	91
Figure 5.2	Blade A' s pressure side root part surface.....	91
Figure 5.3	Blade A' s pressure side part surface.....	92
Figure 5.4	Blade A' s pressure side tip part surface.....	92
Figure 5.5	Blade B in the HAWT assembly.....	92
Figure 5.6	Blade C in the HAWT assembly.....	93
Figure 5.7	Moments generated by various surfaces of blades in Y axis	95
Figure 5.8	Pressure moments generated by Blade-A-psm, Blade-A-ssm and Blade-B- psm, Blade-B-ssm for different surface roughness heights.....	97
Figure 5.9	Pressure moments generated by Blade-A-pst, Blade-A-sst and Blade-B- pst, Blade-B-sst for different surface roughness heights.....	97
Figure 5.10	Pressure moments generated by Blade-A-psr, Blade-A-ssr and Blade-B- psr, Blade-B-ssr for different surface roughness heights	97
Figure 5.11	Pressure moments generated by Blade-C-psm, Blade-C-ssm and Blade-C- pst, Blade-C-sst for different surface roughness heights.....	98
Figure 5.12	Pressure moments generated by Blade-C-psr, and Blade-C-ssr for different surface roughness heights.....	98
Figure 5.13	Viscous moments generated by Blade-A-psm, Blade-A-ssm and Blade-B- psm, Blade-B-ssm for different surface roughness heights.....	100
Figure 5.14	Viscous moments generated by Blade-A-pst, Blade-A-sst and Blade-B-pst, Blade-B-sst for different surface roughness heights.....	101
Figure 5.15	Viscous moments generated by Blade-A-psr, Blade-A-ssr and Blade-B- psr, Blade-B-ssr for different surface roughness heights.	102
Figure 5.16	Viscous moments generated by Blade-C-sst, Blade-C-pst and Blade-C- ssm, Blade-C-psm for different surface roughness heights.....	102
Figure 5.17	Viscous moments generated by Blade-C-psr, and Blade-C-ssr for different surface roughness height	102

Figure 5.18	Comparison of total moments generated by various surfaces of blades in Y axis.....	104
Figure 6.1	Flap at the trailing edge.....	116
Figure 6.2	Contours of static pressure	118
Figure 6.3	Contours dynamic pressures	118
Figure 6.4	Contours of velocity magnitude over the three blades with gurney flaps.	119
Figure 6.5	Velocity vectors colored by velocity magnitude (without tower).....	119
Figure 6.6	Contours of velocity magnitude	120
Figure 6.7	Velocity vectors colored by dynamic pressure	120
Figure 6.8	Velocity vectors colored by velocity magnitude (with tower).....	121
Figure 6.9	Blade with winglet at the tip	121
Figure 6.10	Blades with winglet at the tips on HAWT.....	122
Figure 6.11	Static pressure contour over entire assembly of HAWT with winglets.....	122
Figure 6.12	Velocity magnitude contour over entire assembly.....	123
Figure 6.13	Moments generated on Y axis by three blades without winglets.....	124
Figure 6.14	Moments generated on Y axis by three blades with winglet	125
Figure 7.1	Comparison of airfoil with & without vortex generators.	128
Figure 7.2	Flow Separation graph on airfoil.....	137
Figure 7.3	Configuration of Vortex generator	139
Figure 7.4	Methodology for developing the model	141
Figure 7.5	Airfoil curve extracted in LABFIT.....	142
Figure 7.6	Curve equations in LABFIT.....	142
Figure 7.7	Construction of Vortex generator	144
Figure 7.8	Array of VG on single blade.....	145
Figure 7.9	Array of VG on the Single blade at various sections	145
Figure 7.10	Meshing of the Blade.....	146
Figure 7.11	Iterations residuals.....	146
Figure 7.12	Velocity contour plots on the blades.....	147
Figure 7.13	Pressure contour plots.....	148

Figure 7.14	Velocity vector plot over the blades viewed from inlet.....	148
Figure 7.15	Velocity vector plot by sweep surface along X direction.....	149
Figure 7.16	Velocity vector plot by sweep surface along Y direction.....	150
Figure 7.17	Total Pressure plot by sweep surface along Y direction.....	151
Figure 7.18	Turbulence plot by sweep surface along X direction.	152
Figure 7.19	Pressure contour on the blade surfaces.....	154
Figure 7.20	Velocity contour with sweep surface in X axis.....	155
Figure 7.21	Pressure contour with sweep surface in X axis.....	155
Figure 7.22	Velocity vector plot over the blades viewed from outlet.....	156
Figure 7.23	Turbulence plot of wake region	156
Figure 7.24	Moments generated by the three blades without VGs.....	157
Figure 7.25	Pressure moment and viscous moment generated by the three blades with VGs.....	158
Figure 7.26	The comparison of pressure and viscous moments generated.	159

1.1 The Current Wind Energy Scenario

The Indian wind energy sector has an installed capacity of 14158 MW (as on March 31, 2011). In terms of wind power installed capacity, India is ranked as 5th in the World (<http://www.gwec.net>). Today India is a major player in the global wind energy market. The potential is far from exhausted. Indian Wind Energy Association has estimated that with the current level of technology, the ‘on-shore’ potential for utilization of wind energy for electricity generation is of the order of 65,000 MW. The unexploited resource availability has the potential to sustain the growth of wind energy sector in India in the years to come. International Wind Energy Association (IWEA) helps the industry in realizing this potential quickly and efficiently.

Figure 1.1 shows the top ten cumulative windmill installed capacities among the entire world countries as in December 2010

The motivation to carry out the present research originated from the fact that few wind mill manufacturers have a strong research and development back up.

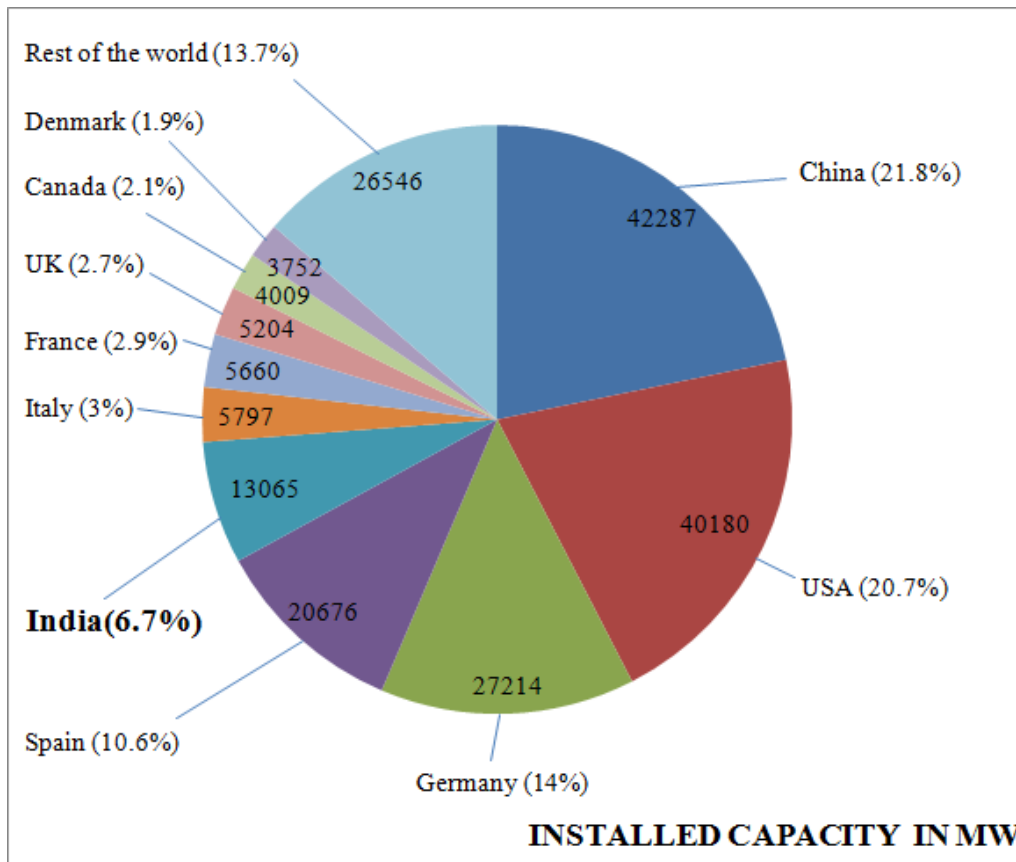


Figure 1.1 Top ten cumulative wind power capacities as in December 2010 (Source: IWEA & AWEA)

At the end of 2010, China was on top for the first time in history with 21.8 % of the world's cumulative wind power generation capacity. In the second place is previous year's number one, the United States with 20.7 % of the world's cumulative capacity. India is in the fifth place with 13,065 MW, 6.7 % of the world's cumulative capacity. Also in 2010 the majority of the new wind mills were put up in China. More than 45 % of the world's new wind mill capacity was installed in China, whereas 6.0 % of the new capacity was put up in India ranking third among the entire world (<http://www.gwec.net>).

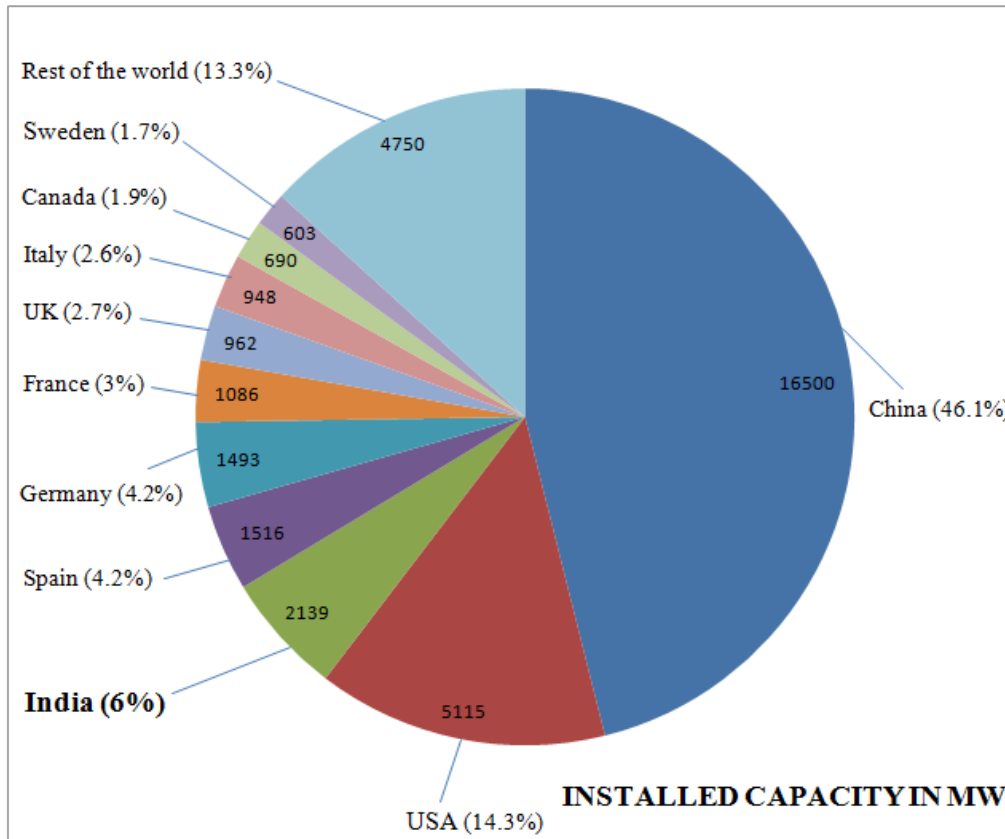


Figure 1.2 Top ten cumulative wind power capacities installed during January to December 2010 (Source: IWEA & AWEA)

Electricity demand in India has continuously outstripped production, and a peak energy shortage of around 12.7 % prevailed in 2009-2010 (<http://www.mnre.gov.in>). To meet this shortfall as well as the National Electricity policy target of ‘Electricity for all by 2012’ the cleanest electricity generation options available to India are Renewable Energy Technologies (RETS) (<http://economictimes.indiatimes.com>). To meet the target of electricity for all by 2012, renewable energy options including wind power will have to play a crucial role in India’s emerging energy mix (<http://www.ewea.org>). Not

only they are environmentally sound but also their project gestation periods are significantly shorter than those for thermal or nuclear power plants.

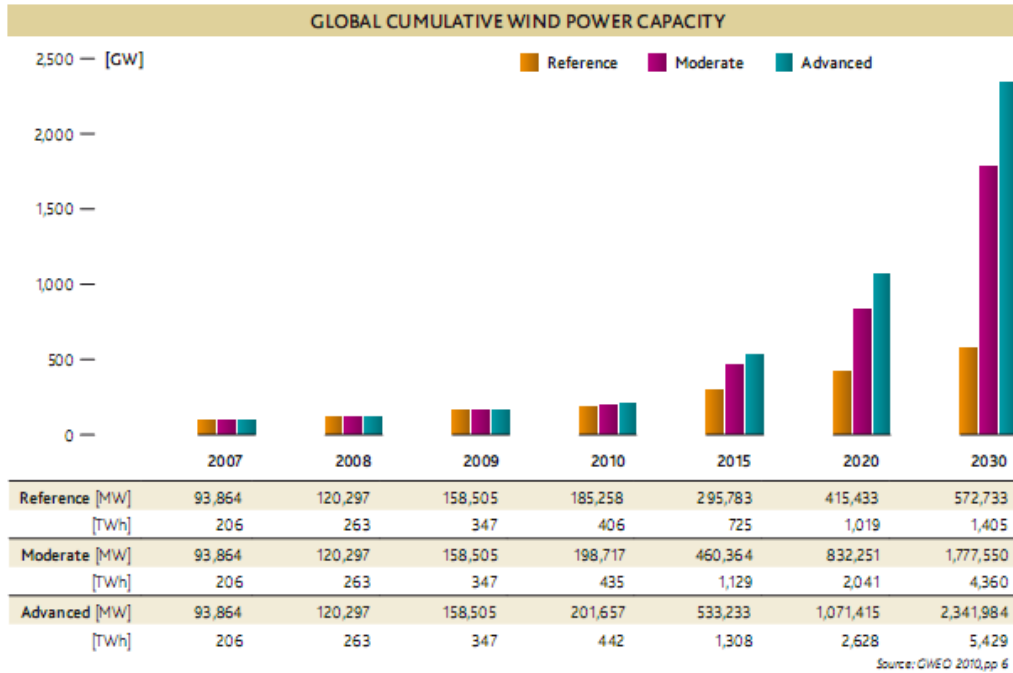


Figure 1.3 Global Cumulative Wind Power (Source: GWEC, 2010)

According to the Indian Ministry of New and Renewable Energy (MNRE) today, the share of renewable based capacity is 10.9% (excluding large hydro) of the total installed capacity of 170 GW in the country, up from 2% at the start of the 10th plan period (2002-2007). This includes 13,065.78 MW of wind, 2,939 MW of small hydro power, 1,562 MW of (bagasse based) co-generation, 997 MW of biomass, 73.46 MW of ‘waste to power’ and 17.80 MW of solar PV for grid connected renewable energy at the end of 2010 (<http://economictimes.indiatimes.com>).

There are several published scenarios that examine the future role of wind power globally as a part of the necessary energy system overhaul towards a clean energy future. The Global Wind Energy Council (GWEC) developed its

strategies in collaboration with green peace international and the German aerospace centre (<http://www.gwec.net>).

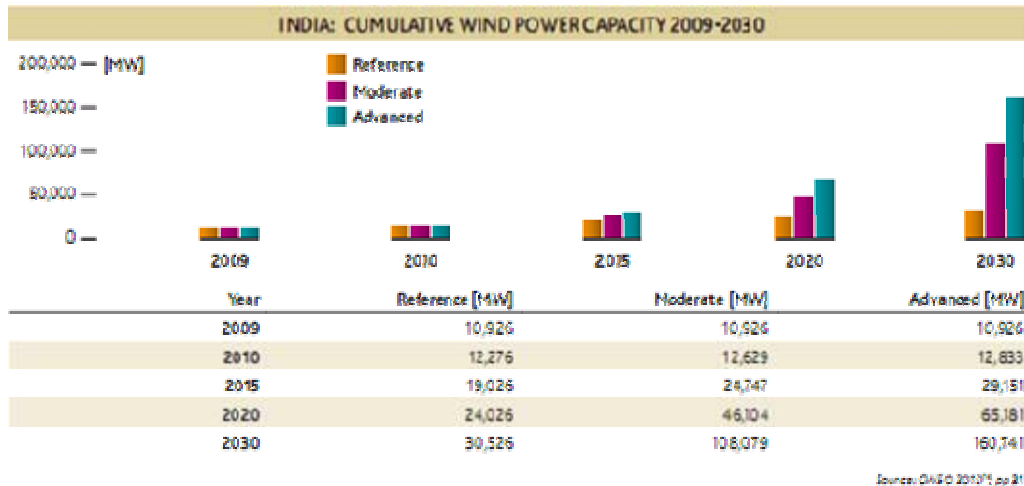


Figure 1.4 Indian Cumulative Wind Power (*Source: GWEO 2010*)

1.2 Motivation and Objectives of the Research

The present energy scenario confirms that wind energy plays a major role in energy sector nevertheless; there is still a lack of attention by industry and policy makers towards the wind energy market. Concerning research too, only a few people are interested in the wind energy field. The motivation to carry out the present research originated from the fact that few Indian wind mill manufacturers only have a strong research and development back up for designing wind mill blades.

The efficiency of the primary processes for generation of wind power has improved during the last 30 years. To make the wind power economically feasible, it is important to further maximize the efficiency in converting wind energy into mechanical energy. Among the different aspects involved, rotor aerodynamics is the key determinant for achieving this goal. The wind turbine

aerodynamics involves several aspects that are unique to turbo machines as following.

The wind turbines operate in the lowest part of the atmospheric boundary layer, where steady wind is an off-design condition, so that wind turbine aerodynamics is essentially unsteady. Unlike most of the aerodynamic devices, wind turbine does not avoid stall, but rely on it for limiting power. Hence thorough understanding of unsteady deep stall is necessary. Moreover, the flow past a wind turbine blade is three-dimensional, particularly at the blade-tip and root region. For instance centrifugal and Coriolis forces are experienced by the boundary layer flow, mainly in the inboard, causing a stall-delay effect, which leads to a higher lift compared to two-dimensional data.

The aerodynamic research on wind turbines has basically contributed to the fast development of modern wind energy sector. The aim of this present research is to investigate the possibility of improving wind energy capture even under low and high relative wind speed conditions. This work attempts the development of a new configuration of wind turbine blades, based on the results of studies using numerical simulations.

The important parameters such as pressure, skin friction drag, skin friction coefficient, and total drag are to be analyzed under wind flow on blades with various angles of attacks. Output power of the wind turbine generator is to be calculated. The complexities in the design of rotor and airfoil made the design of the horizontal axis wind turbine difficult. The selection of the airfoil series requires meticulous study and proper references. All these considerations were taken into account while carrying out the present research.

The ability to predict the downstream wake from a wind turbine is a significant factor for determining the interactions between adjacent wind mills.

Three approaches are available to analyze the flow around and downstream of a wind turbine: 1. Field or wind tunnel testing, which provides accurate results but is highly complex and expensive; 2. Analytical and semi-empirical models which adopt simplifying assumptions and are thus not universally reliable; and 3. Computational Fluid Dynamics (CFD), which probably offers the best support or alternative to direct measurements.

Airfoil characteristics include both aerodynamic and structural requirements. For the outer part of the blade, the most important parameters from the structural point of view are the maximum airfoil thickness and the chord-wise location of the maximum thickness. The thickness of the profile must be able to accommodate the structure necessary for blade strength and stiffness. Depending on the class of the wind turbine, certain values are required for the thickness along the blade. In the case of Mega-Watt class wind turbine, for example, a realistic value for the relative thickness at the tip can be around 18 % of the chord. The location of the maximum thickness along the chord is also important. When an airfoil is designed, the blade should be considered to guarantee constructive compatibility. This means that, in order to allow the spar passing through the blade, the chord-wise position of the thickness should be similar for the complete blade. From the aerodynamic point of view the most important parameter for the tip region is the aerodynamic efficiency (L/D). In order to obtain good turbine performance, the aerodynamic efficiency should be as high as possible.

The present work aims at a comprehensive study of the Horizontal Axis Wind Turbine (HAWT) aerodynamics, by numerically solving the fluid

dynamic equations with the help of a finite-volume Navier–Stokes CFD solver. As a more general goal, the study aims at proving the capabilities of modern numerical techniques for the complex fluid dynamic problems of HAWT. The main purpose is hence to maximize the physics of power extraction by wind turbines.

The horizontal axis wind turbine has to generate maximum lift with minimum drag condition, resulting in the maximum power generation. The impact of the speeding wind over the blade results in bracing the airfoil section in it. The lift force with which the wind mill rotates should be maximum and the force component acting as drag should be minimum.

Another important factor to be considered is the flow pattern of the wind. The wind flow over the blade is laminar for considerable span of time but it shifts to the turbulence region over a period of time. This present research investigates the flow progress over the blade. The velocity of approach of airflow towards the blade has been studied. The complexity of the rotor speed and formation of the vortex region over the blade are other important factors. The dimensionless quantity over the trailing edge of turbulence region is modified for maximizing power generation.

The intensity of turbulence over the upper surface of the blade plays a vital role for lift generation. The effect of turbulence reduces wind energy harnessing and leads to decrease in power generation.

This present research work focuses on the outer structure of the blade. The shape and size of the blade are investigated. The surface roughness

property of the blades has been examined using the numerical simulations results in order to optimize it.

The overall objectives of the present research work are as follows:

- To choose the geometry of the turbine blade for a middle sized HAWT rotor.
- To model middle sized HAWT rotor and its flow field.
- To carry out flow simulation of the model for different flow conditions.
- To validate the computed performances of the HAWT rotor with actual field data.
- To study the rotational effects of HAWT rotor blades under multibody dynamic conditions on the boundary layer.
- To suggest techniques for enhancing wind energy generation in HAWT based on the CFD approach.

1.3 Overview of the Thesis

This thesis mainly focuses on the investigation of the wind turbine performance as a function of multi body fluid dynamics. The functioning of modern horizontal axis windmills for electricity production is briefly described in *Chapter 2*. An overall glimpse of the classical aerodynamic models is also presented. The most important definitions related to HAWT are given in *Chapter 2*. In *Chapter 3*, the computational fluid dynamics techniques are introduced. The adopted mathematical model is based on the Reynolds Averaged Navier Stokes (RANS) equations in a rotating reference system. An overview of the available numerical approaches is finally given.

In *Chapter 4*, validations of the computations are pursued by means of a performance assessment and by investigating the general aerodynamic features of middle sized wind turbine rotor. A real rotor geometry has been adopted for the study.

In *Chapter 5*, the capabilities of CFD for the design optimization of HAWT blades are verified. This is done by analyzing the effects of some modifications on the blade sections by varying surface roughness.

In *Chapter 6*, CFD analysis of HAWT blades are verified by analyzing the effects of modifications at the blade sections by introducing the concept of gurney flaps throughout the blade trailing edges and winglet along the blade tip regions.

In *Chapter 7*, the CFD simulations of HAWT blades are verified by analyzing the effects before and after introducing the concept of vortex generators, along the upper surface of the blade geometry. The mathematical modeling and investigations are carried out to optimize the vortex generator size.

Finally, *Chapter 8* deals with the complete summary and conclusions arrived from the present research investigations. The suggestions for future work are also included in this chapter.



WIND TURBINE FUNCTIONING AND THEIR AERODYNAMICS

2.1 Wind Power Technology

Wind turbines are the largest rotating machines on earth. The World's largest passenger airliner, the Airbus A-380 has a wing span of about 80 m, where as Enercon E-126, 6 MW wind turbine has a rotor diameter of 126 m. This HAWT is 138 m tall and has an overall height of 200 m from tower base to blade tip. The HAWT are also the oldest devices for exploring the energy of wind on land. In fact, the only older device for utilizing wind energy is the sailing ship. For centuries, mankind was in need of mechanical energy, mainly for agriculture, and increasingly for other purposes. In order to extract a useful form of energy from wind that is free flowing everywhere, proper machines were necessary and that is how windmills were born.

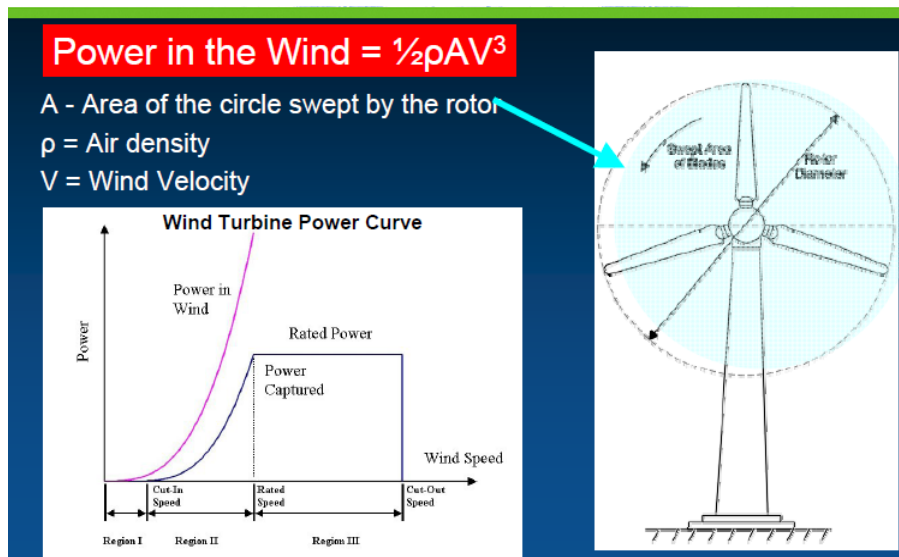


Figure 2.1 Principle of wind energy (Source: AWEA)

The principal of wind energy is shown in Figure 2.1

The wind turbine blades are subjected to a force distribution that results as mechanical torque at the rotor shaft. In modern HAWT the aerodynamic driving force is mainly the lift force as in the aircraft flight, rather than drag force used in ancient sailing ships. The shaft transfers the torque from the blades to the generator, but these passages can be achieved through gear boxes. Today after decades of industrial development, modern turbines transform the wind energy to electric power (Knight and Carver, 2010). The knowledge about the wind power technology has increased over the years. The development of various windmill types from middle-ages to the industrial era can hardly be considered as the result of systematic research and development. In the 17th and 18th centuries, when physical–mathematical thinking became more established, Leonardo, Leibnitz, Bernoulli and Euler involved themselves in systematic results on windmill technologies. Among the others, Danish professor Poul La Cour carried out extensive scientific research in windmill blade aerodynamics and windmill design during the second half of the 19th century, later he experimented on how to generate electrical current with the help of wind power. This marked the turning point from historical windmill building, to the modern technology of power generating wind turbines. Lanchester and Betz were the firsts to predict the maximum power output of an ideal wind turbine. The huge and still increasing sizes of HAWT pose a real challenge to the design engineers.

2.2 Functioning of HAWT

In this section the basics of the functioning of modern HAWT are briefly summarized. The transformation of wind energy into electricity is not obtained directly, but consists of many complicated steps. The latest technologies of

aerodynamics, mechanics, control systems and electro technologies are involved in such processes. The present research work deals with Horizontal Axis Wind Turbines (HAWT). When compared to the Vertical Axis Wind Turbines (VAWT), the HAWTs have

- Higher values of power co-efficient.
- They operate in the high atmospheric boundary layer instead of the bottom shear layer, so they experience more uniform and intense wind speeds.
- The HAWT have more stable mechanical behaviors and they can be constructed in larger sizes.

The most commonly used wind turbine setups are of the following types:

1. A classical turbine with gearbox, i.e. the so-called Danish concept. A gearbox with typically three steps connects the rotor shaft (the slow one) to the generator shaft (the fast one), which is directly connected to the electrical grid and therefore has a fixed rotational speed. The old type configurations do not have an active aerodynamic control, but blades are stall-regulated while wind changes.
2. A turbine without gearbox, with the axle directly connected to the generator. It is a newer concept, compared to the previous one where a large multi-pole generator allows the unique shaft to rotate with the low speed of the rotor.
3. A hybrid concept, which combines the previous two is obtained by adopting a smaller generator and a smaller (usually one-step) gearbox for matching the required angular speed.

Further, the following four concepts can be distinguished with regard to the rotor- generator grid coupling (Reisenthel *et al.*, 2003).

- Type A - fixed speed wind turbine concept corresponds to the “Danish concept”. In this type of wind mill a squirrel cage induction generator (SCIG) is directly connected to the grid through a transformer.
- Type B - variable speed wind turbine concept with variable rotor resistance.

This type of wind mill uses optislip induction generator, where the rotor winding of the generator is connected with an optically (without slip-rings) controlled resistance. By changing the resistance the slip changes and thus the power output can be varied in the range of 0-10 % of the synchronous speed.

- Type C - variable speed wind turbine concept with partial-scale power converter.

This configuration denotes the variable speed controlled wind turbine with doubly fed induction generator (DFIG) and pitch control. In this type the stator is directly connected to the grid, while the rotor is connected through a partial-scale power converter. The variable speed range is +/- 30 % around the synchronous speed.

- Type D - variable speed wind turbine concept with full-scale power converter.

This configuration of HAWT corresponds to the full variable speed, pitch-controlled with the generator connected to the grid through a full-scale power converter. The generator can be excited electrically (WRSG or WRIG) or by permanent magnets (PMSG) or squirrel cage induction generator (SCIG). Typically, a direct driven, multi-pole synchronous generator (no gearbox) is used in this type. This concept has full control of the speed range from 0 to

100% of the synchronous speed (Vermeer *et al.*, 2003). However, it has a higher power loss compared to Type C concept, as all the generated power has to pass through the power converter.

Thus it is clear that the aerodynamic control and regulation systems allow the turbine to follow the variable wind. All modern turbines have variable pitch of 10° . As wind intensity increases the pitch changes to follow the best aerodynamic flow angles along the blades and angular speed increases for absorbing the torque. The turbine must also yaw into the wind. For attaining this, on the top of the nacelle an anemometer together with a wind vane which determines intensity and direction of the incoming wind are kept. The output signal commands the control electric motors of the HAWT.

The start-up wind velocity (cut-in) of a wind turbine is about 3 to 5 m/s. While the wind speed increases the power production also grows along with it, till the rated power is reached and then the exceeding output is limited. At a fixed value of wind speed (cut-off), typically around 25 m/s the turbine stops for safety reasons (standstill). For the correct functioning of a wind turbine, control systems are needed till rated power is reached, these control systems should make the turbine work with the maximum efficiency, whereas after the rated or peak power is reached the target of the control system is to keep the power generation as a constant (Sohn *et al.*, 2005, Timmer and Rooij, 2003). The various control systems are grouped into three families

- Stall control

This control system is a passive way of controlling the power output of a wind turbine. The blades are aerodynamically shaped in order to work with optimum angle of attack at the average wind speeds whereas, at higher speed the flow angle increases, separation occurs on their sections and that is how lift

force is limited. As wind keeps increasing, the lift force of the blades also decreases because of increasing stall. The exceeding loads are in such a way to completely dissipated and no possible control on the efficiency could be done in the low-speed operating range. No rotational speed control is here available. Small and economical turbine types adopt this regulation, as well as the older models (Johnson, 1985).

- Pitch control

In this method of control system the blades can be pitched, i.e. turned around their axes by means of hydro dynamic or electrical motors. In such a way they follow the optimum angles till the rated power speed is reached and then the loads are limited by loosing lift forces (Glauert, 1948).

- Active stall

In active stall control system stall is triggered intentionally. When the wind mill is in stall only very small pitch excursions are required to give shorter response times than those of pitch control. However, stall is an unstable operating condition and thrust is allowed to remain large.

The significant traits of a wind turbine are summarized below (Glauert, 1948).

- Number of blades: 1, 2, 3, 4
- Rotational speed: 20-50 RPM
- Tip-speed (ωR): less than 70 m/s for noise limitation
- Rated power: from 1 kW (Micro-turbine) to 10 MW (Multi-MW WT)
- Control system: stall-regulation, active-pitch, variable speed (rotational)
- Tower-height/Rotor-diameter ratio: H/D

The increasing penetration of large wind turbines into electrical power systems is inspiring continuously the designers to develop both custom generators and power electronics, and to implement modern control system strategies. The wind turbine design objectives have thus changed over the years from being conventional-driven to being optimized-driven, within the operating regime and market environment. In addition to becoming larger, wind turbine design concepts have been progressing from fixed speed, stall-controlled and drive trains with gearbox to variable speed, pitch-controlled with or without gearbox (Patel, 1999).

2.3 A Brief Review of the Aerodynamic Models

The size of commercial wind turbines has increased dramatically in the last 25 years, from a rated power of approximately 50 kW and a rotor diameter of 10 to 15 m up to today's commercially available 5-10 MW machines with a rotor diameter of more than 120 m (Liu and Jameson, 1992, *Reisenthel et al.*, 2003). This development has forced the design tools to change, from simple static calculations assuming a constant wind to dynamic simulation software that uses unsteady aerodynamic loads to model the aero elastic response of the entire wind turbine construction (Johnson, 1985).

Here, the basic theories for different classical aerodynamic models are treated. The following models will be reviewed in the present section.

- Blade Element Momentum method (BEM).
- Lifting line, panel and vortex methods.
- Actuator disc method.
- Navier-Stokes solvers.

2.3.1 Basic Definitions

- **Tip speed ratio**

The tip speed ratio is a very important parameter for wind turbine design. It expresses the ratio between the tip speed and the undisturbed wind speed.

$$\lambda = \omega R / U_{\infty} \dots\dots\dots 2.1$$

Where, ω is the angular velocity, R the radius of the blades and U_{∞} the undisturbed wind speed. The tip speed ratio dictates the operating condition of a wind turbine and it affects a number of flow parameters that will be discussed later. Typical values for modern turbines are 6 to 8. For tip speed ratio at radius r, it is common to use r instead of R in equation 2.1.

- **Solidity**

The turbine solidity is defined as the ratio between the blade areas to the area of the disk.

$$\sigma = \frac{\text{Total blade area}}{\text{disc area}} \dots\dots\dots 2.2$$

And like the local tip speed ratio the local turbine solidity is also defined, while referring to certain radius r, as follows

$$\sigma = \frac{Bc(r)}{2\pi r} \dots\dots\dots 2.3.$$

Here B is the number of blades and c the chord length of the local blade section (Patel, 1999).

Power coefficient

The kinetic energy of an air mass m moving at a free stream velocity U can be expressed as

$$E = \frac{1}{2} mU^2 \dots\dots\dots 2.4$$

And for unit mass

$$e = \frac{1}{2} U^2 \dots\dots\dots 2.5$$

Taking a certain cross-section area A, by which the air passes at the velocity U, the volume Q during a certain time unit is

$$Q = UA \dots\dots\dots 2.6$$

And the mass flow with the air density ρ is

$$\dot{m} = \rho Q = \rho UA \dots\dots\dots 2.7$$

With the product of the kinetic energy of the moving air and the mass flow, one yields the amount of energy passing through a cross-section A per second. It is physically the power P (Johnson, 1985, CWET 2010).

$$P_0 = \dot{m}e = \frac{1}{2}\rho U^3 A \dots\dots\dots 2.8$$

This is the available power in the wind. However, if we had taken the whole energy, the flow would be arrested. Thus there should be a power coefficient C_p that determines the portion of the flow energy captured by the wind energy converter (Liu, 2010, Johnson, 1985).

$$P = C_p P_0 \Rightarrow C_p = \frac{P}{\frac{1}{2}\rho U^3 A} \dots\dots\dots 2.9$$

According to Betz, C_p can never exceed a value of $C_p \text{ max} = 16/27$ (Overgaard & Lund, 2010).

- **Thrust coefficient**

In a similar way the thrust coefficient could be defined for the integral thrust force acting on the rotor T (Velte *et al.*, 2008, Selig and Tangler, 1999).

$$C_T = \frac{T}{\frac{1}{2}\rho U_{\infty}^2 A} \dots\dots\dots 2.10$$

Induction factors

The incoming wind flow is affected by the turbine blade as it approaches the rotor. The effective apparent velocity seen by the blade vortex system is modified as illustrated in Figure 2.1.

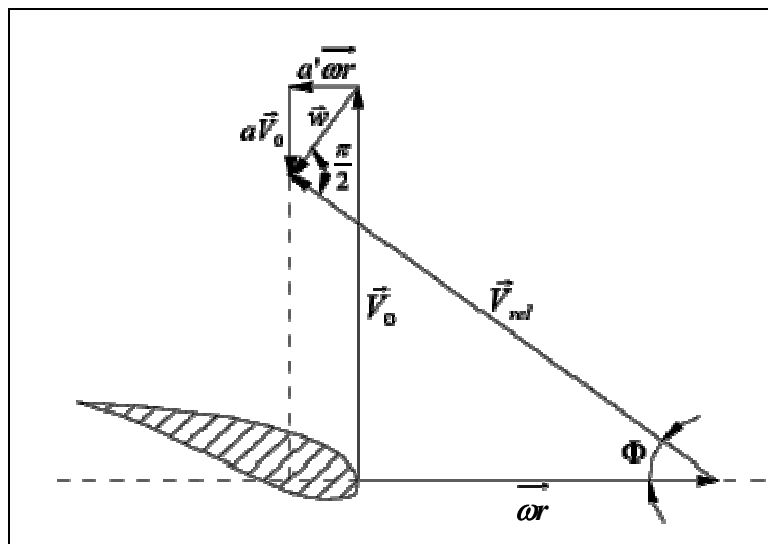


Figure 2.2 Relative velocity concepts

By decomposing the velocity vector into its axial or stream wise and tangential component and introducing the induction factors, we get these relationships.

$$\Gamma = \int u ds \dots\dots\dots 2.14$$

Lift and drag coefficients define the characteristic of an airfoil (Johnson, 1985).

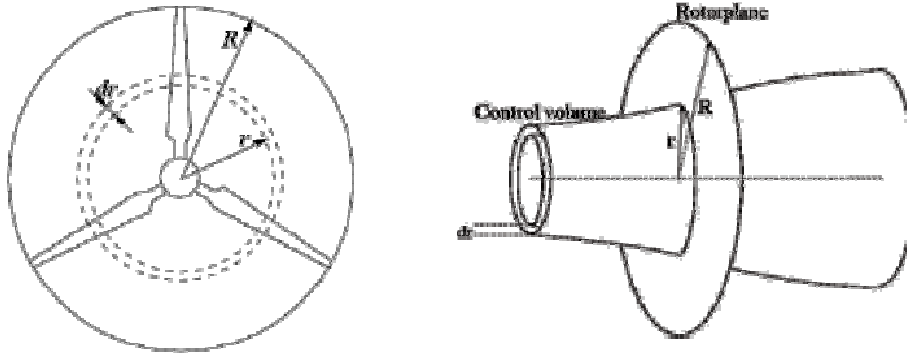


Figure 2.3 BEM annular control volumes.

$$C_l = \frac{L}{0.5\rho U^2 C} \dots\dots\dots 2.15$$

$$C_d = \frac{D}{0.5\rho U^2 C} \dots\dots\dots 2.16$$

Where L and D forces per unit span, the flow speed and C the chord length. These coefficients are function of the angle of attack, Reynolds number and Mach number (Patel, 1999).

- **Pressure coefficient**

Dealing with airfoils, pressure coefficient is often defined as follows

$$C_p = -\frac{P - P_\infty}{0.5\rho U^2} \dots\dots\dots 2.17$$

This is an inverse to the general definition, in order to have the positive suction, which is the main contribution to lift generation (Overgaard and Lund, 2010; Nelson *et al.*, 2008; Glauert, 1948).

2.3.2 The BEM Method

Loads and performance calculations of wind turbines are today routinely performed by the Blade-Element Momentum method. The method is indeed computationally cheap and thus very fast, even with providing very satisfactory results. The BEM method consists of dividing the flow in annular control volumes and applying momentum balance and energy conservation in each control volume. The annuli are bounded by stream surfaces that enclose the rotor and extend from far upstream to far downstream. Basic assumptions of this method are that, the induced velocity in the rotor plane is equal to one half of the induced velocity in the ultimate wake, and that the flow can be analyzed by dividing the blade into a number of independent elements. Moreover the loads for each blade are uniformly distributed azimuth-wise, which means the rotor would have an infinite number of blades. For each blade element, the aerodynamic forces are obtained using tabulated airfoil data, which stem from wind tunnel measurements and corrected for three-dimensional effects. The BEM could be a design as well as verification method and when using BEM as a design method, the following inputs and outputs are defined:

- **Input:**

Rated power P , power coefficient C_P , mean wind speed V_0 , number of blades B

- **Output:**

Rotor diameter D , chord $C_i(r)$ and twist $\theta_i(r)$ radial distribution.

This is in principle the BEM method, but in order to get good results it is necessary to apply, at least, the following two corrections.

- The first is called Prandtl's tip loss factor, which corrects the assumption of an infinite number of blades.
- The second correction is called Glauert's correction and is an empirical relation between the thrust coefficient C_T and the axial interference factor for values greater than approximately 0.3, where the relation derived from the one-dimensional momentum theory is no longer valid.

Since the BEM model is simple and very fast to run on a computer, it has gained an enormous popularity and is today the common design code in use by industry. However, owing to limitations of representing all the various flow situations encountered in practice, it has become necessary to introduce different empirical corrections. Such situations include phenomena related to dynamic inflow, yaw misalignment, tip loss and heavily loaded rotors. Thus there exists an increasing need to establish experiments and to develop more advanced models to evaluate the basic assumptions underlying the BEM model. Although today there seems to be no realistic alternative that may replace the BEM model as an industrial design tool, a number of more advanced inviscid models have been developed to overcome the limitations of the momentum approach (Liu, 2010; Madsen *et al.*, 1998; Johnson, 1985).

2.3.3 Lifting Line, Panel and Vortex Methods

Three dimensional inviscid aerodynamic models have been developed in an attempt to obtain a more detailed description of the 3D flow that develops around a wind turbine. The fact that viscous effects are neglected is certainly restrictive as regards the usage of such models on wind turbines. However, they should be given the credit of contributing to a better understanding of dynamic inflow effects as well as providing a better insight into the overall flow development. There have been attempts to introduce viscous effects using

viscous–inviscid interaction techniques. But they are not used in wind turbine functioning and aerodynamics, as they are not yet reached the required maturity so as to become engineering tools, although they are full 3D models that can be used in aero elastic analyses. In vortex models, the rotor blades, trailing and shed vortices in the wake are represented by lifting lines or surfaces. The vortex strength on the blades is determined from the bound circulation that stems from the amount of lift created locally by the flow past the blades. The trailing wake is generated by the span wise variation of the bound circulation, while the shed wake is generated by a temporal variation, and ensures that the total circulation over each section along the blade remains constant in time. Knowing the strength and position of the vortices, the induced velocity $w(x)$ can be found at any point using the Biot-Savart induction law (Liu and Jameson, 1992, Patel, 1999).

$$w(x) = -\frac{1}{4\pi} \int \frac{(x-x') \times \omega'}{|x-x'|^3} dV \dots\dots\dots 2.18$$

Where w is the vortices, the point x where the potential is computed and x' is the point of integration, which is taken over the region where the vortices is non-zero. In the lifting lines models, the bound circulation is found from airfoil data table, just as in the BEM method. The inflow is determined as the sum of the induced velocity, the blade velocity, and the undisturbed wind velocity (Sohn *et al.*, 2005, Knight and Carver, 2010).

The relationship between the bound circulation and the lift is the well-known Kutta-Joukowski theorem, and using this together with the definition of the lift coefficient, a simple relationship between the bound circulation and the lift coefficient can be derived.

$$L = \rho U_{\text{rel}} \Gamma = \frac{1}{2} \rho U_{\text{rel}}^2 c C_L \rightarrow \Gamma = \frac{1}{2} U_{\text{rel}} c C_L \dots\dots 2.19$$

In its simplest form the wake from one blade is prescribed as a hub vortex plus a spiraling tip vortex, or as a series of ring vortices. Actually, one of the most recurrent applications of vortex methods has been wake dynamics. The inviscid and incompressible flow past the blades can be found by applying a surface distribution of sources and dipoles. This is the approach followed by panel methods (Liu and Jameson, 1990, Velte, 2008). The background is green's theorem which allows obtaining an integral representation of any potential flow field in terms of singularity distribution. An external potential flow field is given, possibly varying in time and space, to which is added a perturbation scalar potential. The active boundary of the flow includes both the solid boundaries as well as the wake surfaces. Dipoles are added so as to develop circulation into the flow to simulate lift.

2.3.4 Actuator Disk Method

The actuator disk model is probably the oldest analytical tool for evaluating rotor performance. In this model, the rotor is represented by a permeable disk that allows the flow to pass through the rotor, at the same time it is subjected to the influence of the surface forces. The classical actuator disk model is based on conservation of mass, momentum and energy, and constitutes the main ingredient in the D momentum theory, as originally formulated by Rankine and Froude. Combining it with a blade-element analysis, we end up with the classical Blade-Element Momentum Technique by Glauert. In its general form, however, the actuator disk might as well be combined with the Euler or NS equations. Thus, as will be told in the following, no physical restrictions have to be imposed on the kinematics of the flow. In a numerical actuator disk model, the NS (or Euler) equations are typically solved by a

second order accurate finite difference/volume scheme, as in a usual CFD computation. However, the geometry of the blades and the viscous flow around the blades are not resolved. Instead, the swept surface of the rotor is replaced by surface forces that act upon the incoming flow. The main limitation of the axisymmetric assumption is that the forces are distributed evenly along the actuator disk; hence the influence of the blades is taken as an integrated quantity in the azimuth direction. To overcome this limitation, an extended 3D actuator disk model has recently been developed. The model combines a 3D NS solver with a technique in which body forces are distributed radially along each of the rotor blades. Thus, the kinematics of the wake is determined by a full 3D NS simulation, whereas the influence of the rotating blades on the flow field is included using tabulated airfoil data to represent the loading on each blade. As in the axis symmetric model, airfoil data and subsequent loading are determined iteratively by computing local angles of attack from the movement of the blades and the local flow field. The concept enables one to study in detail the dynamics of the wake and the tip vortices and their influence on the induced velocities in the rotor plane (Dahl *et al.*, 1998; Timmer and Van Rooij, 2003; Patel, 1999).

The main motivation for developing such types of model is to analysis and verifies the validity of the basic assumptions that are employed in the simpler and more practical engineering models.

2.3.5 Navier-Stokes Solvers

The first applications of CFD to wings and rotor configurations were studied way back in the way late seventies and early eighties, in connection with aircraft wings and helicopter rotors, using potential flow solvers.

A shift towards unsteady Euler solvers was seen through the 80's. Full-Reynolds Averaged Navier Stokes (RANS) equations were solved first for

helicopter rotor computations, including viscous effects, in the late eighties and early nineties, but the first full NS computations of rotor aerodynamics were reported in the literature in the late nineties (Knight and Carver, 2010).

Recently, Detached Eddy Simulations (DES) and Large Eddy Simulation (LES) techniques, which are becoming increasingly important in several engineering fields, have been directed at solving turbine's flow even though high computational efforts still remain a drawback for a practical usage.

Nowadays, an extensive literature on N-S CFD studies on wind turbine exists. Since this method has been chosen for the study of WT aerodynamics, a more comprehensive description of the CFD methodologies will be discussed in the forth coming chapters.

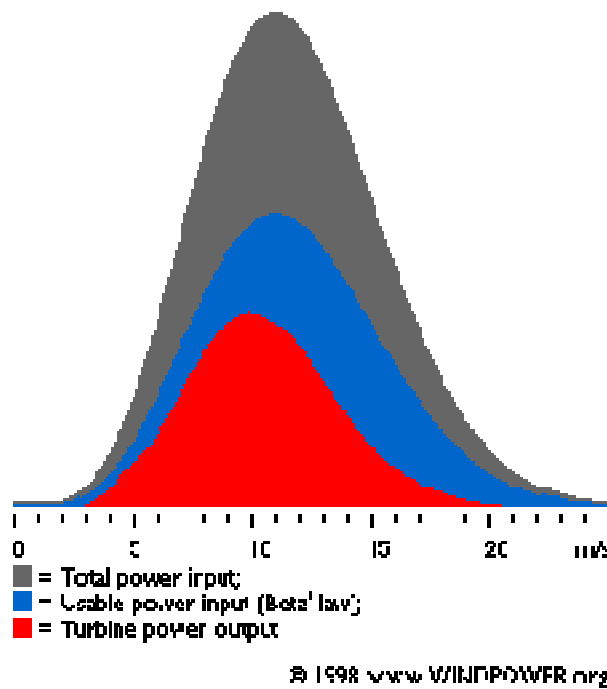


Figure 2.4 Wind power distributions

(Source *www.WINDPOWER.org* 1998)

In the *Figure 2.4* the colors indicate the wind power distribution as stated below.

Gray: Total Potential Wind Power, Blue, Usable Power (Betz' Law) and Red: Turbine Power Output

The present work aims at maximizing the turbine power output to match with the Betz limit.

2.4 Literature Review on Aerodynamics

Liu and Jameson (1990) carried out an experimental study over force constants, speed/power relationship and velocity contours using the panel method. Liu and Jameson (1992) predicted the end wall effect boundary layer condition of flow analysis. Castino *et al.*, (1976) developed a new model which treated both the wind speed and wind direction dynamics. Their analyses were made over stochastic properties of wind speed with the help of two models (i) Markov chain model and (ii) discrete auto regressive model of order 2 (DAR(2)). In their analyses they concluded that, it was impossible to describe the time series of the wind velocity.

The solution space was parameterized by Mach number, pitch angle, grid resolution, and solution algorithm settings were addressed in the paper by Patrick *et al.*, (2003). The static load carrying capacity, buckling stability, blade tip deflection and natural frequencies at various rotational speeds and fatigue strength were evaluated by Sohn *et al.*, (2005) to satisfy the strength requirements in accordance with the IEC 61400-1 and GL Regulations.

The aim of the research carried out by Velte (2008) was to investigate the effect of vortex generators in a turbulent, separating, low Reynold's number (Re 20000) boundary layer over geometry which was similar to flow past a wind turbine blade. A qualitative comparison with LES simulations of the flow

behind vortex generator was made which showed that LES was capable of reproducing flow structure.

In their report Roberl *et al.*, (2008) proposed a methodology called PACE (Plasma Aerodynamic Control Effectors). This paper serves as an experimental report on significant aerodynamics characteristics.

Overgaard and Lund (2010) have carried out a Finite Element Analysis of about the geometric nonlinear and inter laminar progressive failure of a generic wind turbine blade which was undergoing a static flap wise load. Results were compared with the experimented findings and the aero dynamical loading and thrust were found numerically.

Knight and Carver (2010) showed that the energy capture of STAR rotor was 12 % for long run and 36 % for short run with the measured results of 3322 and 2524 data points respectively, when compared to other rotors run simultaneously.



3.1 CFD Governing Equations

The governing equations which are used in CFD are based on the following conservation laws of physics:

- Conservation of mass.
- Newton's second law: the change of momentum equals the sum of forces on a fluid particle.
- First law of thermodynamics (conservation of energy): rate of change of energy equals the sum of rate of heat addition to and work done on fluid particle.

3.1.1 Lagrangian Description

This approach (*Figure 3.1*) is otherwise called as 'particle approach'. A fluid flow field can be thought of as being comprised of a large number of finite sized fluid particles which have mass, momentum, internal energy, and other properties. Mathematical laws can be written for each fluid particle. Fluids in material volume (system) will move, distort and change size and shape, but always consists of the same fluid particles (Bennett *et al.*, 1998).

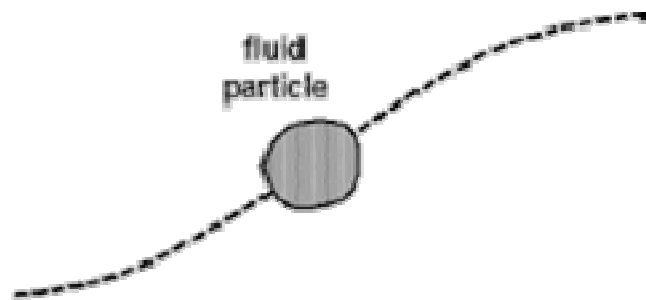


Figure 3.1 Lagrangian Description

3.1.2 Eulerian Description

This is otherwise called as ‘field approach’ (*Figure 3.2*). In this model individuals are not labeled and not distinguished from one another. In the Eulerian description of fluid motion, we consider how flow properties change at a fluid element that is fixed in space and time (x, y, z, t), rather than following individual fluid particles (Tholudin *et al.*, 2004).

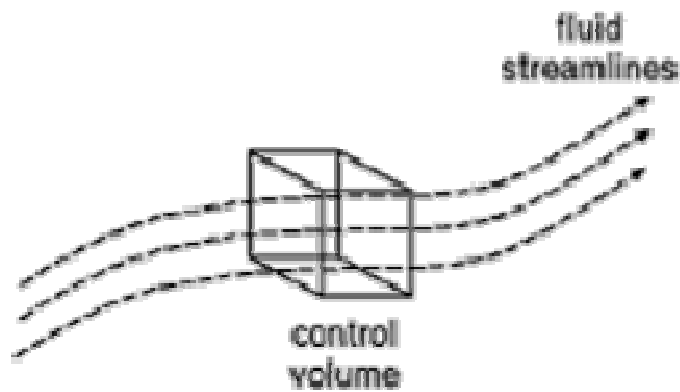


Figure 3.2 Eulerian Description

3.1.3 Continuity Equation

The continuity equation is governed by the “principle of conservation of mass”. It states that ‘the mass of fluid flowing through the pipe at all cross

sections remains constant if there is no fluid is added or removed from the pipe’ (Sorensen, 2009, Tholudin *et al.*, 2004).

The rate of increase of mass in fluid element equals the net rate of flow of mass into the element. Rate of increase of mass is expressed as;

$$\frac{\partial}{\partial t}(\rho\delta x\delta y\delta z) = \frac{\partial \rho}{\partial t} \delta x\delta y\delta z \dots\dots\dots 3.1$$

3.1.4 Momentum Equation

This equation is purely based on ‘Newton’s second law of motion’ (F=ma). The net force acting in any direction is equal to rate of change of momentum in that direction.

Linear impulse=change in linear momentum (Ng *et al.*, 2005, Tomokazu *et al.*, 2009).

In x-direction, initial linear impulse + or - linear impulse=final linear momentum. Rate of increase of x-, y-, and z-momentum is:

$$\rho \frac{Du}{Dt} \quad \rho \frac{Dv}{Dt} \quad \rho \frac{Dw}{Dt} \dots\dots\dots 3.2$$

The forces acting on fluid particles are as follows;

- Surface forces such as pressure and viscous forces.
- Body forces, which act on a volume, such as gravity, centrifugal, Coriolis, electromagnetic forces (Versteeg and Malalasekera, 2007).

3.1.5 Navier-Stokes Equation

The equations of motion without considering force due to turbulence and considering the gravity, pressure and viscosity forces are known as Navier-Stokes equation (Ng, *et al.*, 2005, Sorensen, 2009, Versteeg and Malalasekera, 2007).

$$F_x = (F_g)_x + (F_p)_x + (F_v)_x, \text{ for } x \text{ direction.}$$

$$F_y = (F_g)_y + (F_p)_y + (F_v)_y, \text{ for } y \text{ direction.}$$

$$F_z = (F_g)_z + (F_p)_z + (F_v)_z, \text{ for } z \text{ direction.}$$

Where, F_g - gravity force.

F_p - pressure force.

F_v - viscous force.

The Navier-Stokes equations form a coupled system of nonlinear PDE's describing the conservation of mass, momentum and energy for a fluid. For a Newtonian fluid in one dimension, they can be written as

$$Q = \Delta E + W \dots\dots\dots 3.3$$

$$dE = \Delta Q - \Delta W$$

$$Q = \begin{bmatrix} \rho \\ \rho u \\ e \end{bmatrix}, E = \begin{bmatrix} \rho u \\ \rho u^2 + p \\ u(e + p) \end{bmatrix} - \begin{bmatrix} 0 \\ \frac{4}{3} \mu \frac{\partial u}{\partial x} \\ \frac{4}{3} \mu \frac{\partial u}{\partial x} + k \frac{\partial T}{\partial x} \end{bmatrix}$$

ρ is the fluid density, u is the velocity, e is the total energy per unit volume, p is the pressure, T is the temperature, μ is the coefficient of viscosity, and κ is the thermal conductivity. The total energy e includes internal energy per unit volume $\rho \cdot e$ (where e is the internal energy per unit mass) and kinetic energy per unit volume is $\rho u^2/2$ (<http://www.bakker.org>, Tomokazu *et al.*, 2009).

3.2 Solution Procedure

3.2.1 Segregated Solution Procedure

Figure 3.3 shows the flow chart for the segregated solution procedure.

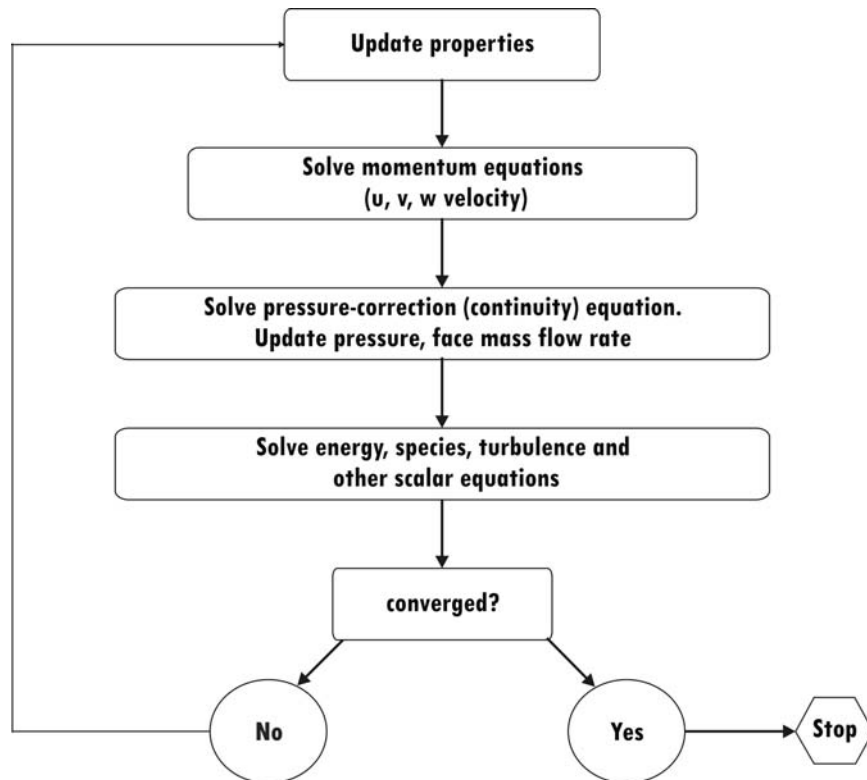


Figure 3.3 Segregated Solution Procedures

3.2.2 Coupled Solution Procedure

When the coupled solver is used for steady state calculations it essentially employs a modified time dependent solution algorithm, using a time step (Ng *et al.*, 2005).

$$\Delta t = CFL / (U/L) \dots\dots\dots 3.4$$

Where Δt is the time step.

CFL is the Courant-Friedrich-Levy number.

\mathbf{u} - Local velocity.

L - Size of the cell.

3.3 Rotating Reference Frames

The equations of fluid flow are usually solved by numerical solution solvers in a stationary (or non inertial) reference frame. However, there are many problems that require the equations to be solved in a moving (or-inertial) reference frame. A rotating rotor of a wind turbine is one such case. With a moving reference frame, the flow around the moving part can be modeled (with certain restrictions) as a steady-state problem, with respect to the moving frame. The moving reference frame modeling capability allows to model problems involving moving parts by activating moving reference frames in selected cell zones. When a moving reference frame is activated, the equations of motion are modified to incorporate the additional acceleration terms which occur due to the transformation from the stationary to the moving reference frame (Glauert, 1948, Tomokazu, *et al.*, 2009). By solving these equations in a steady-state manner, the flow around the moving parts can be modeled. For simple problems, it may be possible to refer the entire computational domain to a single moving reference frame. This is known as the single reference frame or SRF approach (Tony *et al.*, 2001).

3.4 Post-Processing

The numerical solution solvers allow a complete post-processing of solution data. Moreover, the solution data can be easily exported in a number of common file formats, to be analyzed with other post-processing tools. Results are usually reviewed in one of the two ways either graphically or alphanumerically (Sorensen, 2009, Tholudin *et al.*, 2004).

- Graphically:
 - ❖ Vector plots.

- ❖ Contours.
- ❖ Iso-surfaces.
- ❖ Flowlines.
- Alphanumeric:
 - ❖ Integral values.
 - ❖ Drag, lift, torque calculations.
 - ❖ Averages, standard deviations.
 - ❖ Minima, maxima.
 - ❖ Compare with experimental data.

3.5 LES and DES Approach

As an alternative to the Reynolds-averaged methodology, large eddy simulation (LES) techniques have been widely explored in the past years. Although LES gives a better physical representation of the eddy dynamics in separated flows, it is still limited to flow problems at moderate Reynolds numbers. As the RANS equations fail to simulate massive separation, even when simulations are performed in a time-true sense and large eddy simulations CFD and wind turbines (LES) are unaffordable. Hence hybrid LES/RANS approaches, such as detached eddy simulation (DES), represent an attractive compromise between computing costs and accuracy. The idea behind hybrid approaches is to combine fine-tuned RANS technology in the boundary layers, and the simple power of LES in the separated regions. In the RANS regions, the turbulence model has full control over the solution through the eddy-viscosity based closure. In the LES region, little control is left to the model, the larger eddies are resolved both in space and time, and grid refinement directly expands the range of scales in the solution. This reduces considerably the computing costs, as compared to a full blown LES (Tony *et al.*, 2001).



CFD COMPUTATIONS FOR VALIDATION OF PERFORMANCE OF HAWT

4.1 Introduction

In the present research the performance of HAWT is analyzed using CFD simulation approach. Further, techniques introduced in this research have been evaluated for enhancing the performance of HAWT.

The basic model of HAWT taken for the present numerical analysis is the one whose performance was field tested by NREL. The model is created with the actual sizes of the HAWT components in 1:1 ratio.

4.2 Assumptions Made

The following assumptions are made for calculating the power generated by the wind turbine using the CFD tool.

1. The wind flow is steady.
2. The structure has zero wall thickness and thus, weight and inertia are neglected.
3. Aero elasticity and flutter effects are neglected.
4. The blade of the turbine has uniform surface roughness.
5. The power generated is transferred to the grid and thus, the frequency is maintained.
6. Wind is flowing perpendicular to the plane of rotation of the blades.

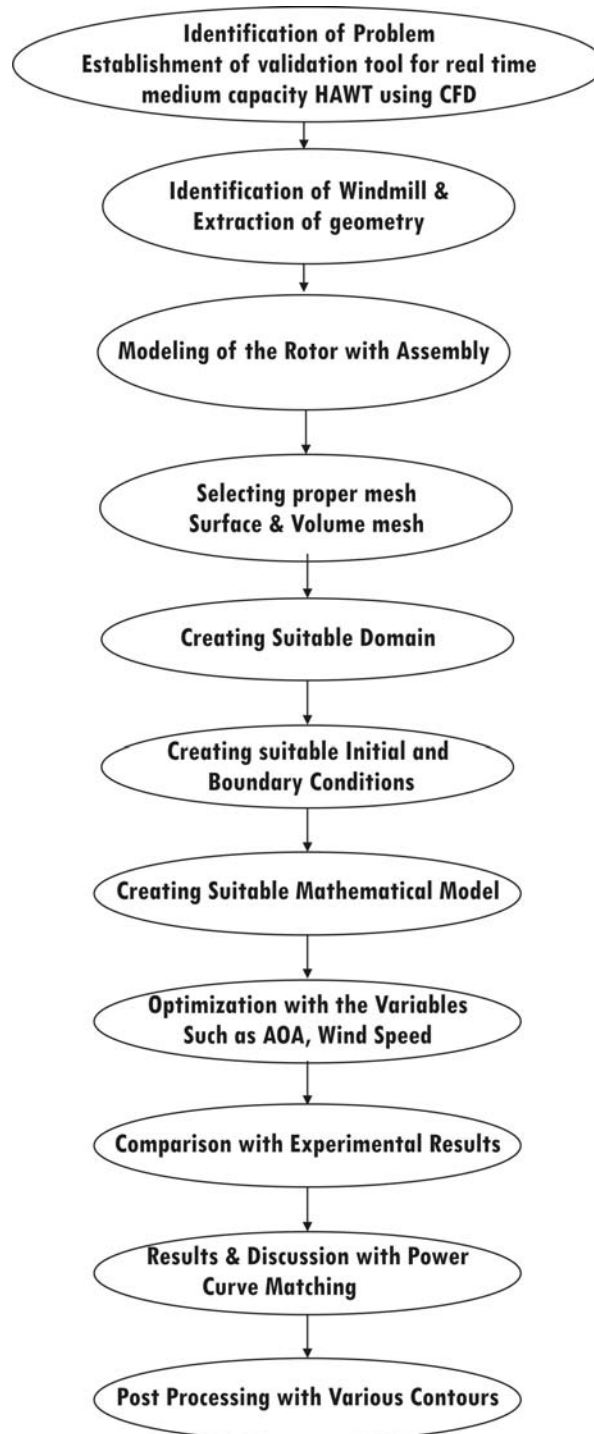


Figure 4.1 Methodology for CFD analysis of HAWT

4.3 Blade Modeling

The airfoils S816, S817 and S818 forming the blade of the HAWT were used for the present study. These airfoils were developed by the NREL. The profile of the airfoils is shown in *Figure 4.2*.

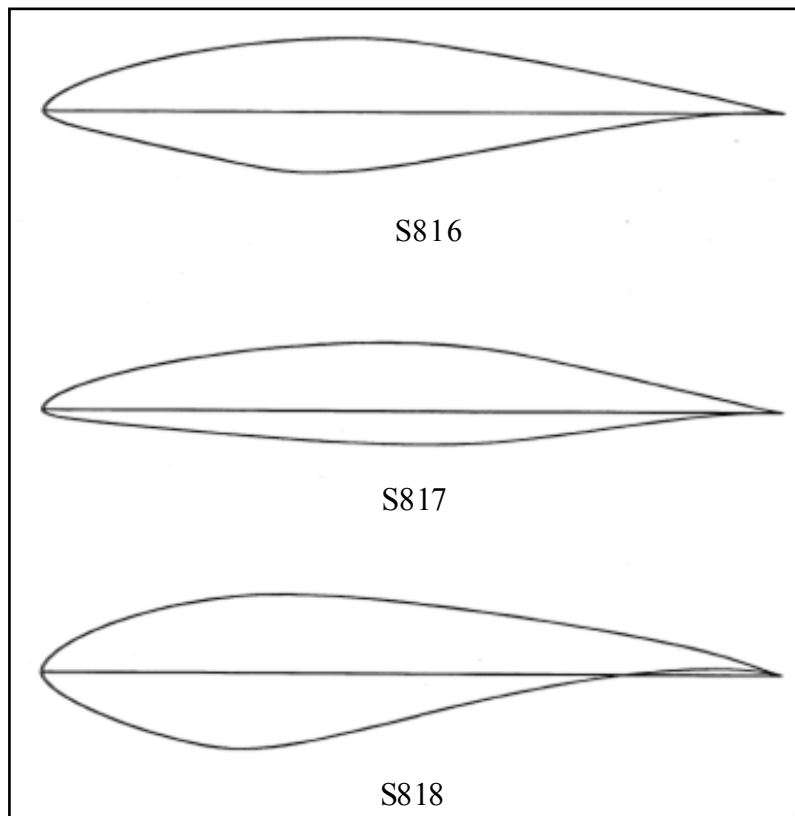


Figure 4.2 Profile of S816, S817 & S818 airfoil. (Source: Somer, 1992)

The co-ordinates forming the upper and lower surface of the airfoil S816 is given in the *Table 4.1*.

Table – 4.1 Co-ordinate values of airfoil S 816 (Source: Somer, 1992)

Upper Surface		Lower Surface	
x/c	y/c	x/c	y/c
0.00000	0.00009	0.00019	-0.00158
.00023	.00198	.00093	-.00314
.00302	.00863	.00220	-.00475
.01099	.01818	.00368	-.00620
.02379	.02836	.01412	-.01294
.04125	.03888	.03050	-.01988
.06315	.04950	.05260	-.02698
.08920	.06005	.08019	-.03456
.11901	.07033	.11247	-.04309
.15222	.08009	.14831	-.05249
.18843	.08912	.18682	-.06232
.22723	.09720	.22730	-.07231
.26818	.10411	.26846	-.08222
.31082	.10965	.30881	-.09050
.35467	.11360	.34877	-.09483
.39923	.11569	.39005	-.09470
.44398	.11547	.43340	-.09089
.48900	.11217	.47890	-.08411
.53503	.10591	.52644	-.07515
.58217	.09767	.57555	-.06477
.62982	.08824	.62567	-.05360
.67730	.07811	.67615	-.04229
.72392	.06774	.72622	-.03146
.76893	.05749	.77501	-.02165
.81158	.04763	.82154	-.01331
.85113	.03838	.86477	-.00676
.88685	.02976	.90364	-.00216
.91827	.02165	.93713	.00052
.94534	.01412	.96426	.00150
.96784	.00776	.98412	.00118
.98512	.00320	.99605	.00038
.99617	.00072	1.00000	.00000
1.00000	.00000		

The co-ordinate values of the HAWT blade airfoils which are taken up for the present study are calculated in accordance with the chord value and geometry mentioned in *Table 4.2*.

Table – 4.1(a) Co-ordinate values of airfoil S 817 (Source: Somer, 1992)

Upper Surface		Lower Surface	
x/c	y/c	x/c	y/c
0.00010	0.00117	0.00001	-0.00038
.00036	.00243	.00029	-.00169
.00443	.01001	.00107	-.00285
.01313	.01841	.00235	-.00398
.02661	.02718	.00925	-.00755
.04479	.03620	.02330	-.01157
.06748	.04533	.04329	-.01517
.09441	.05445	.06911	-.01857
.12517	.06342	.10030	-.02217
.15941	.07203	.13611	-.02613
.19672	.08010	.17584	-.03033
.23667	.08746	.21884	-.03464
.27883	.09392	.26447	-.03891
.32273	.09934	.31211	-.04294
.36790	.10355	.36113	-.04655
.41384	.10640	.41092	-.04952
.46005	.10771	.46088	-.05162
.50602	.10727	.51041	-.05260
.55134	.10473	.55893	-.05200
.59585	.09969	.60634	-.04913
.63984	.09191	.65317	-.04392
.68387	.08192	.69967	-.03701
.72779	.07087	.74564	-.02924
.77085	.05960	.79051	-.02150
.81221	.04865	.83342	-.01447
.85106	.03842	.87341	-.00861
.88653	.02908	.90948	-.00420
.91803	.02060	.94065	-.00132
.94528	.01309	.96599	.00013
.96792	.00701	.98470	.00046
.98522	.00281	.99615	.00020
.99621	.00061	1.00000	.00000
1.00000	.00000		

Table – 4.1(b) Co-ordinate values of airfoil S 818 (Source: Somer, 1992)

Upper Surface		Lower Surface	
x/c	y/c	x/c	y/c
0.00012	0.00170	0.00003	-0.00087
.00066	.00442	.00048	-.00341
.00374	.01205	.00141	-.00608
.01259	.02437	.00328	-.00985
.02619	.03717	.01232	-.02157
.04424	.05009	.02631	-.03391
.06647	.06284	.04486	-.04650
.09256	.07518	.06764	-.05923
.12213	.08681	.09404	-.07200
.15482	.09745	.12331	-.08444
.19023	.10678	.15489	-.09598
.22797	.11449	.18823	-.10622
.26760	.12006	.22238	-.11444
.30915	.12285	.25700	-.11893
.35312	.12287	.29323	-.11847
.39944	.12073	.33232	-.11328
.44760	.11690	.37488	-.10412
.49702	.11165	.42102	-.09200
.54711	.10527	.47043	-.07786
.59727	.09798	.52267	-.06258
.64685	.09003	.57709	-.04706
.69521	.08161	.63288	-.03217
.74169	.07292	.68903	-.01872
.78569	.06409	.74437	-.00740
.82657	.05526	.79758	.00128
.86377	.04651	.84726	.00704
.89672	.03779	.89200	.00985
.92522	.02885	.93046	.00996
.94958	.01983	.96144	.00780
.96996	.01155	.98351	.00422
.98590	.00509	.99606	.00113
.99633	.00122	1.00000	.00000
1.00000	.00000		

Table 4.2 Blade details at various sections

Radial Station r mm	Span wise Station z mm	Span wise Station z/L %	Chord c mm	Thickness t mm	Thickness to Chord Ratio t/c %	Twist Θ ($^{\circ}$)	Airfoil combinations
816	0	0.0	1310.0	1310.0	100.0	0.0	Cylinder
1150	334	1.4	1310.0	1310.0	100.0	0.0	Cylinder
2300	1484	6.4	1323.0	1294.0	97.8	0.0	97.1% cylinder & 2.9% S818
3450	2634	11.4	1672.0	1141.0	68.2	18.52	58.2% cylinder & 41.8% S818
4600	3784	16.3	2000.0	781.0	39.1	16.34	19.8% cylinder & 80.2% S818
5750	4934	21.3	2263.9	545.9	24.1	14.22	S818
6900	6084	26.2	2222.1	517.0	23.3	11.31	75.5% S818 & 24.5% S816
8050	7234	31.2	2165.5	490.4	22.6	9.10	54.9% S818 & 45.1% S816
9200	8384	36.2	2096.3	465.5	22.2	7.38	40.2% S818 & 59.8% S816
10350	9534	41.1	2016.5	442.3	21.9	5.99	31.1% S818 & 68.9% S816
11500	10684	46.1	1929.5	419.2	21.7	4.84	24.8% S818 & 75.8% S816
12650	11834	51.0	1832.6	394.1	21.5	3.90	16.2% S818 & 83.2% S816
13800	12984	56.0	1728.3	363.2	21.0	3.12	S816
14950	14134	61.0	1616.3	323.0	20.0	2.42	79.7% S816 & 20.3% S817
16100	15284	65.9	1499.1	278.3	18.6	1.87	51.3% S816 & 48.7% S817
17250	16434	70.9	1376.1	234.9	17.1	1.35	21.3% S816 & 78.7% S817
18400	17584	75.8	1245.7	199.3	16.0	0.91	S817
19550	18734	80.8	1111.1	177.8	16.0	0.51	S817
20700	19884	85.8	969.0	155.0	16.0	0.16	S817
21850	21034	90.7	824.9	132.0	16.0	-0.12	S817
23000	23184	95.7	682.6	109.2	16.0	-0.41	S817
25000	24184	100.0	436.0	69.8	16.0	-0.41	S817

Using the modeling software Catia V5, the profile of the airfoils of the subject HAWT were drawn individually and spaced at the span wise distance as mentioned in the Table 4.2. The profile with twist angle is shown in Figure 4.3.

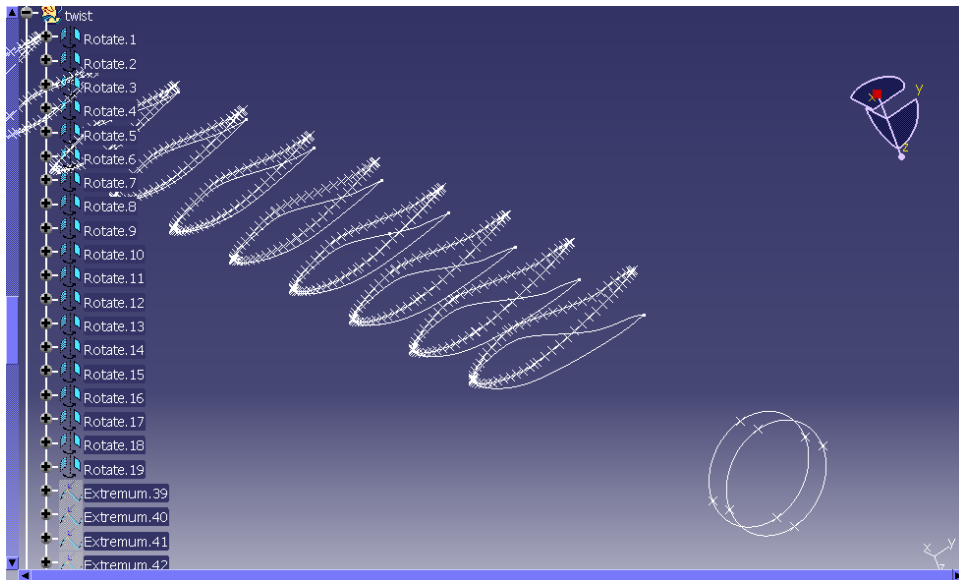


Figure 4.3 Modeling the airfoils of the blade.

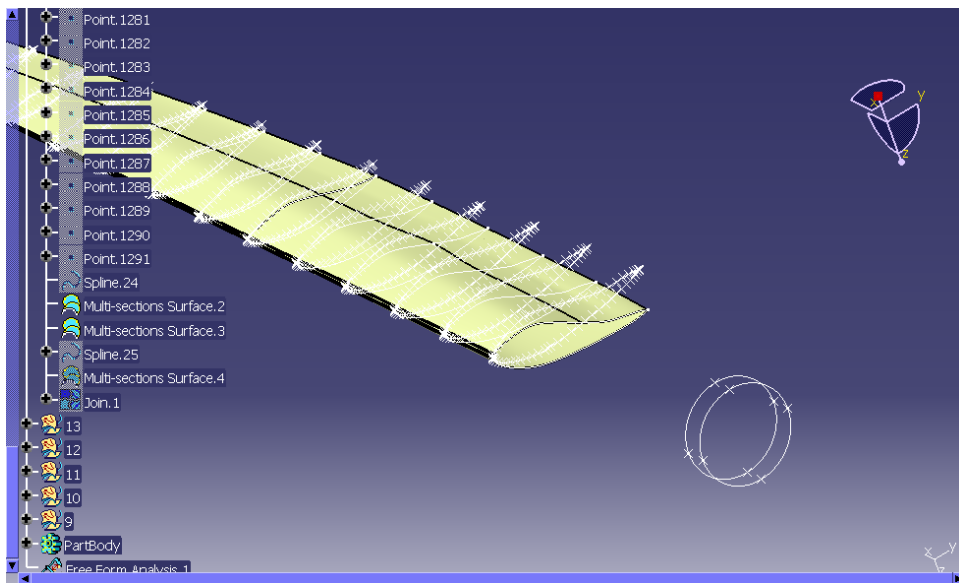


Figure 4.4 Lofting of the airfoil sections.

These airfoils are lofted together to create the blade model surface having zero thickness as shown in *Figures 4.4 and 4.5*

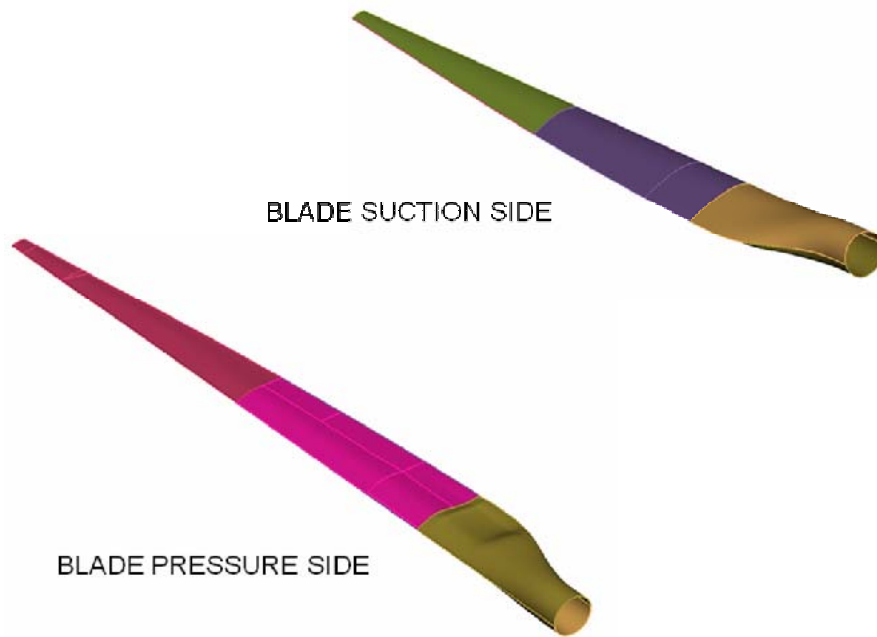


Figure 4.5 Blades modeling with suction and pressure sides

In the report prepared by the NREL, it is mentioned that the hub height of the HAWT made with tubular tower is 50 m. This hub height is used on the present analyses. From *Table 4.2*, it could be calculated that the hub diameter is 1633 mm. The nacelle is also modeled with the assumptions of dimensions in accordance with the standard wind mills of 750 kW capacities. The roots of the three blades are connected to the hub, and they are kept 120° apart from each other at the plane of rotation. These blades have an inclination of 3° towards the direction of the wind flow in order to avoid the blade tip towards the tower. The profiles of hub and nacelle do not play any significant role in the aerodynamic performance of HAWT.

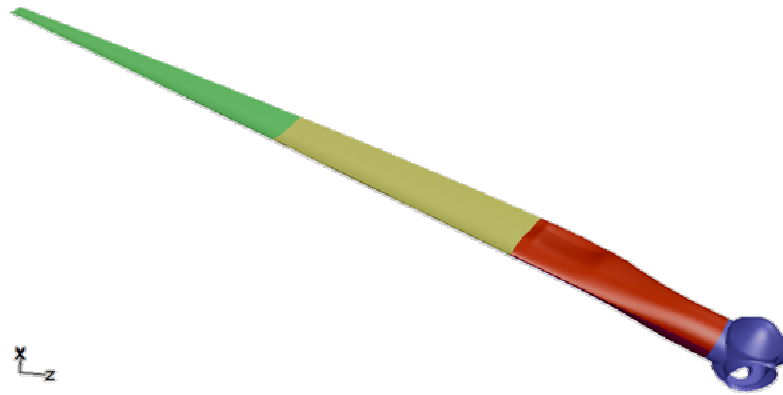


Figure 4.6 Assembly of blade and hub

Further the nacelle is kept on top of the tower of HAWT facing the wind. It is tilted upwards by an angle 4° known as tilt angle. The purpose of the tilt is to avoid the blade tip touching the tower. This is shown in *Figure 4.7*.

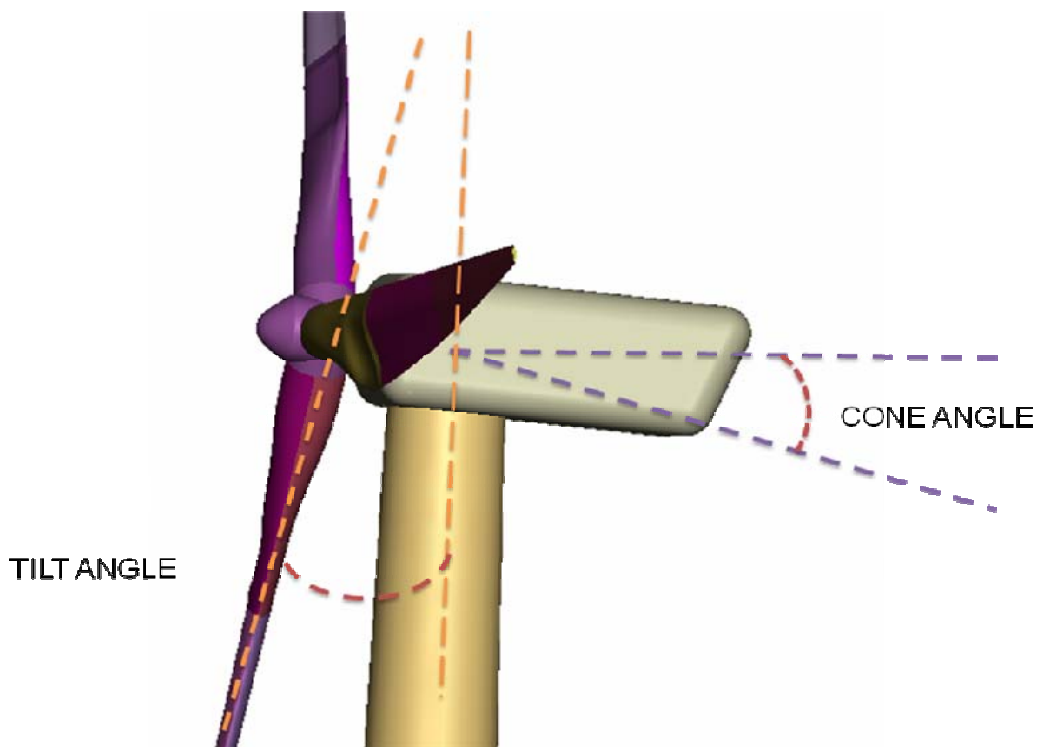


Figure 4.7 Assembly constraints cone angle, tilt angle.



Figure 4.8 Complete model of windmill

Figure 4.8 shows the complete assembly of the three blades equally spaced apart by 120° and connected to the hub which is a part of the nacelle. The whole blades and nacelle assembly is placed on top of the upright tubular tower.

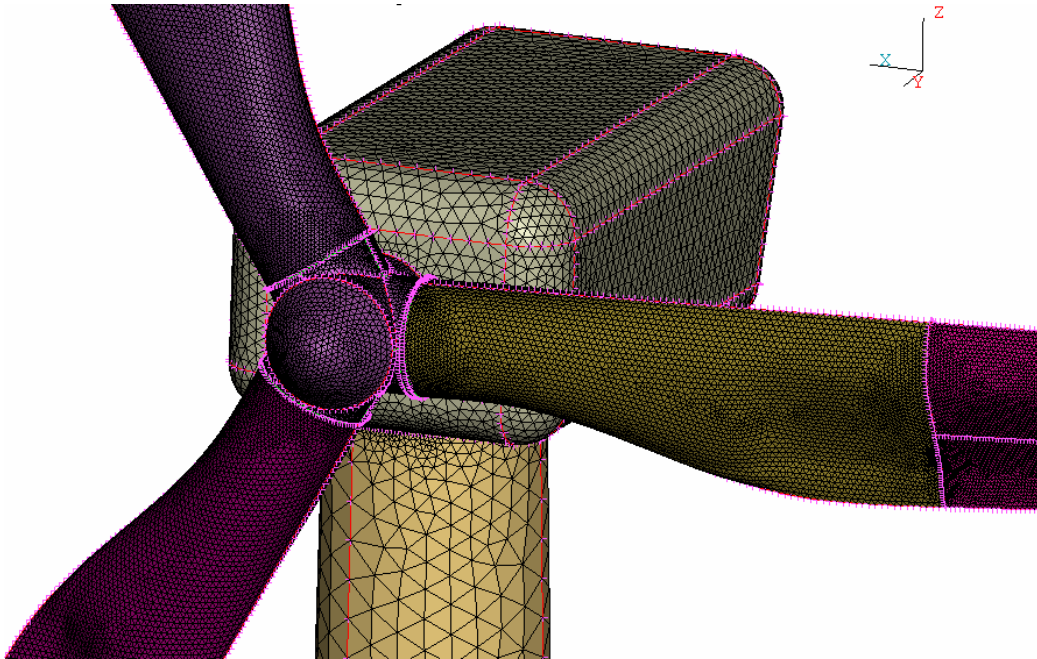


Figure 4.9 Discretization of parts of the HAWT

In the field study conducted by the NREL, the HAWT was erected on the flat ground as per standards. The distance to be kept between the two HAWTs is based on the wind flow pattern (NREL hand book). In the line of wind flow the HAWT should be placed at a distance of 7 times the swept diameter (D) of the HAWT. The sideward clearances between adjoining towers of HAWTs are to be kept at minimum $3D$ to maximum $8D$ in practical. In the present study the rectangular domain having $5D$ width, $10D$ length and $3D$ height is constructed. The wind turbine is kept in this domain at a distance of $2.5D$ from the inlet. The dimensions for the present study of HAWT were assumed after a thorough analysis of the result values of domain sizes which are shown in *Figures 4.10 and, 4.11*.

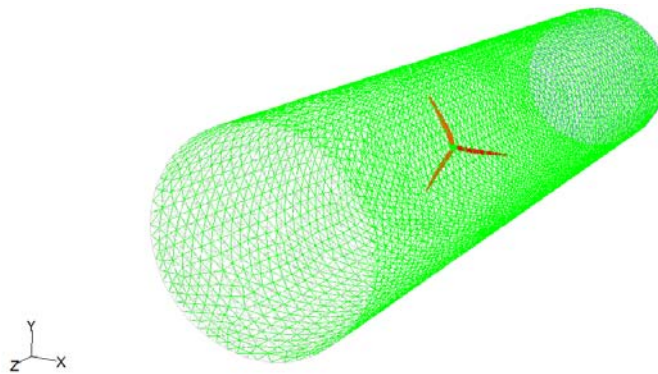


Figure 4.10 Cylindrical domains

The domains selected for the numerical analysis of the HAWT were cylindrical and cubical in shape. The diameter of cylindrical domains and the side of the cubical domain were taken as 150 m.

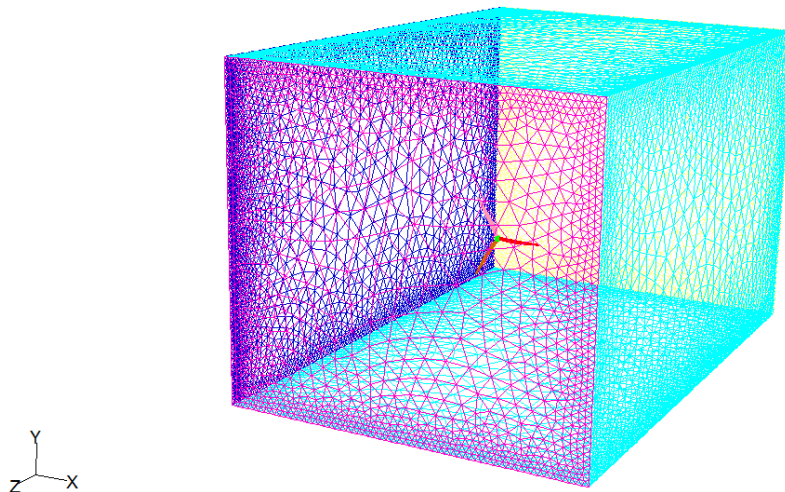


Figure 4.11 Cubical domains

The final selected domain size which is shown in the Figure 4.12 falls within the sizes presented in NREL hand book.

4.4 Discretization of Volumes

The various parts of the models are separated into small surface elements. The sizes of the surface areas are carefully selected by giving

importance to flow physics. The blades of the HAWT are given prominence as their aero-dynamical behavior decides the performance of the wind mills. Hence they are given the smallest sizes of surface meshing as shown in the *Figure 4.9*. The other components such as nacelle and tower are passive elements and they are given normal mesh sizes. The tetrahedral elements are used for this surface meshing because of their ability to maintain the geometry of the critical parts of the HAWT. The schematic diagram as shown in *Figure 4.12* and *Figure 4.13* describes the domain shape and sizes and the location of HAWT in the domain.

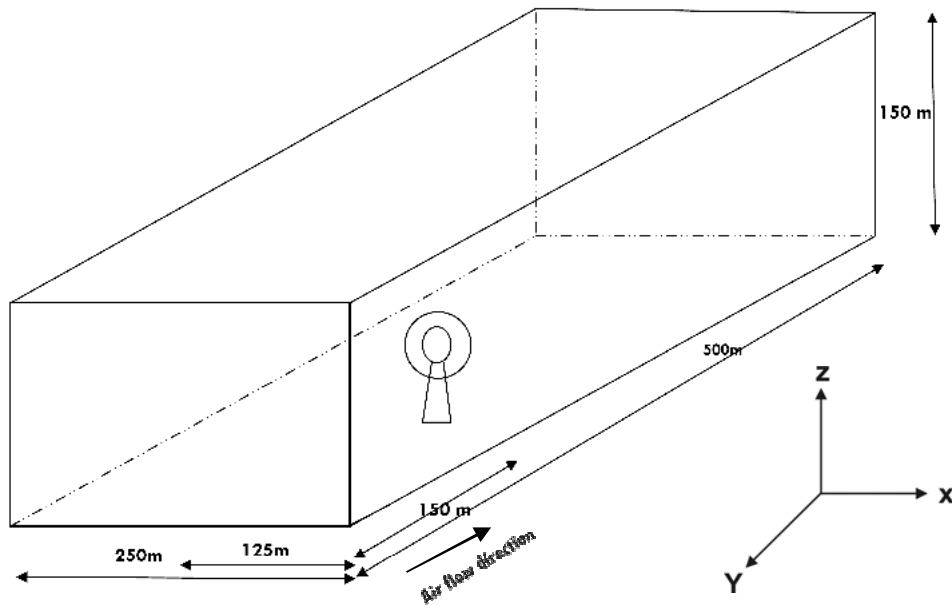


Figure 4.12 Location of wind turbine in the computational domain

4.5 MULTIPLE ROTATING FRAMES

The most important feature of the present research work is the analysis of HAWT under multi-body dynamic condition. The tower blade interaction and the relative dynamics of rotating bodies are governed by the multi-body

dynamics. For achieving the flow of wind over the HAWT the sliding mesh algorithm was used in the research work done by Iradi *et.al*, (2009).

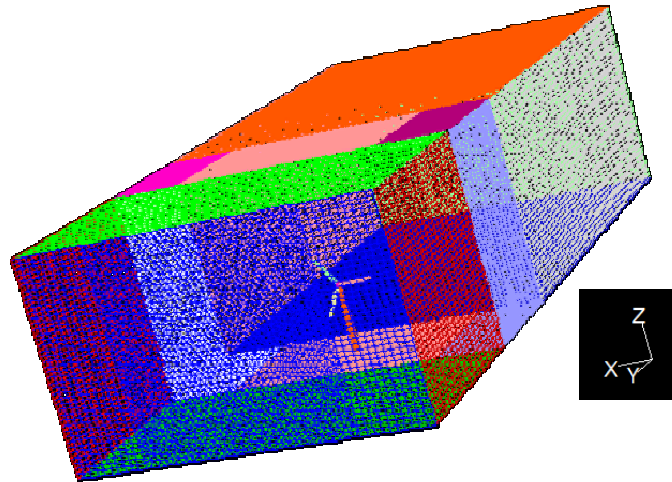


Figure 4.13 Volume zones for analysis

The turbo machines are analyzed in CFD with rotating reference frame techniques. The single rotating frame and multiple rotating frames are the commonly used techniques for the turbo machinery problems. Since only a few researches have used these techniques on HAWT the present research gives more importance. The regions around the three blades of the HAWT are covered along the space of rotational volume. They are created as a separate zone named as MRF zone as shown in the *Figure 4.14*. This MRF zone carefully avoids the stationary components of the HAWT such as nacelle and tower, but it includes the rotating blades and hub. This zone is given the rotational speed relative to adjoining cell zones as defined in the problem and given as boundary conditions for the present numerical analysis. The MRF zone is created with the tetrahedral meshes with good accuracy level.

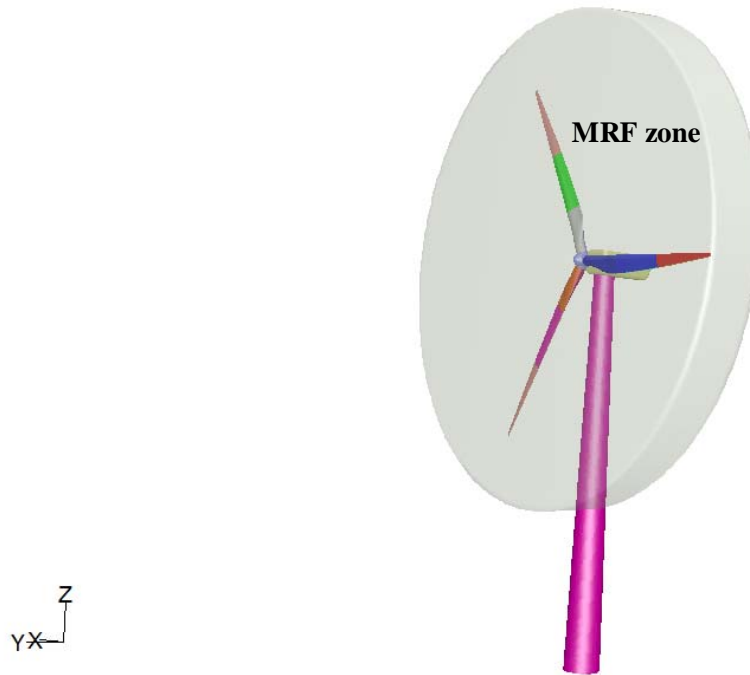


Figure 4.14 MRF zone in the assembly of HAWT

4.6 Boundary Conditions

In the present numerical methodology for the selected HAWT, the inlet is considered as velocity inlet as intended for incompressible flows. This approach ensures that the solution will not be non-physical. The velocity inlet is placed at a distance of 200 metres (*i.e.*, 4D) ahead of the HAWT centre. Pressure outlet boundary condition requires the specification of a static pressure at the outlet boundary. In the present study, the turbulence intensity and hydraulic diameter account for the turbulence parameter. At 5% turbulence intensity the flow is fully developed (Patel, 1999).

4.6.1 Wall Boundaries

The blades of the HAWT are considered as fixed walls around which fluid cells are assumed to be rotating relative to the adjacent walls. In this

present analysis all interior zones such as inlet, outlet, turbine zone and MRF zone are fluid cell zones for which all active equations are solved. MRF zone is defined as fluid cell zone rotating at 25 rpm relative to adjacent blade wall zone. Fluid material is air with a density of 1.225 kg/m^3 and with standard physical properties (Wang, 2008).

4.6.2 Solution Methods

This present research work used finite volume method of fluid flow and discretization. The equations are normally solved for convergence of continuity and product of k and ω . The numerical scheme used to solve the equations is of second order upwind scheme which is more accurate than first order. Segregated SIMPLE algorithm was used to perform the study on HAWT (Yang, 2005).

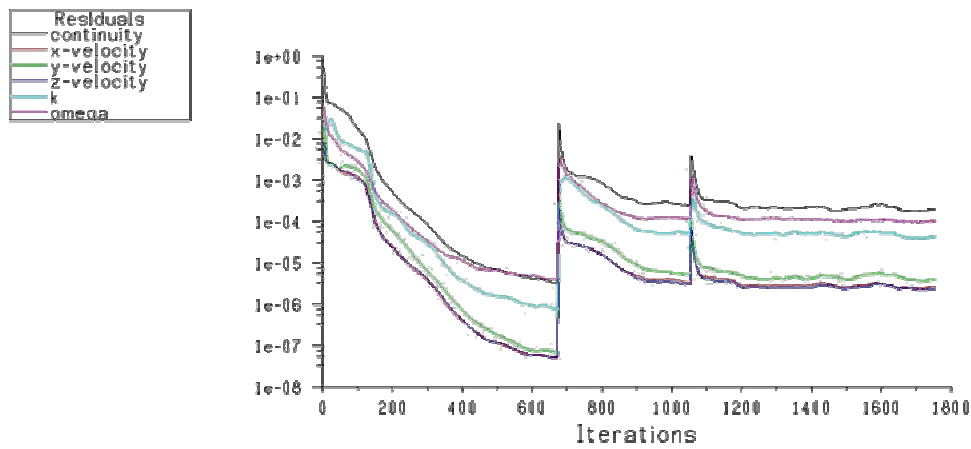


Figure 4.15 Iteration statuses with convergence

Figure 4.15 shows the status of residual values. It also shows the residuals of x , y , z velocities and k , ω and their convergence. Y axis shows the residuals levels and X axis is the number of iterations.

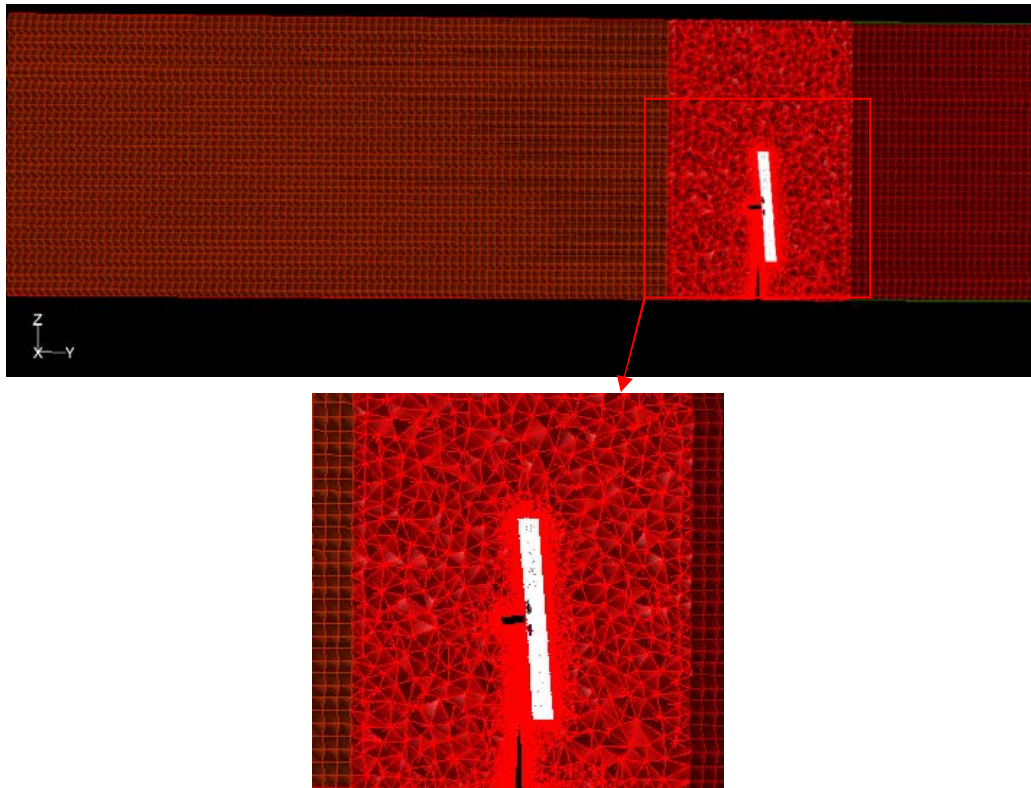


Figure 4.16 Cross sectional view of the domain of analysis

Figure 4.16 shows the cross-section of the total domain. The air enters from -Y direction and the inlet zone as well as the outlet zone has the prism cells. The entire MRF zone has very fine meshes of tetrahedrons and again with fine tetrahedron meshes around it in the middle part of the whole domain.

4.6.3 Turbulence Model

The turbulence model used in the present research work for the numerical analyses is Wilcox $k-\omega$ model which incorporates modifications for low-Reynolds-number effects. The $k-\omega$ model was developed to effectively blend the robust and accurate formulation of the $k-\epsilon$ model (Launder, 1972, Choudhury, 1993) in the near-wall region with the free stream independence of the $k-\epsilon$ model in the far field. These features make the shear stress transport

(SST) k- ω -Model (Menter, 1994) more accurate and reliable than the standard k- ϵ model. Other modifications include the addition of cross diffusion term in the ω equation and a blending function to ensure that the model equations behave appropriately in both the near- wall of the blades and far-field zones. Double precision pressure based solution is used in this present research work to get good predicted results (Amano 2009, Liu 2010).

Grid size in the range of 3.2 million was optimised by the grid independence study in the present research work. The domain used for this CFD project was the same as for the field and hence no question arises regarding the domain independence. The MRF domain was created for the rotational affect of blades. This was correctly done with effectively limiting to the rotating blade region avoiding the stationery parts such as nacelle and tower (Ebert 2002, Pilmoor 2006). Tetrahedron cells were used to mesh the turbine region and MRF region. The bottom portion of the model (ground) was given a suitable surface roughness value to get the effects of log-law layer on wind speed variation. This variation is known as the wind shear. The grid quality was well maintained within allowable limits by proper grid check surface mesh skewness 0.85, and volume mesh 0.65. The gird has to be generated in mm and to be properly scaled. The direction of wind and rotation of relative cell zones in the rotating region is to be given correctly. Residuals are to be achieved for continuity, x, y and z velocities to the convergence level of 1e-06 as prescribed for pressure based solution.

4.7 Power Calculation

The field results of the turbine validation program are validated with numerical solution in the present research. The CFD results will give aero dynamical power generator by the HAWT model. The gear box used in the HAWT taken for present study has efficiency around 97-98 %. The generator used in this type of HAWT taken for present study has efficiency around 95 %. (Johnson,1985).

Table 4.3 Pressure moment, viscous moment

Zone name	Pressure moment (N-m)			Viscous moment (N-m)			Total moment (N-m)		
	x	y	z	x	y	z	x	y	z
Blade-A									
Blade-B									
Blade-C									
Hub									
Net									

Table 4.3 shows the template for the pressure moment and viscous moment generated by the blades A, B and C in X, Y, Z axis.

4.8 Validation of CFD Approach for HAWT Analysis

In this part of the study, the performances evaluation of the horizontal axis wind turbine is carried out and its general aerodynamic behavior is studied. This section demonstrates the potential of an incompressible Navier–Stokes CFD method for the analysis of horizontal axis wind turbines. The method has to be validated against experimental data of the NREL power performance testing activities (Vanden, 2000). The performance assessment of Zond 750 kW- a non yawed isolated HAWT of a wind farm was carried out. This present study aims to compare the surface pressure distributions at several stations along the blades with the CFD results for the local flow angles at several stations ahead of the wind turbine. For attached and moderately stalled flow conditions the pressure distribution and torque predictions are to be calculated. Subsequently, the wind-field effects on the blade aerodynamics, as well as the blade/tower interaction, are to be investigated. The case selected for the study corresponds to 12.5 m/s up-wind turbine at zero deg of yaw angle with a

rotational speed of 25 rpm. The result obtained is expected to suggest that the present method can cope well with the flows encountered around wind turbines. The results should be useful for assessing the aerodynamics performance of the HAWT. They are also expected to reveal the flow pattern details near and off the blades and tower (Baxevanou, 2008).

4.9 Studies on HAWT using CFD

The current trend towards different varieties of wind turbine rotors brings new challenges to wind turbine manufactures. These wind turbine rotors were mainly designed for efficient field performance and to tolerate high loads. Due to the higher weight ratios the flow properties over the heavy blade may affect the performance and the machine may operate near to stall. Due to this reason, accurate CFD methods are inevitable and several studies documenting the applications of CFD to wind turbine appears frequently in literature. But only few studies are available in literature on the rotors at dynamic condition considering the effect of the tower. Normal Mach no. speeds less than 0.3 are widely used in application and hence the flow may be treated as incompressible. Hence incompressible Navier Stokes equations are used in the present study.

Bennett and Edwards (1998) have developed the CFD coding of CAP-TSDV - Euler and Navier-Stokes type. The methodology followed in their work involved preprocessing of the geometry and model data, the execution of the CFD computer program, and the post processing of the output data. The present research work follows the same sequence.

Bermudez *et al.*, (2000) studied the steady and unsteady aerodynamics behavior of horizontal-axis wind turbines. The experimental results based on the variables such as air velocity, inflow angles, and yaw angle ensured the existence of flow forces, moments and separation. The validation of the

computed model was done with experimental results. The experimental data from the NREL- HAWT study was used for validation. The aero elastic numerical model used the Navier–Stokes CFD solver for the study of flutter introduction over the model.

Ebert and Wood (2002) in their paper showed, that the CFD results had good agreement with the experimental validation. They concluded that CFD results appear to capture all the expected features of flow including root and tip vortices, as well as the interaction between the tower and the wake of the blades. The study proved that the blade tower interaction resulted in reduction the rotor thrust and torque.

Baxevanou *et al.*, (2008) investigated the performance of the flutter on aero elastic behavior. A new Navier–Stokes CFD aero elastic model with two coupling schemes (explicit and implicit) and two turbulence models (with wall functions and wall treatment) were presented and evaluated against linear theory and existing numerical results.

Lazim *et al.*, (2004) had done a computational fluid dynamics and experimental study over the air craft model to predict the pressure distribution and aerodynamic characteristics. The CFD simulation was carried out at wind speed of 22 m/s assuming incompressible laminar flow. Then a comparative study was made between the experimental and numerical results.

Tholudin Mat Lazim *et al.*, (2004) conducted an aerodynamic study over the model blade sections. The aerodynamic coupling caused by blade motions was represented using the single family of modes approach in the equations of motion. The investigation was focused on the forced response amplification factors in FEA method. The unsteady aerodynamic forces were computed using computational fluid dynamics (CFD).

The work of Corbus and Meadors (2005) provided the real time experimental validation of SWAT wind turbine. The results of their analysis showed agreement between thrust and torque over varying wind speed. They also demonstrated the performance of two blade wind mill model placed in the octagonal wind tunnel. The results obtained were in contrast to tip vortices which contain angular momentum in the direction opposite to the one which was generating the blade torque. The increase in radius had lead to increase in thrust generation. The tip vortices had high turbulence. Its pitch was approximately constant over the range of measurements with a value that was shown to be consistent with the results from propeller wakes.

In the analysis of Richard Farmer *et al.*, (2005), the extrapolation of the variables such as tip speed ratio, propeller thrust coefficient, turbine thrust coefficient and power coefficient was done. The coordinate systems for the NACA 63-8 xx foil section with 18 % thickness were used.

Hansen et al investigated the aerodynamic performance of a horizontal axis wind turbine (HAWT), by the combination of momentum and BEM theories. The numerical investigation was done by considering outer blade diameter and tangential induction factor of the wake rotation as initial conditions. The results obtained were found to be in agreement with the variable pitch control output system, the blade drag dissipation and wake distributions.

Pilmoor *et al.*, (2006) projected and exhibited the flow control techniques with wind tunnel validation. The results on the wake structures of NACA 0012 airfoils were obtained with the Euler solver and were validated with experimental results. The flow separation with concentrated vortices formation was also observed.

Yang *et al.*, (2006) had done a sub sonic flow analysis over the sinusoidal pitching airfoil NACA 0012 with the mean angle of attack. The pressure distribution and the aerodynamic loading on the blade at the mean angle of attack were studied with Euler flow solver.

Farmer *et al.*, (2006) have done CFD analysis of the complex flow processes. Their paper projected the high-pressure turbulence models and the aerodynamic behavior. The multi grid convergence accelerator and pseudo-compressibility factors were simulated under incompressible flow using the coupled solution technique.

Miyakozawa *et al.*, (2009), focused on the validation study of the wind turbine to enhance the performance by scoop design. The methodology formulated could be validated for the future work over a new rotor blade system along with scoop. The modified design resulted in the increase of power generation with respect to varying wind speed conditions. The CFD tool over the scoop model validated the wind turbine, experimentally and numerically in predicting the power performance. In the wind tunnel test, the pressure and velocity distribution were measured and compared against the CFD predicted results. The model was tested at the wind speeds of 9.1 m/s, 11.25 m/s and 13.9 m/s and the power curves were plotted.

A comprehensive study of the wind turbine was carried out using the aero elasticity concept by the mathematical model and numerical simulation. This study was done by predicting the aerodynamic load on the wind turbine blade using blade element momentum method with major complexity in calculations and numerical simulations on rotors. The experimental work was carried out with vortex and panel methods. The finite element method (FEM) discretization and a multi-body formulation, was studied by Gomez-Iradi *et al.*, (2009).

A constant rotation rate was assumed for the blade by Amano (2009) and investigations were carried out by CFD. The optimization of the blades was carried out at 7 m/s wind speed. The optimization was focused on straight edge blade, the angle of attack and chord length for the given airfoil cross section at different positions along the blade. The swept edge geometry maintains maximum efficiency at lower on coming wind speeds. It delays the stall point resulting in an increase in power at higher oncoming wind speeds.

The turbine as well as tower behavior was studied by installing many sensors on it, ‘to predict the aerodynamic behavior such as furl, yaw angle and power generated, rotor speed, thrust and torque over the wind speeds’. This study done by Fei liu (2010) also served as a supporting document for obtaining the various coordinates of the foil section.

Liu (2010) presented a numerical study for HAWT wind turbine with the PANEL method approach, for predicting the performance of the wind turbine. The formulation and execution of the Panel method approach was done with various fluid properties such as viscosity/density and Reynolds number. Their aim was to reduce the negative pressure and stall effect along with cavitations exposure which leads to more extraction of power.

4.10 CFD results Validation

CFD can be used as a tool for calculating the aero dynamical power. The effects of airfoil shape, size, interaction with flowing air and tower effects are large enough to be calculated and the cost involved is high. Making proto-types of rotors for analysing is time consuming and alternatively narrowing the options to CFD. For the present study, the 750 kW Zond 50 HAWT was considered whose rotors are made up of family of airfoils generated by NREL.

When it comes to wind turbine design, CFD is frequently used as a tool for the development of new wind turbine aerofoils and blades. It can also be exploited for tower and nacelle analysis. CFD offers cost advantages and reduced risks with respect to the use of scaled wind-tunnel test result data (Ebert, 2002).

The above aspect is related to the difficulties in achieving the same tip speed ratio, the same Reynolds and Mach numbers as well as the precise operational parameters of a full size wind turbine in a wind tunnel during the experiment. However, uncertainties regarding in-field measurements make wind-tunnel data more suitable for initial validation of CFD solvers (Ebert 2002). Further, wind tunnels offer carefully controlled conditions and refined measurement techniques which are not available in wind turbine farms. On the other hand, the majority of the available wind-tunnel data concern scaled turbines and do not match the conditions experienced by wind turbines in situ. The main discrepancies are related to the lower Reynolds numbers usually achieved in tunnels, when the tip-speed ratio (tip speed of the blade / wind speed) is maintained close to the real values.

The definition of the blade geometry of the NREL phase VI experiments considered the coordinates of the employed S809 section, the taper of the blade, as well as the twist distribution and the blade pitch. The tip and root sections were not defined in a unique way, and the authors have made an attempt to quantify these effects (Hansen, 2006).

The factors influencing the performance of HAWT are

- Swept area
- Hub height

The air Properties, turbulence and ground roughness are taken as constraints for computation. Other parameters like tip speed ratios; relative velocity and angle of attack are optimised to harness maximum energy from wind.

Table 4.4 shows the pressure moment and viscous moment at X, Y, Z axis of rotation of the blade A, B and C.

Table 4.4 Pressure moment and viscous moment

Zone name	Pressure moment (N-m)			Viscous moment (N-m)			Total moment (N-m)		
	x	y	z	x	y	z	x	y	z
Blade-A	3379.98	53115.4	532032	-335.4	5057.5	-370.39	3044.58	58173	531662
Blade-B	-342105.8	64113.1	-193199	223.72	1419.6	92.2063	-341882	65532	-193107
Blade-C	376591.16	193660.	-382304	48.548	6022.9	1037.01	376639.	199682	-381267
Hub	-27.51740	0.36042	-75.1600	-0.131	0.4874	-1.6791	-27.649	0.8478	-76.839
Net	37837.765	310888	-43546.0	-63.25	12500.	757.144	37774.5	323389	

4.11 Results and Discussion

The following figures illustrate the post processed numerically arrived results.

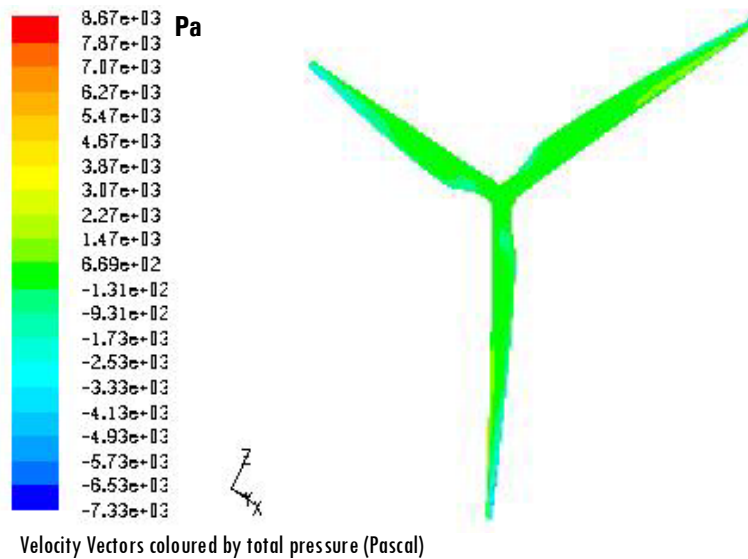


Figure 4.17 Pressure vector contour

Figure 4.17 shows the velocity vectors of the blade surfaces, and it is seen that the centre and trailing edges of all the three blades have negative values which confirm higher velocities

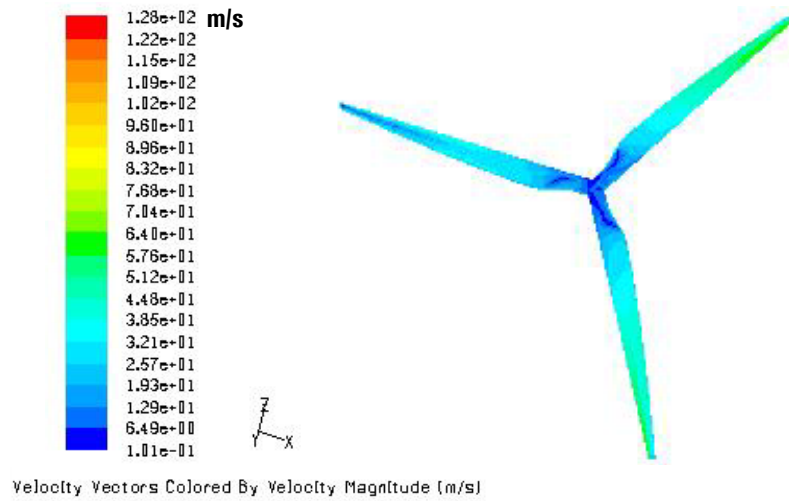


Figure 4.18 Velocity vector contour

Figure 4.18 shows the velocity vectors of the blade surfaces, and it is seen that the centre region of all the three blades have velocity values 6.5 m/s to 10 m/s compared to higher velocity at the outer and trailing edge zones.

Velocity vector is in accordance with the concept shown in *Figure 4.18*. The relative velocity at the tip of the blade is around 60 m/s. The undisturbed free stream velocity 12.5 m/s of air is lowered at root and increased at tip regions of the blade because of the functioning of the HAWT.

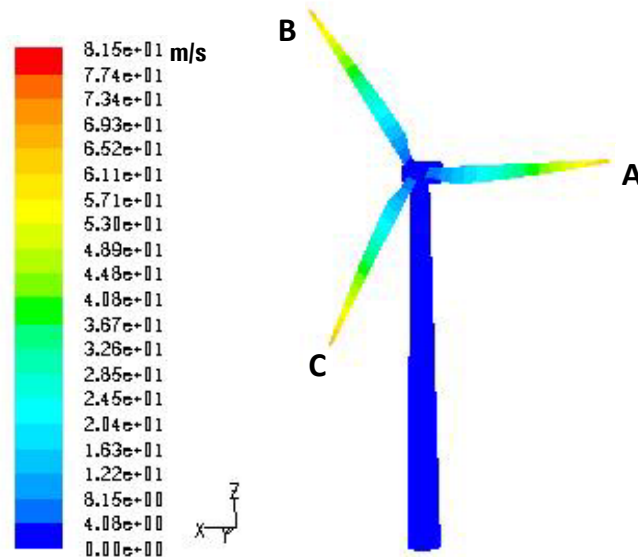


Figure 4.19 Velocity vector contour along with Tower

Figure 4.19 shows the velocity magnitudes of the blade surfaces and tower, and it is found that the centre region of all the three blades have velocity values 6.5 m/s to 10 m/s, compared to higher velocities around 60 m/s at the outer tips. However the outer tips and trailing edge zones exhibit higher velocity when compared to the trailing edge at the root of the blade.

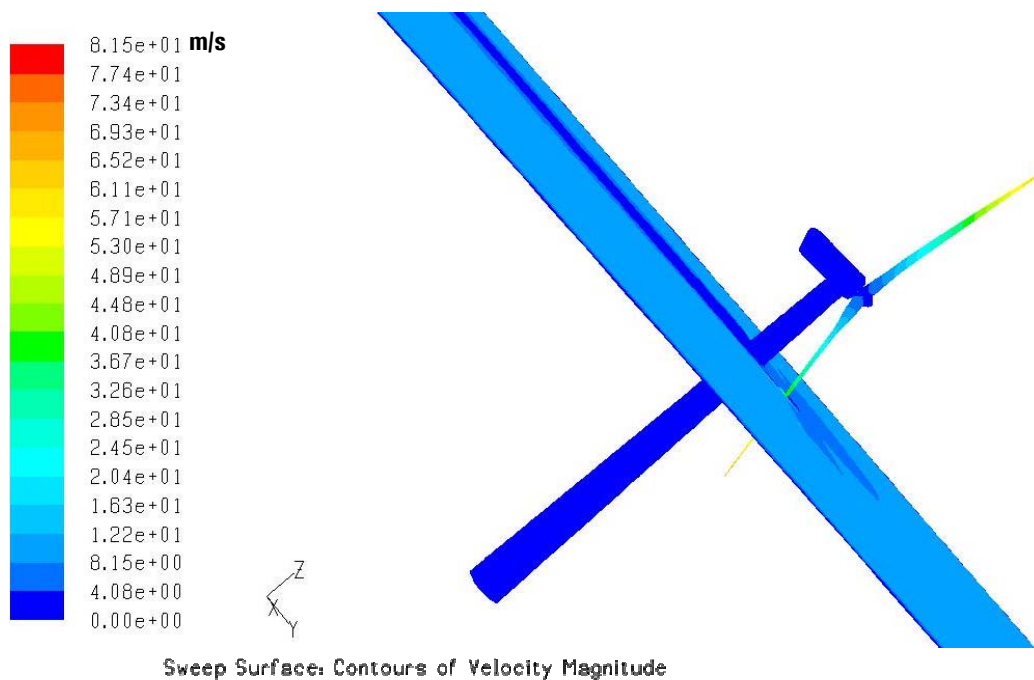


Figure 4.20 Velocity vector contour along with Tower –sweep surface –Z direction

The sweep surface created in Z axis (*Figure 4.20*) shows the velocity vectors which depict the nil velocities of non moving zones such as tower and nacelle. The zone in front of the tower has a low velocity (around 10 m/s) similar to the zone behind the tower. But the effect of tower shadow and the tower blade interaction creates a lesser velocity of (around 4 m/s and 0 m/s) respectively ahead and behind the tower.

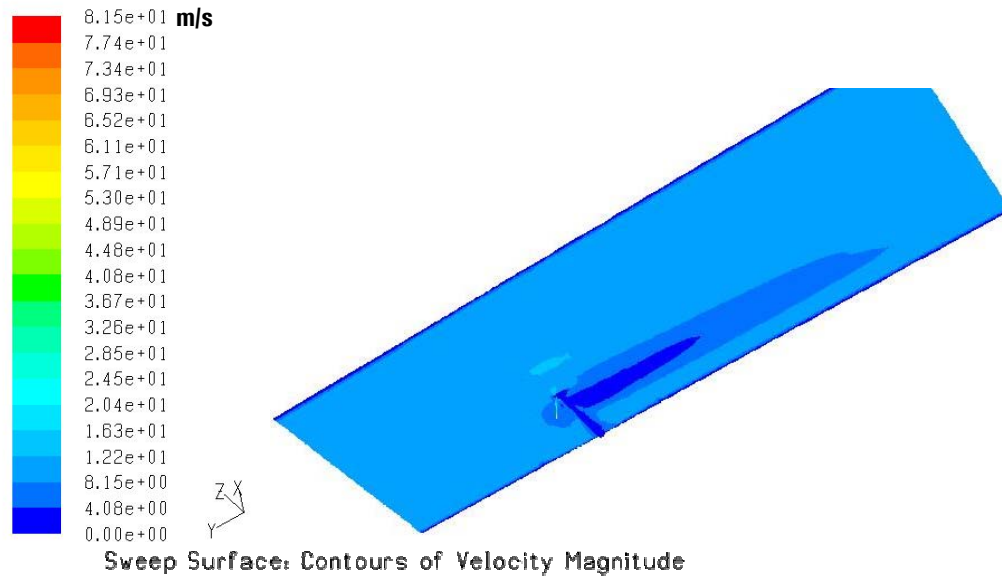


Figure 4.21 Velocity vector contour along with Tower –sweep surface –Y plane

Figure 4.21 shows the velocity vector contour in the region behind the wind turbine.

The present analysis is more important as it can determine the scientific distance between two successive HAWTs. The free flowing wind with undisturbed velocity of 12.5 m/s is altered because of the functioning of HAWT. The velocity of the wind drops when the kinetic energy of wind is converted to rotational mechanical energy. Thus the wind leaving the HAWT is having lower velocity. When it travels further away from the HAWT and joins the rest of the wind, it resumes the old velocity of 12.5 m/s. The velocity of air in front and behind the turbine can be predicted by the velocity vector contour plotted on the sweep surface created in the Y plane as shown in *Figure 4.21*

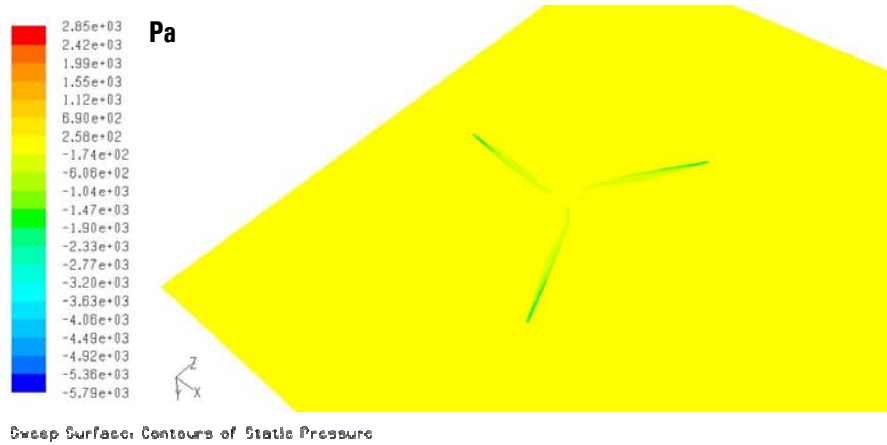


Figure 4.22 Pressure vector contours of the three blades along with Sweep surface in Z direction

Sweep surface along Z direction created to analyse the pressure vector of the three blades as shown in *Figure 4.22* and *Figure 4.23*. This creation of sweep surfaces helps in predicting the pressure contour along the plane of sweep surface. The sweep surface can be moved and the pressure can be analysed.

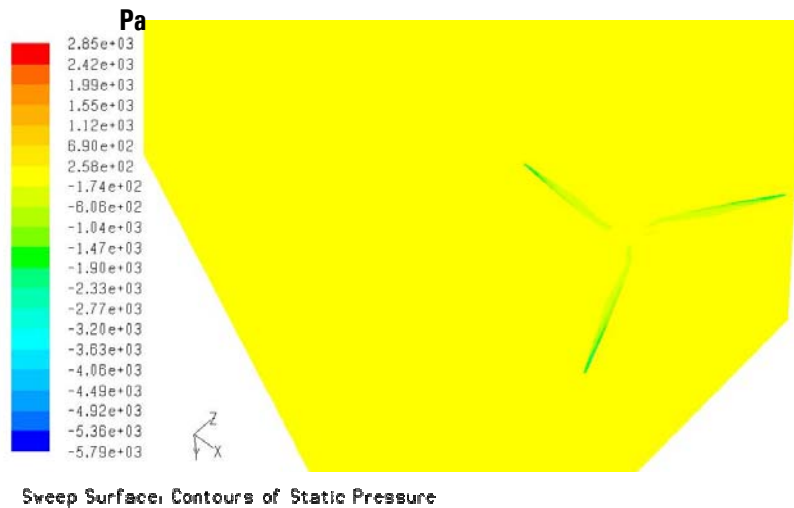


Figure 4.23 Pressure vector contours of the three blades along with Tower –Sweep surface in Z direction

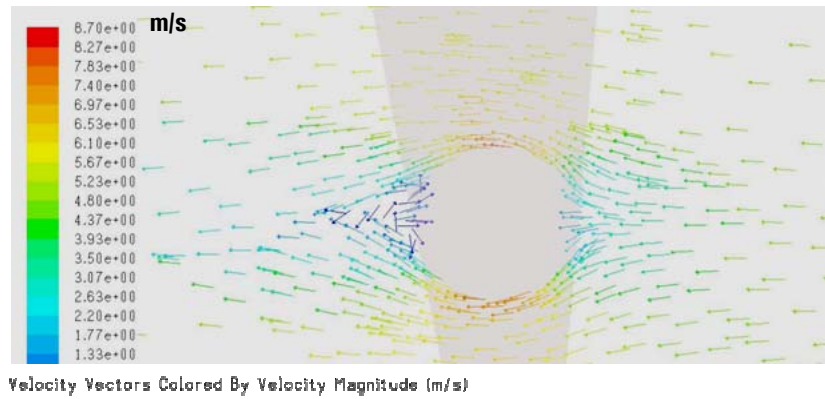


Figure 4.24 velocity vectors around the tower

Figure 4.24 shows the velocity of air flowing around the tower confirming stagnation in the leading edge of the tower and respective shadow effects. This can be further examined and compared with other types of towers.

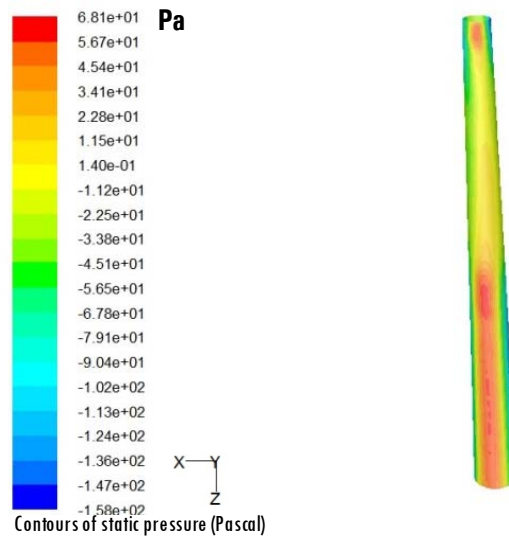


Figure 4.25 Static pressure on the tower surface viewed from -Y direction.

The free flowing air hits the tower and creates high static pressure over the lower part of the tower surface facing the wind as shown in *Figure 4.25*. The upper part of the tower experiences negative static pressure because of blade-tower interaction.

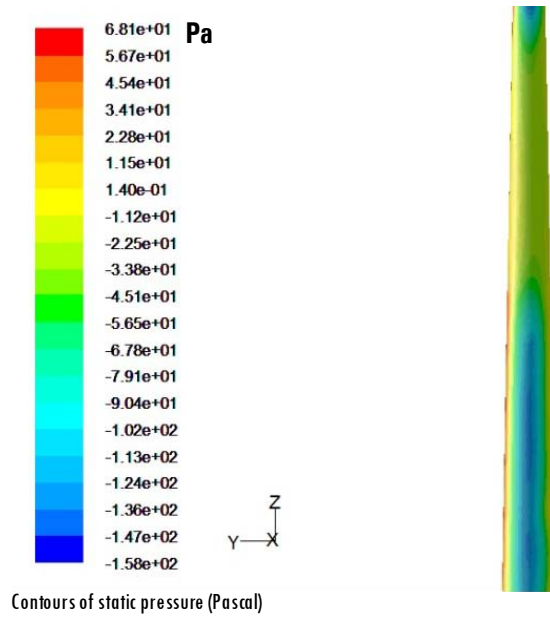


Figure 4.26 Static pressure on the tower surface viewed from X direction.

The wind flow over the tower creates suction pressure over the surfaces of the tower side perpendicular to the flow direction of wind. This low suction pressure distribution is clearly shown in *Figure 4.26*.

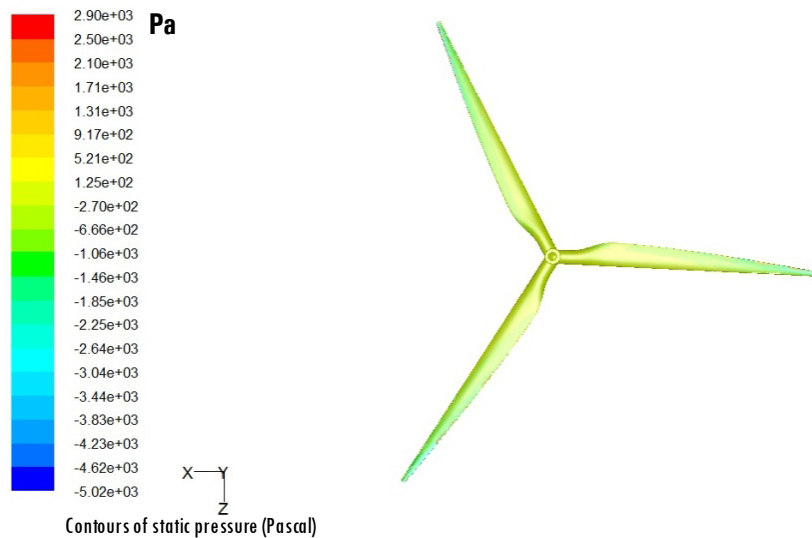


Figure 4.27 Static pressure contour over the three blades viewed from the outlet side.

As shown in the *Figure 4.27* when compared to the trailing edges the leading edges experience higher static pressures.

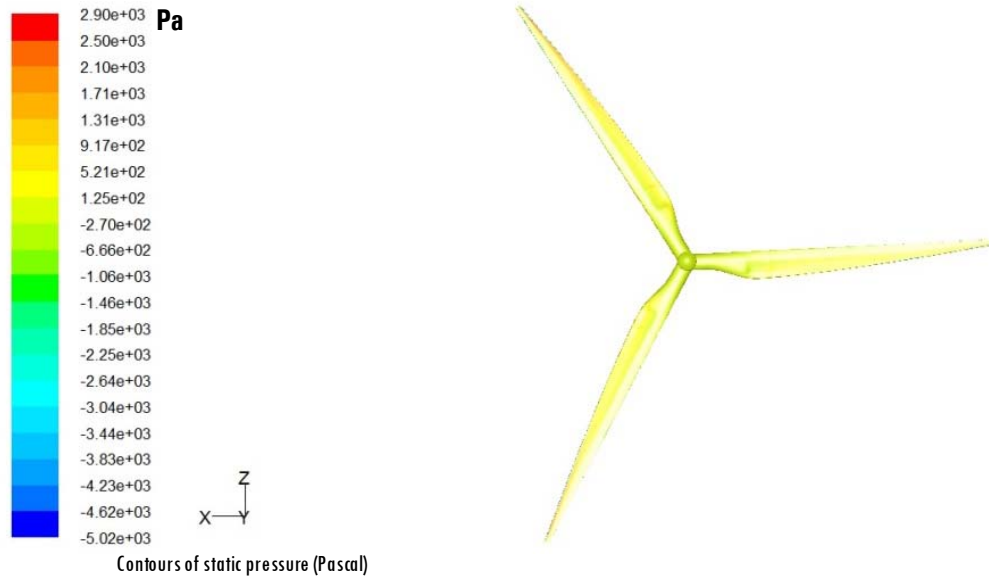


Figure 4.28 Static pressure contour over the three blades viewed from air flow direction.

As shown in the *Figure 4.28* the root section and tip section of the blades facing wind experience static pressure around -270 Pascal to 521 Pascal. When compared to the trailing edges the leading edges experience higher static pressures. The trailing edges of the tip region of blades of HAWT are subjected to a maximum static pressure of around 1310 Pascal.

Figure 4.29 shows the static pressure of the swept area of the HAWT. The static pressure around, the lower half region of swept area is moderately negative around -3 Pa. At the upper half portion of the swept area, the static pressure goes down further and it is around -57 Pa. The region around the tip of the blade which is away from the tower has a high static pressure pocket around 90 Pa.

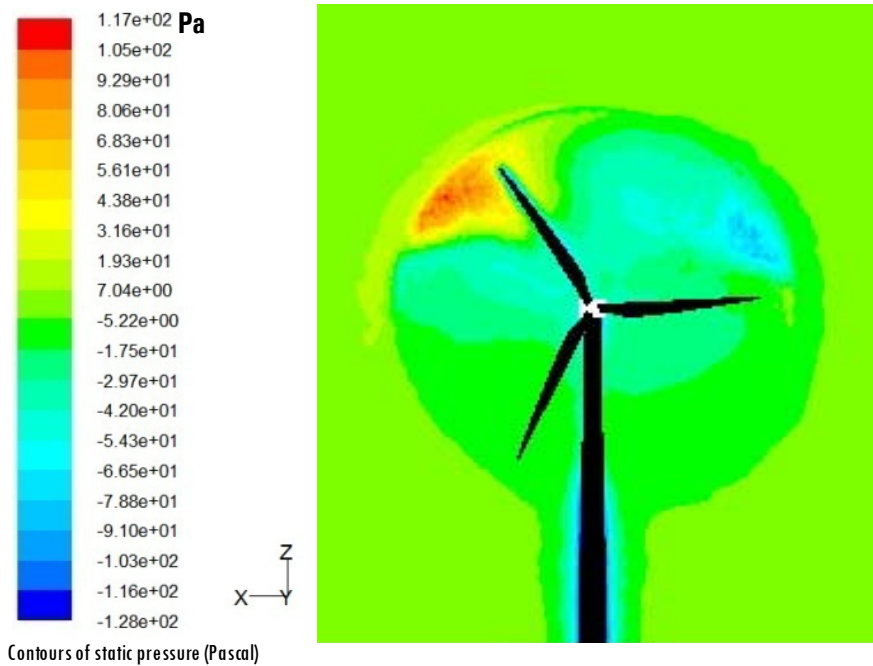


Figure 4.29 Static pressure contour over the entire wind turbine viewed from air flow direction.

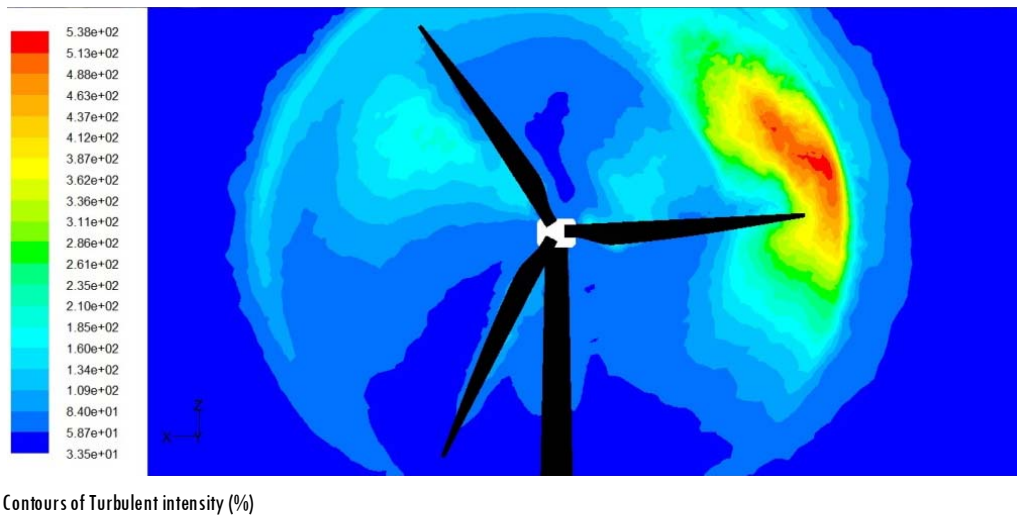


Figure 4.30 Turbulence intensity

Figure 4.30 shows the turbulence intensity contour over the entire wind turbine viewed from air flow direction

The undisturbed wind flowing towards the HAWT was having only 5 % turbulent intensity. The free flowing wind interacts with blades of HAWT and the turbulence intensity rises up to 536 %. The wind in the swept and just around the blade expect in the tip region have non uniform turbulence. The wind and the blade which approaching the tower has lower turbulent intensity. The wind behind the blade which is leaving the tower has an increased turbulence level. The wind zone between the tower and up to half the radius of the blade has growing turbulence level. The zone and the tip of the blade which left the tower have maximum turbulent level.

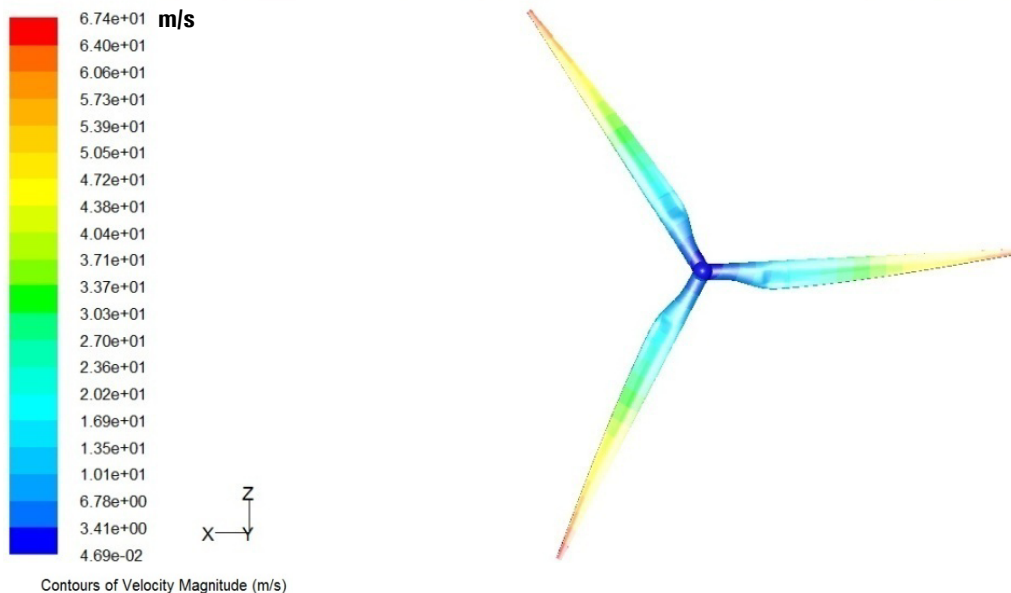


Figure 4.31 Contour velocity magnitude over the entire wind blades viewed from air flow direction.

As shown in the *Figure 4.31* the root section and tip section of the blades facing wind experiences velocities around 3 m/s and 57 m/s respectively. Comparing to the trailing edges the leading edges experience lower velocity magnitude. The trailing edges of the tip region of blades are subjected to

maximum relative wind velocity of 60 m/s compared to the inflow wind velocity of 9 m/s.

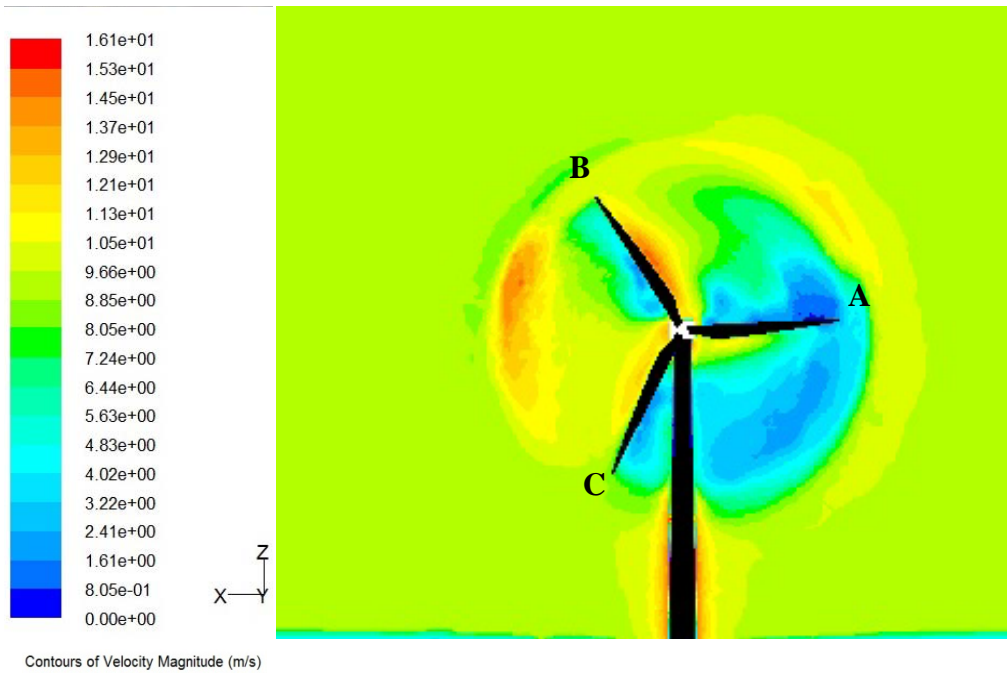


Figure 4.32 Contour velocity magnitude over the entire wind turbine viewed from air flow direction.

The contour velocity magnitude over the entire wind turbine and its surrounding region is depicted in *Figure 4.32*. It is well evident that between the three blades the velocity of air drastically varies. The wind in the region across the leaving blade and tower has low velocity magnitude where as the region between the two blades away and approaching the tower has maximum velocity magnitude. The velocity of air at the tip of the Blade A is very low because of high turbulence (*Figure 4.30*) and results in lower pressure moment generation as shown in *Table 4.6*. Because of more turbulence the viscous moment generation is little above when compared to the other two blades.

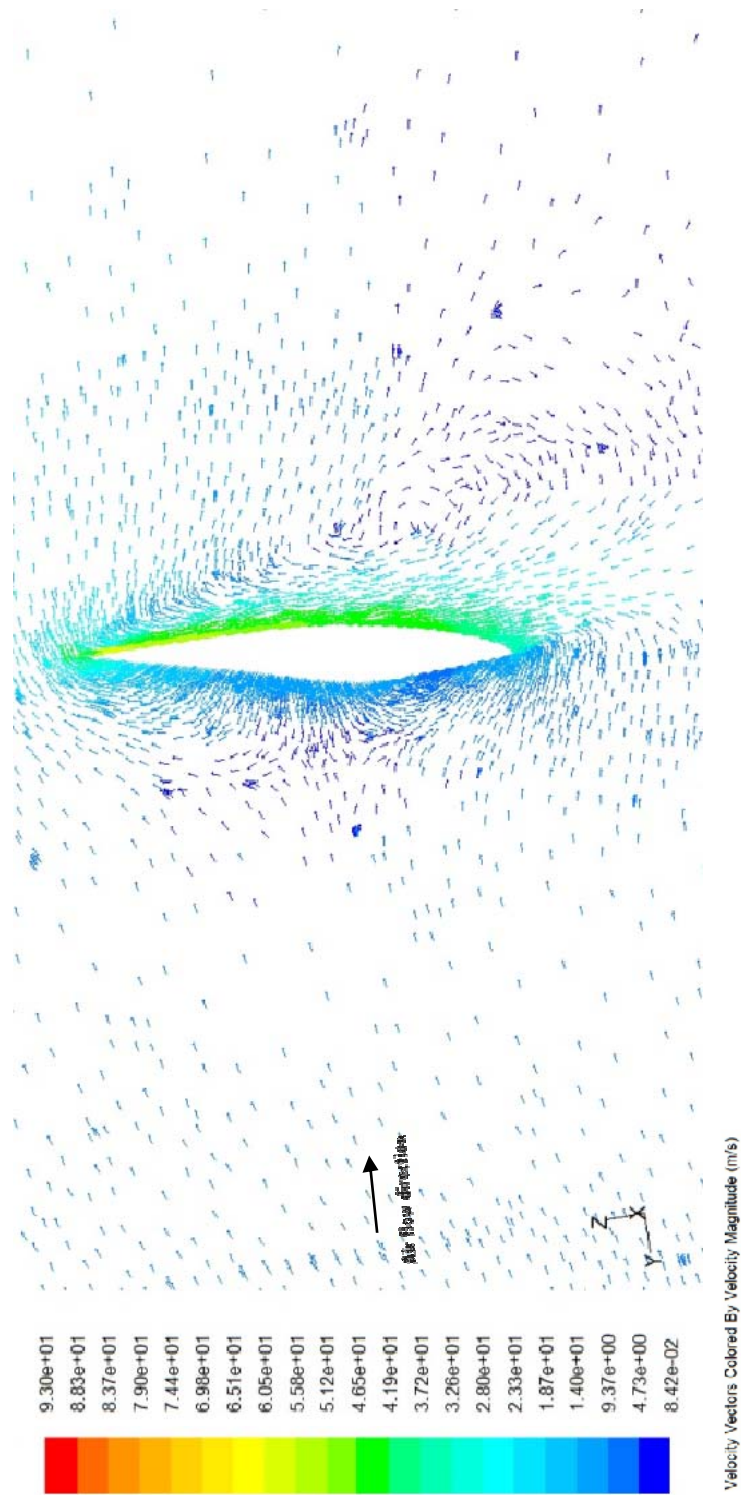


Figure 4.33 Velocity vectors around the middle section of blade.

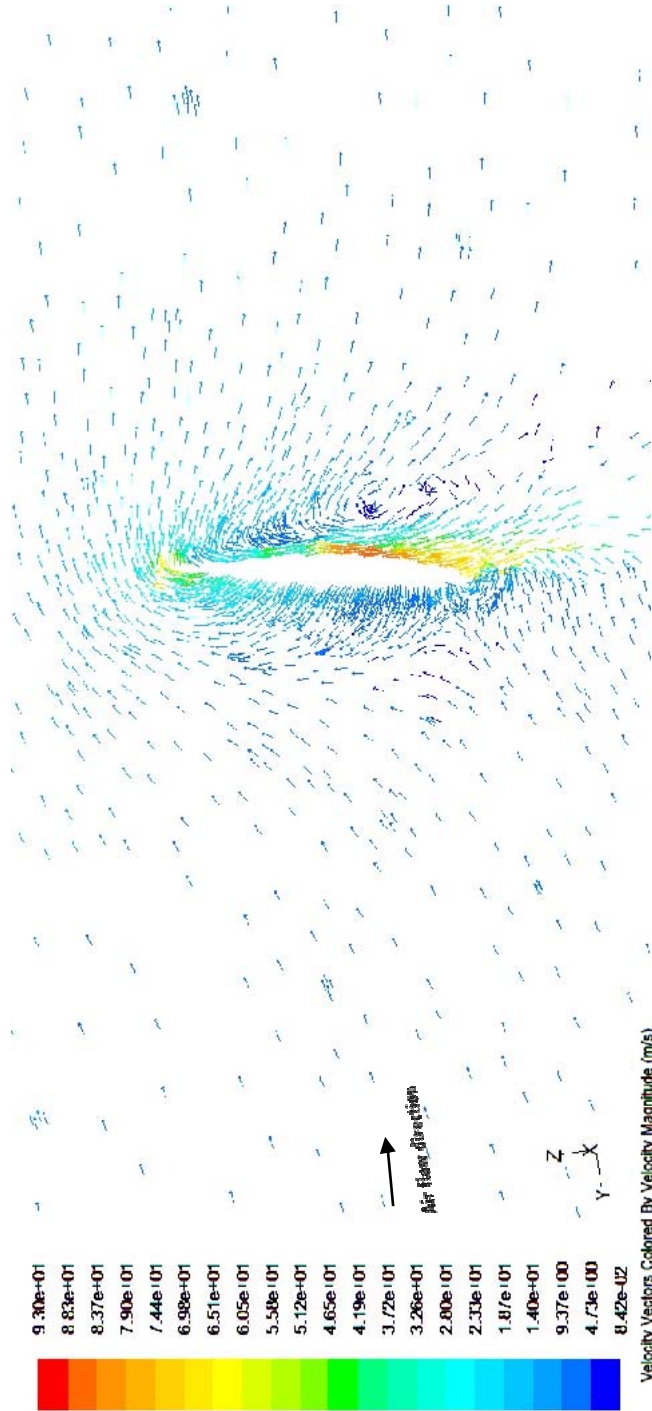


Figure 4.34 Velocity vectors around the tip section of blade.

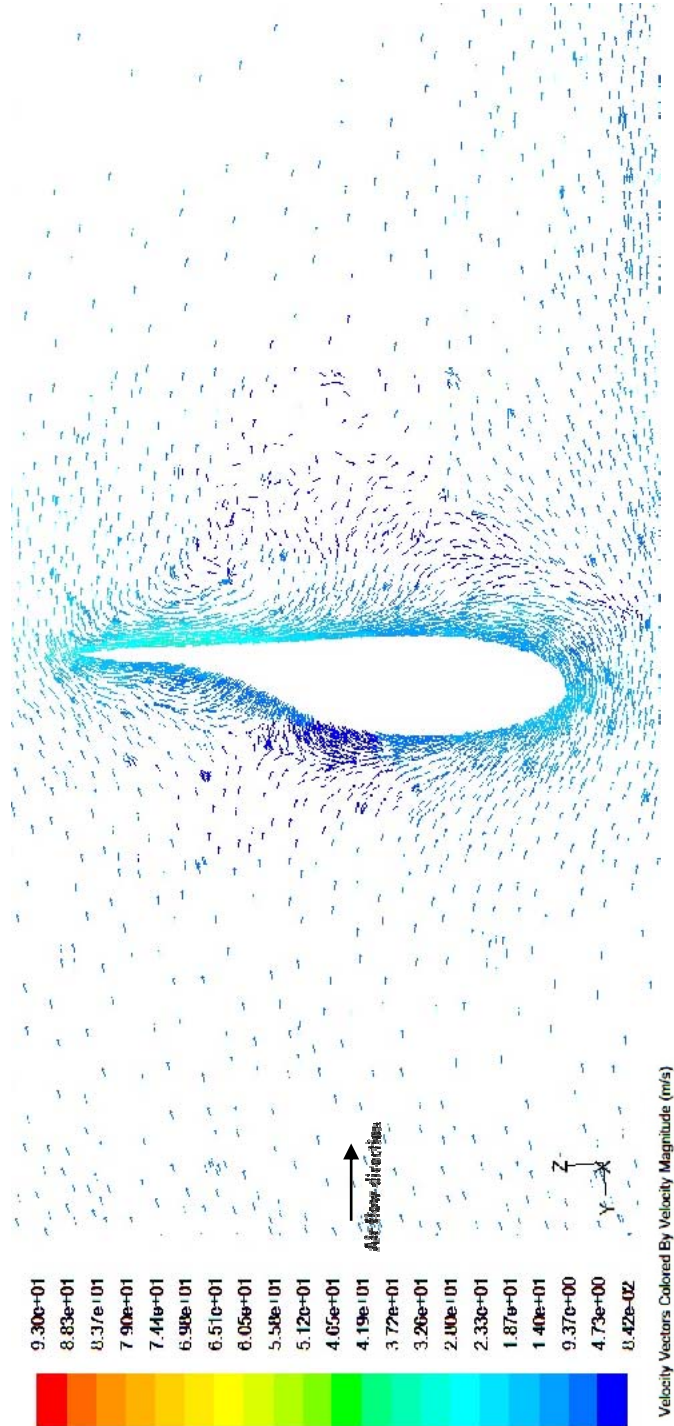


Figure 4.35 Velocity vectors around the root section of blade.

The main objective of the present research is to study the behavior of the airfoil under rotating condition (i.e) multibody condition. *Figure 4.33* vividly describes the wind flow pattern around the airfoil at the middle section of the rotating blade. The approaching wind at 9 m/s hits the middle part of the pressure side or the lower part of the airfoil. Then it is divided into two flows towards the leading and trailing edges. The wind flowing towards the leading edge joins with the free wind and travels over the suction side as layers with high velocity and joins the wind separate while hitting the blade to maintain the continuum. This clearly shows the airfoil performance under multi body dynamic condition.

The *Figure 4.34* shows the wind flow pattern around the airfoil at the tip section of the rotating blade. The approaching undisturbed wind at 9 m/s hits the middle part of the pressure side or the lower part of the airfoil. Then it flows towards the trailing edge. When the wind flows over the 50 % cord length positive over the suction side of the blade it gains a velocity of 70 m/s. At this state also the wind flow is laminar. Finally it joins at the trailing edge with the other portion wind separated while hitting the leading edge.

The wind flow pattern around the airfoil at the root section of the rotating blade is shown in *Figure 4.35*. The approaching wind at 9 m/s hits the middle part of the pressure side or the lower part of the airfoil. Then maximum quantity of the air flows towards the leading edge. The wind flown towards the leading edge joins with the free wind and travels over the suction side as laminar layers with a small gain in velocity and joins the rest of the wind separated while hitting the blade to maintain the continuum.

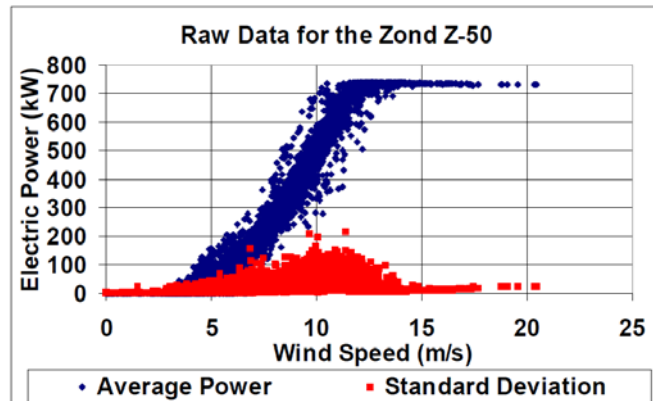


Figure 4.36 Raw data of power measurements
(Source: NREL report)

Figure 4.36 shows scattered data of the power generated by the wind turbine at various wind speed conditions (Vanden, 2000).

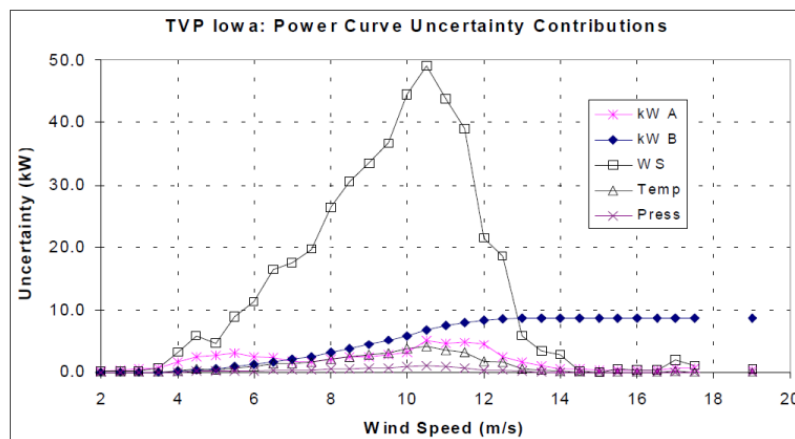


Figure 4.37 Power curve uncertainty contributions
(Source: Vanden, 2000, NREL)

While performing the uncertainty analysis, GEC calculated the contribution that each component of uncertainty adds to the total value in each wind speed bin. The results of this analysis are shown in *Figure 4.37*. Below rated power, the uncertainty in the wind speed measurement is by far the largest contributor to the total value of uncertainty. This could be improved by using an

anemometer with higher accuracy and by having a better understanding of flow distortion between the met tower and the test turbine. The site is very flat and easily met the requirements of the IEC standard without the need for a site calibration. However, site effects still led to a 4 % uncertainty in the wind speed measurement. By comparison, sensor accuracy and calibration contributed 0.5 % and 1.5 % to the wind speed, respectively. Above rated power, the wind speed has relatively little effect on the total uncertainty because the power curve is very flat, thus reducing the sensitivity to uncertainty in wind speed measurement. The uncertainty above rated power is dominated by Category B (sensor accuracy) effects on the electrical power measurement (Vanden, 2000).

Figure 4.36 shows scattered data of the power generated by the wind turbine at various wind speed conditions.

Table 4.5 shows the power generated by the wind turbine at various wind speeds (Vanden, 2000).

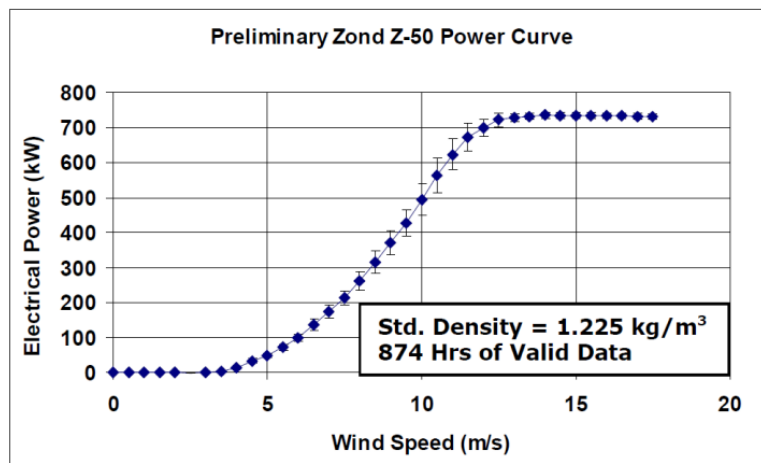


Figure 4.38 Power curve of Zond 50 HAWT
(Source: Vanden, 2000, NREL)

The measured power shown in *Figure 4.38* was adjusted to sea level density and the error was found to be less because the wind mill site was a flat

one. The power for every 0.5 m/s interval raise in wind speed for a range of 0 to 17.5 m/s is plotted. A close analysis shows that up to wind velocity to 3.5 m/s the aerodynamic power captured by the wind turbine is utilised for its own inertia. From 3.5 m/s onwards the power curve has a gentle slope up to 6 m/s and goes up in an accelerated fashion up to the rated wind speed of 12.5 m/s. After that the excess power is let out and the power curve flattens. In variable pitch turbines the blade selected by NREL for their turbine verification program should be positioned at the correct angle of attack for the particular relative wind speed. Since the blade is made up of three airfoils and their combinations pitching angle calculation requires clinical precision (Vanden, 2000).

Table 4.5 Comparison of Power generation

S.NO	Velocity m/s	Experimental Power kW	Numerical Results kW
1	0	0	0
2	3.5	8	233
3	5	50	272
4	7	175	433
5	10	500	561
6	12.5	725	840

The power contrast observed in the *Table 4.5* is due to the fixed inertial losses, gear box efficiency, and generator efficiency (Gary, 1985, Patel, 2007).

Aerodynamic power of the HAWT was calculated by numerical solution as total momentum in the axis of rotation multiplied by the angular velocity. The present research proves the calculation method for the power generated by any of the HAWTs.

Even a small variation in angle drastically affects the performance of the blade; only for a particular angle of attack the blade produces the maximum lift and minimum drag. The angle of attack for each airfoil can be calculated easily. But, for a combination of airfoils of a single blade no universal method has

been found out. The method followed in the present research work is capable of identifying the correct angle of attack. In the model the blade can be pitched for various angles and the corresponding power can be calculated.

The present study proves that as the angle of attack increases the lift keeps on increasing and at a particular angle flow over the airfoil separates leading to stall. In general, a higher angle of attack is to be maintained for lower speeds and vice-versa. This concept was considering simulation of angles of attack of 60° , 65° , 70° , 75° and 80° , with various wind speed limited to the rated wind speed of 12.5 m/s. The angle of attack was measured with reference to wind flow direction (Y-axis). Further analysis carried out by considering angle of attack of 68° , 69° , 70° , and 71° revealed that an angle of attack of 70° gave the maximum power generation for the rated wind speed. The analysis with k- ϵ turbulence model resulted in unrealistic power values which were above the Betz limit.

The numerical results for power shown in *Table 4.5* are found higher than the experimental values obtained under the field conditions. The difference between the two values should account for the inherited losses of a HAWT.

Table 4.6 Moments generated by the three Blades

Zone	Pressure moment N-m	Viscous moment N-m	Total moment N-m
BladeA	59117.6	9939.89	69057.5
BladeB	106908	8758.42	115666
BladeC	127278	8223.6	135501
Total	293303	26921.9	320225

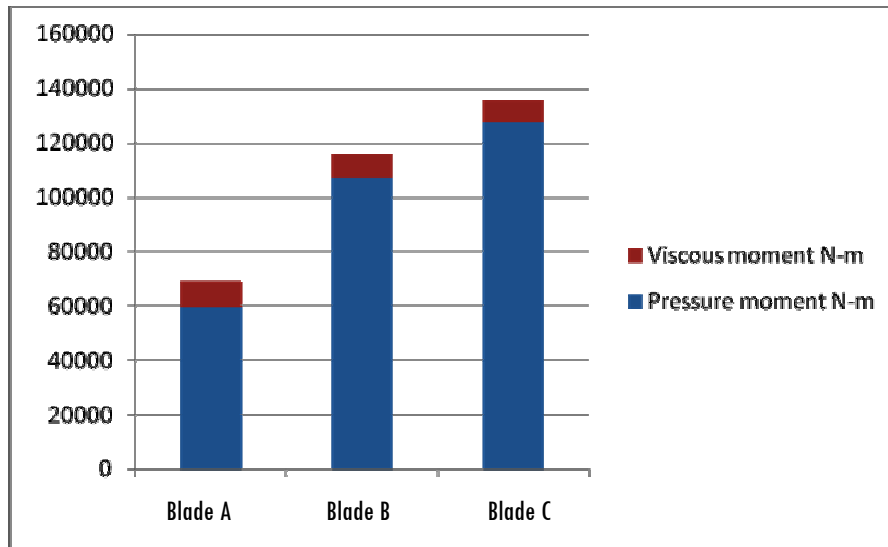


Figure 4.39 Pressure and viscous moments generated by each blade.

Figure 4.39 shows the pressure and viscous moments generated by the three blades..

4.12 Conclusions

From this study following conclusions can be drawn.

- A whole assembly of wind turbine can be modelled to the real size with all the features like complete, cone angle and tilt angle, rotor hub and three blades.
- The complete profile of the blade can also be modelled without losing its geometry which contributes to flow of physics.
- The finite and fine pitch angle can be modelled and performance could be studied. The power generation from an HAWT can be predicted for any pitch angle.
- The wind shear can be simulated for varied ground surface conditions and turbulence intensity levels and their effects on wind turbine performance could be studied.

- Static pressure over the surface of the HAWT structure can be analysed by visualising the static pressure contour.
- Similarly dynamic pressure, absolute pressure and relative velocities can be studied.
- Turbulence levels and relative positions the swept domain of HAWT can be well analysed using CFD.
- The vortices and wake generated could be well predicted over the wake region.
- The resultant momentum generated by each blade at any position of rotation relative to the tower can be well predicted. This is very important in analysing the tower influence and tower shadow affects.
- The pressure load at any point on the surface of the blade can be predicted and this can be used to design aero elasticity effects.
- Interestingly the power generated by similar blades of the HAWT varies with respect to their space position.
- It is found that power generation will be more when the blade is approaching the tower during rotation and the power generation by the same blade will be less when it moves away from the tower. This shows the significance of the CFD based multibody dynamics approach for the analysis of HAWT performance.
- The study proved that as the angle of attack increases the lift keeps on increasing and at a particular angle onwards flow over the airfoil separates leading to stall.

4.13 Necessity for further techniques.

From the present study of validation of performances of the HAWT through numerical solution, it is found that the HAWT is not performing well at lower wind speeds. Hence it is necessary to find a suitable technique so that the HAWT performs well at wind speed lower than the cut in speed. The option available is to modify the blade geometry.

The CFD simulation study revealed that even a small change in angle of attack for a particular wind velocity creates a stall effect leading to lower power generation. Since the wind velocity is not constant in practice, an immediate change of angle of attack even to an extent of 1^0 is not possible. Hence it is needed to find a technique to delay stall for small change in angle of attack.

To have the maximum energy from wind we need to go for maximum swept diameter which leads to the high tip speed ratio. This leads to greater turbulence at the tips of the HAWT. A technique has to be found to avoid the flow joining side wards of the airfoil at the tip of the blade leading to tip turbulence.



EFFECT OF SURFACE ROUGHNESS ON PERFORMANCE OF WIND TURBINE

5.1 Introduction

The development of modern airfoil, for their use in wind turbines was initiated in the year 1980. The requirements for such airfoils differ from standard aviation airfoils, due to the structural reasons and extensive aerodynamic off-design operation conditions. The wind turbine airfoils operate frequently under fully separated flow, whenever stall is used for power regulation at high wind speeds. Even in the case where traditional aviation airfoils are used on wind turbines, their performance needs to be verified in the entire operational range and at suitable Reynolds numbers.

Eventually these traditional aviation airfoils are modified for achieving improved performance by aerodynamic devices, such as vortex generators and gurney flaps. Apart from these two techniques the surface roughness plays a vital role in the flow separation or transition of laminar flow to turbulent flow. Thus there is a need for continuous testing of new airfoil configurations. Modern airfoils are to a large extent developed, based on the numerical calculations and optimization studies. The flow conditions such as separation at high angles of attack, laminar separation bubbles and transition from laminar to turbulent flow are difficult to predict accurately using conventional methods. Hence, testing of airfoils using the present numerical method becomes an

important issue in airfoil design. The present research addresses the effect of surface roughness of HAWT blade and optimizing the roughness value.

5.2 Studies on Roughness

Turbulence has an important influence on the average output power of a wind turbine. The wind dynamics coupled to the turbine dynamic characteristics results in a fairly complicated behavior. Thus the common "static" model of calculating the average power based on the turbine power curve and the average wind speed, may result in increasing errors as pointed out by Rosen and Sheinman (1994).

Sohn (2005) designed a rotor blade for the variable speed operation on the pitch controlled direct drive wind turbine 750 kW KBP-750D. The blade geometry was based on the modified NACA 63 and AE02 series profiles. The cylindrical profile was adopted near the blade root for easy connection with rotor hub and to assure the structural strength on the inner part of the blade. The designed blade showed good aerodynamic performances. The characteristics of aerodynamic design of the rotor blade for the KBP-750D were studied.

A prototype of 750 kW direct-drive wind turbine generator systems, KBP-750D was under development in Korea. For the gearless, direct-drive prototype a synchronous generator with permanent magnets was developed. This upwind 3-blade type machine employed variable speed and pitch control. A general performance requirement of the new airfoil families was to exhibit a maximum lift coefficient. The airfoil families address the needs of stall-regulated, variable-pitch, and variable-rpm wind turbines. The airfoils having greater thickness result in greater blade stiffness and low tower clearance. Airfoils of low thickness result in less drag and were better suited for downwind machines and these were analyzed by Tangler (1995).

The energy generating costs of wind turbines directly depend on the wind turbine output. The output of wind turbine depends upon the characteristics of the turbine blades and their surface roughness. An important operating requirement that relates to wind turbine airfoils was its ability to perform when the smoothness of its surface was degraded by dust. The effect of surface roughness of rotor blades due to accumulated dust on the blade surface of stall-regulated, horizontal axis 300 kW wind turbine was investigated. The effect of operation period of wind turbines on the blade surface roughness intensity was investigated by Khalfullaha and Koliubb (2007) experimentally. Also, the quantity of dust accumulated on the blade leading edge and the effect of changing dust area on blade surface were studied.

Wang *et al.* (2008) used the CFD tool in the scoop model for validating the wind turbine experimental results with and numerically predicted power. The test results were used to validate the CFD modeling. In the wind tunnel test, the pressure and velocity distribution were measured and compared against the CFD predicted results.

Ren and Ou (2009) work on full two-dimensional Navier-Stokes algorithm and the SST $k-\omega$ turbulence model were investigated on incompressible viscous flow past the wind turbine two-dimensional airfoils of the wind turbine under clean and roughness surface conditions. The lift coefficients and the drag coefficients of NACA 63-430 airfoils was computed under different roughness heights, different roughness areas and different roughness locations.

Jun *et al.* (2009) carried out an experimental study on the aerodynamic characteristics of a low-drag high-speed natural laminar flow (NLF) airfoil. The comparison of the measured results with the calculated proved the acceptability

of the airfoil and its aerodynamic characteristics had satisfied the design requirements.

This research by Hussian (2010) had used of Navier Stokes Solver, analyzing on the effect of Reynolds number on the surface roughness parameters. The effect of different parameters on surface roughness was analyzed and presented in this study.

Amirulaei *et al.* (2010) studied the design and selection procedure of airfoil sections for small wind turbine blades. It is found that for blades up to 5 m long, two different airfoils mixed at the outer third of the span will be sufficient and have demonstrated good strength and aerodynamic characteristics. The effects of unsteady parameters, such as, amplitude of oscillation, reduced frequency, and Reynolds number on the aerodynamic performance of the model was investigated. Computational Fluid Dynamics (CFD) was utilized to solve Navier–Stokes (N–S) equations based on the finite volume method (FVM). The resulting instantaneous lift coefficients were compared with analytical data. The simulation results revealed the importance in the aerodynamic performance of the system. Thus, achieving the optimum lift coefficients demands a careful selection of these parameters.

The surface-flow field of finite wings having an aspect of ratio ten were visualized using the smoke wire and surface oil-flow schemes. According to the smoke-streak flow patterns for the low Reynolds number ($Re < 1.5 \times 10^4$), five characteristic flow modes were defined. They were surface flow, separation, separation vortex, separation near the leading-edge and bluff-body wake. Based on the surface oil-flow patterns for the high Reynolds numbers ($Re > 3 \times 10^4$), six characteristic flow modes were defined. They were laminar separation, separation bubble, leading-edge bubble, bubble extension, bubble burst and turbulent boundary layer. The velocity field around the wing was quantified

using the particle image velocimetry (PIV) in this study by Yen and Huang (2010).

5.3 Methodology

The methodology used for the present work is followed similar to that used in Chapter 4. Further the pressure and suction sides of all the three blades are divided into various parts as shown in Table 5.1 and Figures 5.1- 5.6. The surface roughness of uniform grain size of 0.001 m, 0.002 m, 0.003 m and 0.004 m are given as boundary conditions for the surface roughness height.

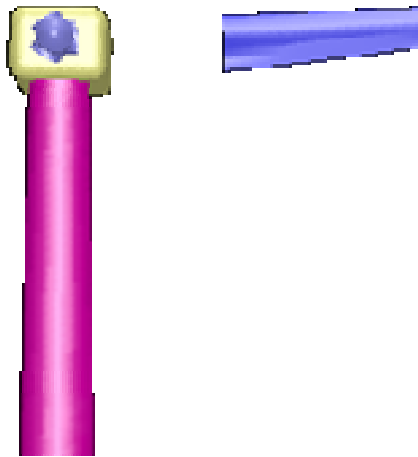


Figure 5.1 Blade A' s pressure side middle part surface.

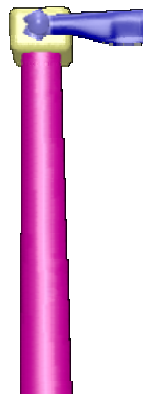


Figure 5.2 Blade A' s pressure side root part surface

The power generated with each roughness height was predicted by the numerical methods.

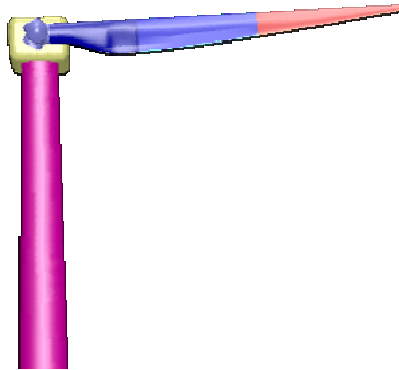


Figure 5.3 Blade A' s pressure side part surface.

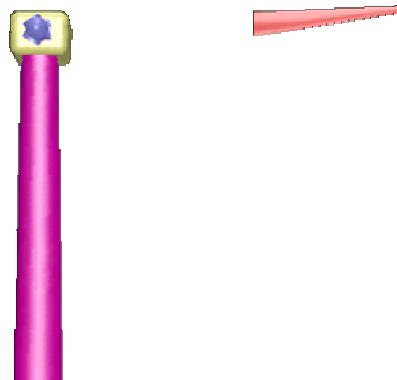


Figure 5.4 Blade A' s pressure side tip part surface

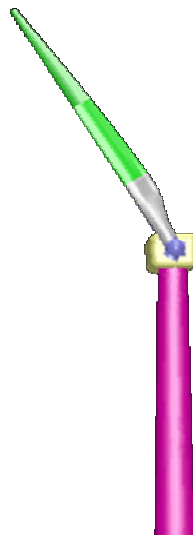


Figure 5.5 Blade B in the HAWT assembly

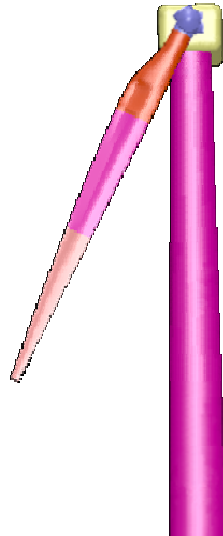


Figure 5.6 Blade C in the HAWT assembly

Table 5.1 Various surface parts of the three blades

Blade-A-psm	Blade A' s pressure side middle part surface as shown in fig 5.1
Blade-A-psr	Blade A' s pressure side root part surface as shown in fig 5.2
Blade-A-pst	Blade A' s pressure side tip part surface as shown in fig 5.3
Blade-A-ssm	Blade A' s suction side middle part surface.
Blade-A-ssr	Blade A' s suction side root part surface.
Blade-A-sst	Blade A' s suction side tip part surface.
Blade-A-tip	Blade A' s tip part surface.
Blade-B-psm	Blade B' s pressure side middle part surface.
Blade-B-psr	Blade B' s pressure side root part surface.
Blade-B-pst	Blade B' s pressure side tip part surface.
Bade-B-ssm	Blade B' s suction side middle part surface.
Blade-B-ssr	Blade B' s suction side root part surface.
Blade-B-sst	Blade B' s suction side tip part surface.
Blade-B-tip	Blade B' s tip part surface.
Blade-C-psm	Blade C' s pressure side middle part surface.
Blade-C-psr	Blade C' s pressure side root part surface.
Blade-C-pst	Blade C' s pressure side tip part surface.
Blade-C-ssm	Blade C' s suction side middle part surface.
Blade-C-ssr	Blade C' s suction side root part surface.
Blade-C-sst	Blade C' s suction side tip part surface.
Blade-C-tip	Blade C' s tip part surface.

Table 5.2 Area of seperated surface zones

Zone Name	Normal Blade Area-1 in m²	Roughness changed blade Area-2 in m²
Blade-A-psm area perpendicular to y axis	21.287355	21.287355
Blade-A-psr area perpendicular to y axis	14.297474	14.297474
blade-A-pst area perpendicular to y axis	20.994221	20.994221
Blade-A-ssm area perpendicular to y axis	21.287355	21.287355
Blade-A-ssr area perpendicular to y axis	14.295125	14.295125
Blade-A-sst area perpendicular to y axis	20.994221	20.994221
Blade-A-tip area perpendicular to y axis	0	0
Blade-B-psm area perpendicular to y axis	30.589773	30.589773
Blade-B-psr area perpendicular to y axis	23.5753	23.5753
Blade-B-pst area perpendicular to y axis	28.969892	28.969892
Blade-B-ssm area perpendicular to y axis	30.589773	30.589773
Blade-B-ssr area perpendicular to y axis	23.536695	23.536695
Blade-B-sst area perpendicular to y axis	28.969892	28.969892
Blade-B-tip area perpendicular to y axis	0	0
Blade-C-psm area perpendicular to y axis	33.293415	33.293415
Blade-C-psr area perpendicular to y axis	22.908458	22.908458
Blade-C-pst area perpendicular to y axis	29.101543	29.101543
Blade-C-ssm area perpendicular to y axis	33.293415	33.293415
Blade-C-ssr area perpendicular to y axis	22.909929	22.909929
Blade-C-sst area perpendicular to y axis	29.101543	29.101543
blade-c-tip area perpendicular to y axis	0	0

5.4 Results & Discussion

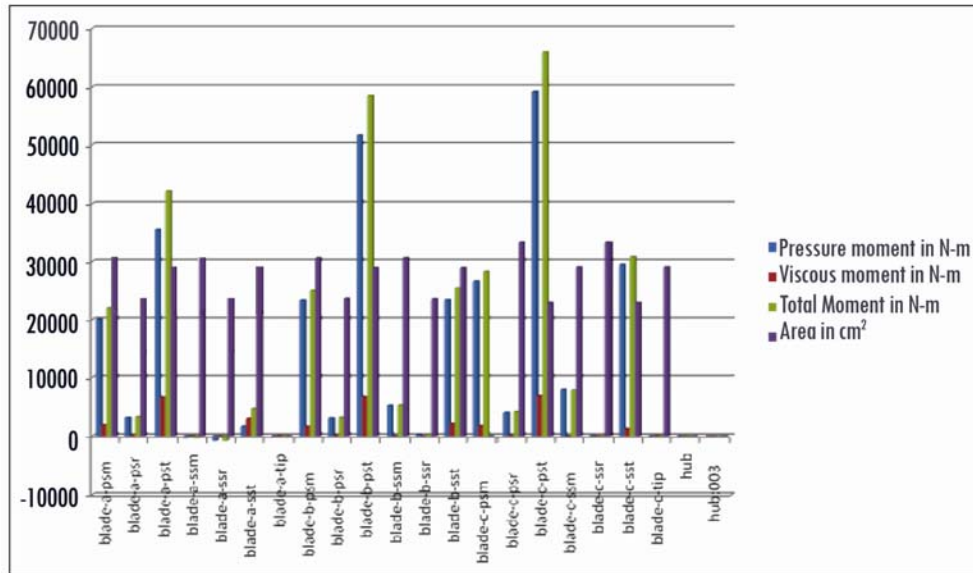


Figure 5.7 Moments generated by various surfaces of blades in Y axis

Moments generated by both pressure force and viscous force on the various surface zones of the three blade surfaces at varying roughness height values are compared in the *Figure 5.7*.

It is evident from the results plotted that the pressure moments predominate the moment generation followed by viscous moments.

The area of each surface zone and its moment generation are also given in the *Figure 5.7* and it is evident the tip surfaces of blades generate more moments.

The moments generated by surface roughness height value 0.001 m are lower than the others and further increase in roughness value above 0.004 m does not give much appreciable enhancement of moment generation.

Table 5.3 Comparison of pressure moment

Pressure moment N-m				
Zone	0.001 m	0.002 m	0.003 m	0.004 m
Blade-a-psm	20099.47	20078.707	20063.384	20022.392
Blade-a-psr	3192.6153	3186.2918	3181.8229	3172.9391
Blade-a-pst	35498.533	35508.893	35518.472	35504.611
Blade-a-ssm	-378.29363	-384.21517	-391.05572	-401.52652
Blade-a-ssr	-837.6766	-835.95132	-834.65209	-833.39552
Blade-a-sst	1554.5337	1629.9518	1663.9275	1730.4054
Blade-a-tip	-11.559069	-11.518546	-11.49931	-11.467596
Blade-b-psm	23309.76	23310.701	23311.812	23294.596
Blade-b-psr	3126.5573	3124.2341	3122.7661	3118.8928
Blade-b-pst	51668.637	51698.32	51700.3122	51714.99
Blade-b-ssm	5175.2098	5172.1092	5168.7102	5163.1549
Blade-b-ssr	244.22124	243.79272	244.15512	243.70222
Blade-b-sst	23383.309	23397.954	23397.727	23388.934
Blade-c-psm	26663.567	26665.299	26666.317	26648.59
Blade-c-psr	4002.5256	3998.8416	3996.073	3989.9098
Blade-c-pst	59089.534	59125.334	59195.6878	59145.067
Blade-c-ssm	7916.2345	7907.897	7899.6684	7888.3606
Blade-c-ssr	63.63058	66.172009	67.802109	69.890831
Blade-c-sst	29558.814	29536.986	29506.71	29464.314
Blade-c-tip	-16.766007	-16.703173	-16.688607	-16.656249

The pressure moments generated by the various parts of the blades of the HAWT are given in *Table 5.3*. The roughness increment of 1mm and the relative pressure moment generated by the various parts are compared in the table.

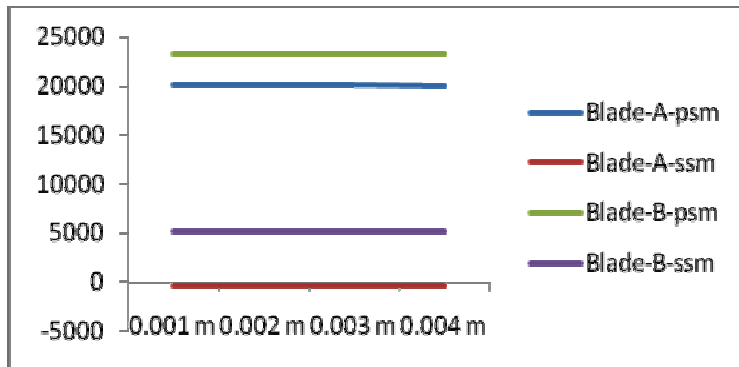


Figure 5.8 Pressure moments generated by Blade-A-psm, Blade-A-ssm and Blade-B-psm, Blade-B-ssm for different surface roughness heights

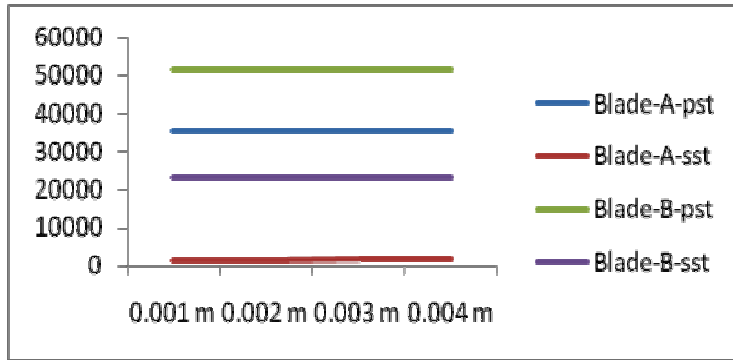


Figure 5.9 Pressure moments generated by Blade-A-pst, Blade-A-sst and Blade-B-pst, Blade-B-sst for different surface roughness heights.

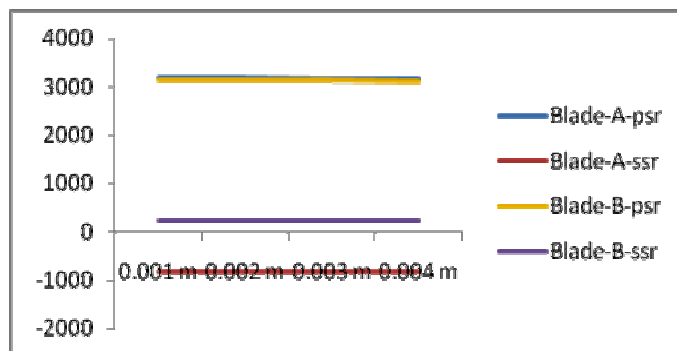


Figure 5.10 Pressure moments generated by Blade-A-psr, Blade-A-ssr and Blade-B-psr, Blade-B-ssr for different surface roughness heights

From *Figures 5.8, 5.9, 5.10* it is evident that there is no variation in the pressure moment generated by the various parts of blade A and B. From this we can conclude that there is no effect of surface roughness in pressure momentum generation.

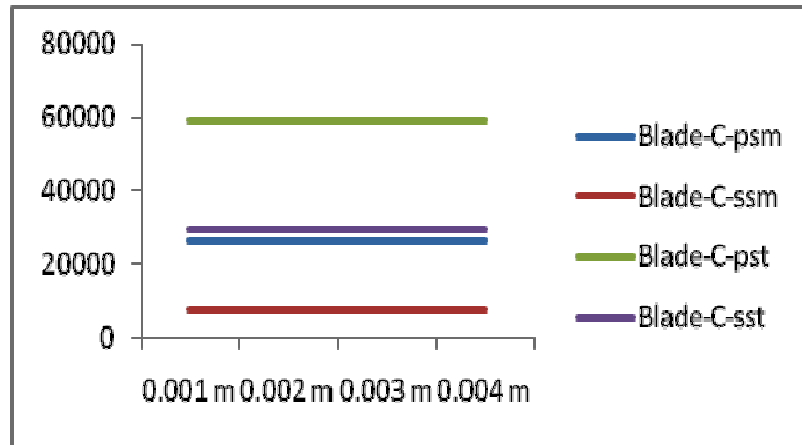


Figure 5.11 Pressure moments generated by Blade-C-psm, Blade-C-ssm and Blade-C-pst, Blade-C-sst for different surface roughness heights.

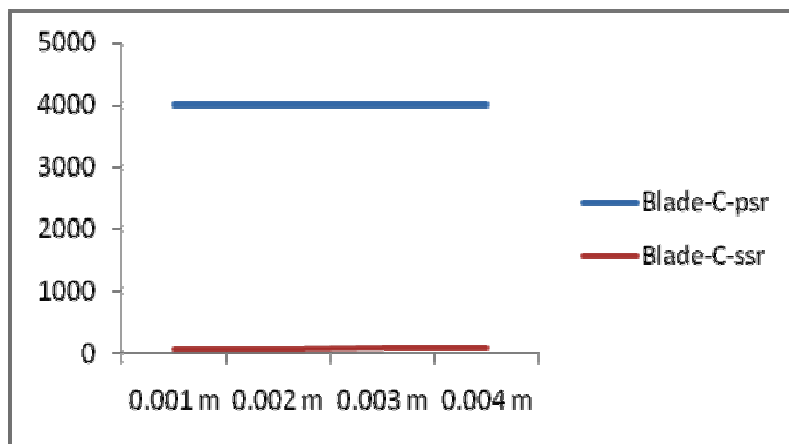


Figure 5.12 Pressure moments generated by Blade-C-psr, and Blade-C-ssr for different surface roughness heights.

From *Figures 5.11 and 5.12* it can be conformed that the blade C also makes no significant difference in pressure moment generation because of

surface roughness variation. From *Figures 5.8 to 5.12* it can also be conformed that the relative position of the blade doesn't make any difference in pressure moment generation because of varied surface roughness values,

Table 5.4 Comparison of viscous moment

Viscous moment N-m				
Zone	0.001 m	0.002 m	0.003 m	0.004 m
Blade-a-psm	1523.0074	1832.0317	2083.9606	2289.5838
Blade-a-psr	103.67431	121.1845	134.62532	145.63139
Blade-a-pst	5650.7557	6636.2116	7391.3514	8021.5268
Blade-a-ssm	7.9970473	7.4886484	7.0368462	5.5343632
Blade-a-ssr	-9.1839355	-11.023847	-12.495021	-13.85187
Blade-a-sst	2630.7362	3026.4079	3317.6546	3544.9307
Blade-a-tip	32.907783	39.239557	39.06198	38.20733
Blade-b-psm	1320.8853	1587.277	1803.9189	1980.0849
Blade-b-psr	81.048615	94.50524	104.78046	113.23336
Blade-b-pst	5566.3291	6731.4081	7852.0212	8454.9456
Blade-b-ssm	18.631976	20.406469	21.711374	21.869245
Blade-b-ssr	-4.877601	-5.8109229	-6.5450504	-7.3260489
Blade-b-sst	1776.3985	2068.1337	2287.9415	2456.3245
Blade-c-psm	1418.0369	1704.1043	1936.4345	2126.6908
Blade-c-psr	109.17285	127.57422	141.67565	153.27725
Blade-c-pst	5699.096	6875.776	7644.9788	8612.5438
Blade-c-ssm	-88.420174	-106.87867	-121.52038	-134.71192
Blade-c-ssr	-7.5516443	-9.2534619	-10.611456	-11.980463
Blade-c-sst	1060.1656	1226.6574	1349.4566	1441.4187
Blade-c-tip	33.104398	38.950361	38.726441	37.955443

The viscous moment generated by the various parts of the three blades of the HAWT are tabulated in *Table 5.4* for roughness values ranging from 0.001 m to 0.004 m at the intervals of 0.001 m.

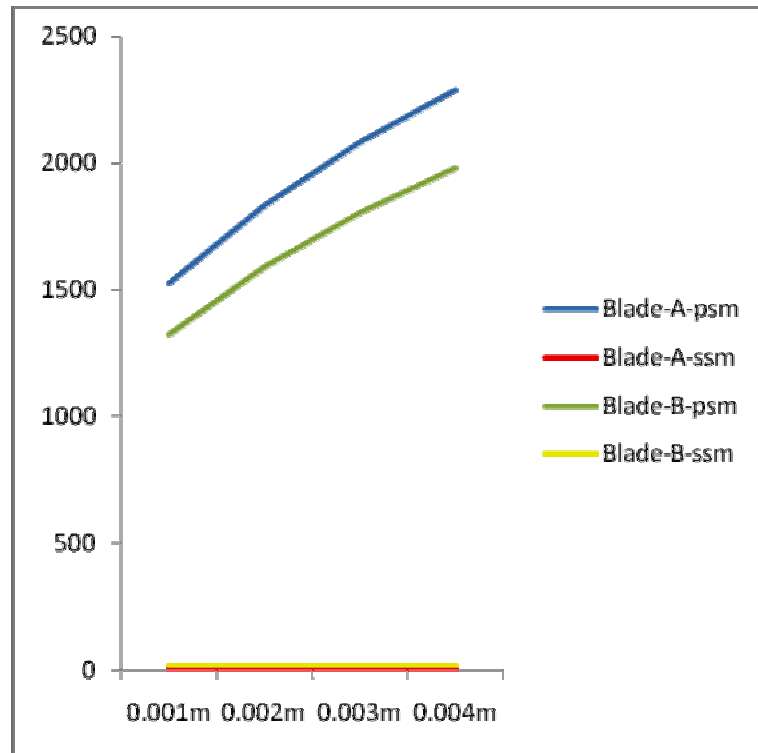


Figure 5.13 Viscous moments generated by Blade-A-psm, Blade-A-ssm and Blade-B-psm, Blade-B-ssm for different surface roughness heights

Figure 5.13 shows the viscous moments generated by the middle part of blade A and B at both suction and pressure side. There is a heavy increase in viscous moment generation with increase in the roughness values on the pressure side middle part of both the blades A and B. Negligible and a very small variation in viscous moment generation in the middle parts of the suction sides of blades A and B.

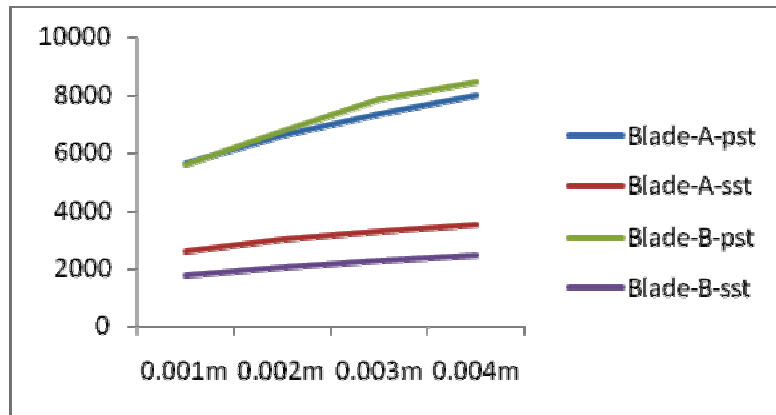


Figure 5.14 Viscous moments generated by Blade-A-pst, Blade-A-sst and Blade-B-pst, Blade-B-sst for different surface roughness heights

Viscous moments generated by the pressure side and the suction side tips of blade A and B are graphically shown with respect to roughness values increase in the *Figure 5.14*. The surface parts of blade B pressure side tip region and blade A pressure side tip region both show considerable increase in viscous moment generation increment with increase in roughness values. Among these two blades B pressure side tip has more increment in viscous moment generation when compared to the others. The suction side tip region surface of the blade A and B both show reasonable increase in viscous moment generation with the increase in surface roughness value.

Again from *Figure 5.15* it can be understood that the pressure side tip region surface of the blades A and B show an increase in viscous moment generation as the roughness value increases. In contrary the suction side tip surface region of blade A and B which are already having negative values of viscous moment generation further decreases. The same concepts applicable to blade C surface as shown in *Figure 5.16*

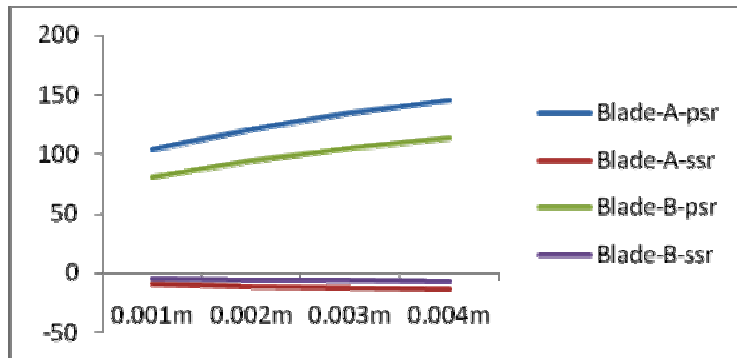


Figure 5.15 Viscous moments generated by Blade-A-psr, Blade-A-ssr and Blade-B-psr, Blade-B-ssr for different surface roughness heights.

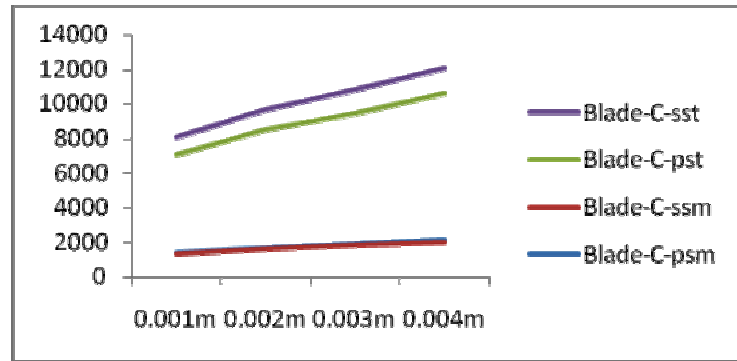


Figure 5.16 Viscous moments generated by Blade-C-sst, Blade-C-pst and Blade-C-ssm, Blade-C-psm for different surface roughness heights.

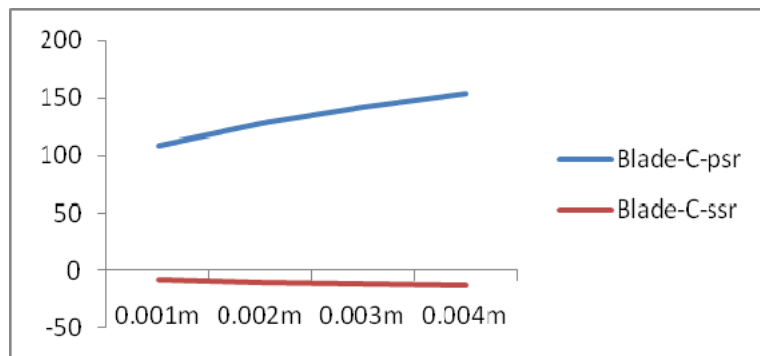


Figure 5.17 Viscous moments generated by Blade-C-psr, and Blade-C-ssr for different surface roughness height

Table 5.5 Comparisons of total moment generated by different rough surfaces.

Total moment N-m				
Zone	0.001 m	0.002 m	0.003 m	0.004 m
Blade-a-psm	21622.478	21910.738	22147.344	22311.976
Blade-a-psr	3296.2896	3307.4763	3316.4482	3318.5705
Blade-a-pst	41149.288	42145.104	42909.823	43526.138
Blade-a-ssm	-370.29658	-376.72652	-384.01888	-395.99216
Blade-a-ssr	-846.86053	-846.97517	-847.14711	-847.24739
Blade-a-sst	4185.2699	4656.3597	4981.5821	5275.3361
Blade-a-tip	21.348714	27.721011	27.56267	26.739734
Blade-b-psm	24630.646	24897.978	25115.731	25274.681
Blade-b-psr	3207.6059	3218.7393	3227.5466	3232.1262
Blade-b-pst	57234.966	58429.728	59000.0212	60169.936
Blade-b-ssm	5193.8418	5192.5156	5190.4216	5185.0242
Blade-b-ssr	239.34364	237.9818	237.61007	236.37617
Blade-b-sst	25159.707	25466.087	25685.669	25845.259
Blade-c-psm	28081.603	28369.403	28602.751	28775.281
Blade-c-psr	4111.6985	4126.4158	4137.7486	4143.1871
Blade-c-pst	64788.63	66001.11	67392.9788	67757.611
Blade-c-ssm	7827.8143	7801.0183	7778.148	7753.6487
Blade-c-ssr	56.078935	56.918547	57.190653	57.910368
Blade-c-sst	30618.98	30763.644	30856.166	30905.733
Blade-c-tip	16.338391	22.247188	22.037834	21.299194

Table 5.5 shows the total moment generated by the various surface parts of the three blades of the HAWT, when they have different roughness values.

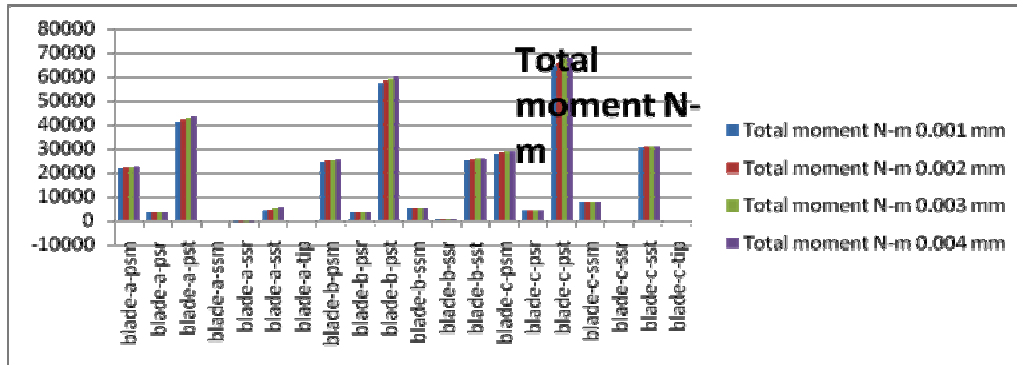


Figure 5.18 Comparison of total moments generated by various surfaces of blades in Y axis.

Figure 5.17 shows that there is no variation in the areas of the blades because of varying the surface roughness values

Figure 5.18 shows the Comparisons of total moments generated by various surfaces of blades in Y axis

5.5 Conclusions

The following conclusions can be arrived from the Chapter 5.

- The surface roughness values over the blade surface of the HAWT can be effectively modeled.
- The effect of surface roughness over the aerodynamic performance of the blades of the HAWT can be numerically simulated and results can be predicted.
 - The capability of numerical methods to solve the NS equation with the bound flow of air over the blades of HAWT with various surface roughness values is established.

- The analyses show that the viscous moments generated by the blades increases with increase in surface roughness values. The velocity of air is not much changed by increase in surface roughness value and thus the pressure moment generated is not appreciably changing.
- Because of the change in surface roughness value, the friction between the blade surface and flowing air increases, thus leading to an increase in the viscous moment.
- The study shows that there is a sharp increase in viscous moment generation with increase in surface roughness value on the pressure sides of turbine blades.
- By optimizing the surface roughness value power generation from an HAWT can be increased by approximately 1.5%.



Chapter-6

EFFECT OF GURNEY FLAPS AND WINGLETS ON THE PERFORMANCE OF THE HAWT

6.1 Introduction

The gurney flap (wicker bill) was a small flat tab projecting from the trailing edge of a wing. Typically it is set at a right angle to the pressure side surface of the airfoil, and projects 1 % to 2 % of the wing chord. This trailing edge device can improve the performance of a simple airfoil to nearly the same level as a complex high-performance design. This device operates by increasing pressure on the pressure side and decreasing pressure on the suction side. And this device is helping the boundary layer flow stay attached all the way to the trailing edge on the suction side of the airfoil. Common applications occur in auto racing, helicopter horizontal stabilizers, and aircraft where high lift is essential, such as banner-towing airplanes (Hossain *et al.*, 2007).

The gurney flap increases the maximum lift coefficient ($C_{L,max}$), decreases the angle of attack for zero lift (α_0), and increases the nose down pitching moment (C_M), which was consistent with an increase in camber of the airfoil. It also typically increases the drag coefficient (C_d), especially at low angles of attack. Although for thick airfoils, a reduction in drag is reported. A net benefit in overall lift to drag ratio is possible if the flap is sized appropriately based on the boundary layer thickness. The gurney flap increases lift by altering the Kutta condition at the trailing edge (Bechert *et al.*, 2000).

The wake behind the flap is a pair of counter-rotating vortices that are alternately shed in a von Karman vortex street. In addition to these span wise vortices shed behind the flap, chord wise vortices shed in front of the flap and become important at high angles of attack. The increased pressure on the lower surface ahead of the flap means the upper surface suction can be reduced while producing the same lift (Mark and Gotz, 2008).

The term "winglet" was previously used to describe an additional lifting surface on an aircraft, e.g., a short section between wheels on fixed undercarriage, but today it refers to a near-vertical extension of the wing tips. The upward angle of the winglet and its inward or outward angle as well as its size and shape are critical for correct performance and were unique in each application (Hantrais and Grenon, 2009).

The wingtip vortex which rotates around from below the wing strikes the cambered surface of the winglet generating a force that angles inward and slightly forward, analogous to a sailboat sailing close hauled. The winglet converts some of the otherwise-wasted energy in the wingtip vortex to an apparent thrust. This small contribution can be worthwhile over the aircraft's lifetime, provided the benefit offsets the cost of installing and maintaining the winglets. Another potential benefit of winglets was that they reduce the strength of wingtip vortices, which trail behind the plane. When other aircrafts pass through these vortices, the turbulent air can cause loss of control, possibly resulting in an accident (Smith *et al.*, 2001).

6.2 Studies on Gurney Flaps and Winglets

Cory *et al.*, (1998) performed two-dimensional numerical investigation to determine the effect of a gurney flap on a NACA 4412 airfoil. A flat plate gurney flap with the order of 1 to 3% of the airfoil chord in length was oriented

perpendicular to the chord line and located on the airfoil windward side at the trailing edge. Gurney flap sizes of 0.5 %, 1.0 %, 1.25 %, 1.5 %, 2.0 %, and 3.0 % of the airfoil chord were studied. Computational results were compared with experimental results. In this the numerical solutions show that some gurney flaps increase the airfoil lift coefficient with only a slight increase in drag coefficient. Gurney flap sizes less than 1.25 % of the main airfoil chord will result in an increased lift coefficient, with very little increase in drag. In fact, at higher lift coefficients the drag is lower than that of the clean airfoil configuration Jany *et al.*, (1998) showed that the use of the gurney flap increases the loading along the entire length of the airfoil, with a large increase in trailing-edge loading.

A wind tunnel experiment was conducted by Ferrer and Munduate (2007) in order to investigate the influence of a gurney flap upon the aerodynamic behavior of an HQ 17 airfoil. The airfoils, with and without the gurney flap, were submitted to two different turbulent flows with the same mean wind velocity but with different turbulence structures. Lift and drag coefficients were calculated in both the cases. The results in this paper show that the gurney flap acts enhancing the lift coefficient of the airfoil and the performance it was almost independent of the scales of the incoming turbulence. The tests were performed at turbulence intensity of 1.8% and 3.5% and at a Reynolds number of 3×10^5 .

Inam *et al.*, (2007) describes the potential of winglets for the reduction of induced drag without increasing the span of the aircraft. For this experiment a model aircraft whose wings profile was NACA 4315 with three different types of winglet (rectangular, triangular and circular) were constructed for experiment. Aerodynamic characteristic of the model aircraft wing with rectangular, triangular and circular winglets and without winglet was studied

using a subsonic wind tunnel. The experimental results show that the drag decreases by 26.4 % from 30.9 % as compared to the aircraft model with and without winglet respectively for the maximum Reynolds number considered in this study. In this study several factors like Airstream velocity, Plan form area, Profile shape of the airfoil, Viscosity of air and Angle of attack (degrees) were considered for winglets lift and drag comparisons. The comparison was done including Coefficient of drag vs. winglet angle, lift to drag ratio Vs Reynolds number and Variation of C_D with winglet angle.

Miniflaps at the trailing edges of airfoils (e.g., gurney flaps or divergent trailing edges) change the Kutta condition and thus produce higher lift. Unfortunately, however, the drag was also increased due to the flow separation downstream of this particular type of trailing edge. Therefore, the trade-off between beneficial and detrimental effects was considered by *Berchart et al.*, (2000). Various aspects of the flow on airfoils with gurney flaps were Fluid flow, Selection of flap size and drag reduction by wake stabilization. It was possible to further reduce the drag of gurney flap by more than 48 % *Berchart et al.*, (2000) with the wake body.

Smith et al., (2001) performed two dimensional steady state Navier-Stokes computations to determine the effect of gurney flap on NACA 4412 and NACA 0011 airfoils. There was good correlation observed between computed and experimental data. Addition of gurney flap increased the lift coefficient significantly with very little drag penalty if proper gurney flap height was selected. Nose down pitching moment also increased with gurney flap height. Flow field structure near the trailing edge shows very good resemblance with Lie beck's hypothesis that provides the possible explanation for the increased aerodynamic performance.

Smith *et al.*, (2001) examined the potential of multi-winglets for the reduction of induced drag without increasing the span of aircraft wings. The results show that certain multi-winglet configurations reduced the wing induced drag and improved L/D by 15-30 % compared to the baseline 0012 wing. A substantial increase in lift curve slope occurs with dihedral spread of winglets set at zero incidences relative to the wing. Dihedral spread also distributes the tip vortex. These observations in the paper supplement previous results on drag reduction due to lift reorientation with twisted winglets set at negative incidence. This study shows that negative incidence and twist of the winglets improves L/D by re-orienting the winglet lift vector forward and thus canceling part of the drag. Flat plate winglets at zero incidences improve the lift curve slope, and produce more lift than an equivalent area of the baseline wing. A combination of optimal dihedral and geometrically twisted winglets would provide enhanced L/D for subsonic wings over a range of Mach numbers.

Brown and Filippone (2003) carried out research on gurney flaps and the related high lift trailing edge devices. Investigation was done for aerofoil performances at Reynolds numbers less than or Equivalent to 10^5 for both with the clean configuration and various gurney flap sizes. The device height is optimized, and a semi-empirical formula linking flap height to free stream speed and aerofoil chord is proposed. This analysis shows that the optimal size of the device was always below the boundary-layer thickness at the trailing edge. At angles below stall, the drag increased to the gurney flap with a height less than the trailing edge boundary-layer which was less than 20 %. For flaps of larger height, or for an aerofoil that was stalled, the drag increment was twice that of the plain aerofoil. The maximum lift to drag ratio occurs when the flap

height is about 90 % of the trailing edge boundary-layer thickness. Therefore, the flap can be applied to a number of low Reynolds number systems, including gliders, micro air vehicles, and wind turbines.

A numerical investigation was performed by Yoo (2000) to determine the effect of the gurney flap on a NACA 23012 airfoil. A Navier-Stokes code, RAMPANT, was used to calculate the flow field about the airfoil. Results were obtained using the standard $k-\omega$ two-equation turbulence model. The numerical solutions showed that the gurney flap increased both lift and drag. These suggested that the gurney flap served to increase the effective camber of the airfoil. The gurney flap provided a significant increase in the lift-to-drag ratio relatively at low angle of attack and for high lift coefficient. It turned out that 0.6 % chord size of flap was the best.

Schatz *et al.*, (2004) described the effect of small micro-tabs (Gurney-flaps) mounted at the lower trailing edge of a HQ17 airfoil using numerical simulation. The focus of attention was mainly placed on the unsteady flow structures in the wake of the gurney flap, as these are responsible for increased induced drag. At a Reynolds number of 10^6 , the flow was investigated by using steady and unsteady simulations which was based on the Reynolds-averaged Navier-Stokes equations (URANS) as well as detached eddy simulations (DES). In order to reduce the occurrence of unsteady flow structures, further simulation was performed using alternative trailing edge shapes. The results from this study show that the unsteadiness can be successfully suppressed and the drag can be reduced substantially using advanced flap concepts. In this paper the relationship between angle of attack and Transition wake was studied.

Gervois and Grenon (2009) described the design and performance analysis of a wing tip device proposed within the M-DAW project by ONERA was presented in this paper. A proto-design process was described and the device was thoroughly assessed (mainly with Reynolds-Averaged Navier-Stokes simulations). This device was a downward pointing winglet designed for a retrofit scenario (the wing could be modified only within the 96 % to 100 % bounds of the span). The downward pointing winglet reaches the M-DAW low speed target (L/D increase by 2 %) when compared to the tip fence of the same span.

Chattot (2005) explained the design and analysis of winglets from an aerodynamic point of view. The effect of a small yaw angle on a wing equipped with such optimal winglets indicates that, even in the presence of viscous effects, they provide weathercock stability.

Bourdin *et al.*, (2006) investigated a novel method of control for ‘morphing’ aircraft. They used as cant angle of 45^0 for the winglet for maximum performances.

Myose *et al.*, (2006) investigated the effect of a gurney flap in a compressor cascade model at low Reynolds number using tuft flow visualization in a water table facility. The results suggested that the gurney flap energizes the flow and delays the stall at large incoming flow angles. This is similar to wind turbine blades cascade with and without gurney flaps.

Watters and Masson (2007) paper presents the recent developments of a new CFD-based method aimed at predicting wind turbine aerodynamics. A comparison was done with results obtained by an actuator disk method (without

tip loss correction), showed that in ranges of lower angles of attack the blade sections exhibits high lift characteristics.

Hossain *et al.*, (2007) describes the influences of two pair of elliptical and circular shaped winglets with the wing of the aircraft model for the reduction of induced drag without increasing the span of the aircraft. The experimental results show that lift curve slope increases by 1 – 6 % with the addition of certain winglet configurations as compared to the aircraft model with and without winglet for the maximum Reynolds number considered in the study.

Cairns *et al.*, (2008) in their paper explored the active control surfaces on wind turbine blades for improved reliability and efficiency. Concept mechanisms were developed, demonstrated, and analyzed with regards to their deployment in current and next generation wind turbine blades.

Dam *et al.*, (2007) describes effect of wind turbine blade tip geometry is numerically analyzed using computational fluid dynamics (CFD). An increase in loadings (particularly the normal force) towards the tip seems to be associated to a span wise flow component present for the swept- back analyzed tip.

Ferrer and Munduate (2007) analyzed the integrated loads were ranked to asses wind turbine tip overall performance. The flow physics around the airfoil was studied three rotating tip shapes and various terms like stagnation pressure, change in Re, AOA and local suction depending on the tip shape.

Dam *et al.*, (2007) focused on the latter aerodynamic devices, their time-dependent effect on sectional lift, drag, and pitching moment, and their

effectiveness in mitigating high frequency loads on the wind turbine. The overall transient behavior of the micro flap is very similar to that of the micro tab, with a slightly faster initial response time and larger lift effectiveness due to the trailing-edge location of the former.

Gaunna & Johansen (2007) described theoretical considerations and computational results on the nature of using winglets on wind turbines. The agreement between FWLL results and CFD results in the case with winglets is not as good as in the case without winglets. Due to this, the predicted increase in C_p is lower for the CFD results.

Maughmer and Bramesfeld (2008) explored the aerodynamics of a gurney-flap-equipped airfoil was explored by means of low-speed wind-tunnel experiment. As the angle of attack is decreased, the influence of a gurney flap extending from the lower surface also decreases as the flap is increasingly immersed in the thickening boundary layer. A gurney flap mounted to the upper surface behaves in the opposite way increasing the negative lift at low angles of attack and having less and less influence as the angle of attack is increased. The gurney flaps result in significantly higher drags for airfoils with extensive runs of laminar flow. This disadvantage disappears as the amount of turbulent boundary-layer flow increases, as is the case with fixed transition near the leading edge of the airfoil. Comparison was done on the aerodynamic characteristics with a 1 % gurney flap located at the trailing edge on the upper and lower surfaces and it suggests the possible location of Flaps.

Thumthae and Chitsomboom (2009) explained the numerical simulation of horizontal axis wind turbines (HAWT) with untwisted blade to determine the optimal angle of attack that produces the highest power output. The numerical

solution was carried out by solving conservation equations in a rotating reference frame wherein the blades and grids were fixed in relation to the rotating frame. Computational results of the 12° pitch angle was in agreement with the field experimental data of the national renewable laboratory (USA), for both inviscid and turbulent conditions. Numerical experiments were then conducted by varying the pitch angles and the wind speeds. The power outputs reach maximum at pitch angles: 4.12° , 5.28° , 6.66° and 8.76° for the wind speeds 7.2 m/s, 8.0 m/s, 9.0 m/s and 10.5 m/s, respectively. The optimal angles of attack were then obtained from the data.

6.3 Methodology

The rotor blades were modeled as briefed in Chapter 4 and their 2 % trailing edges were flapped to 35° inwards to the pressure side as shown in *Figure 6.1*. The rest of the procedure followed is the same as the methodology given in Chapter 4.

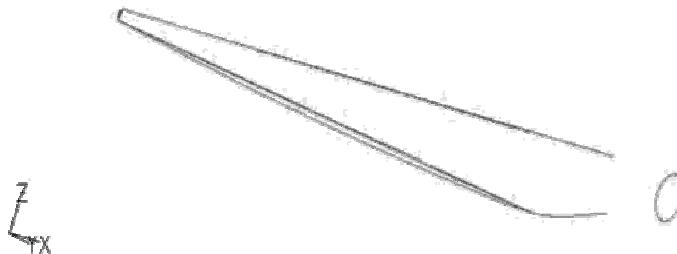


Figure 6.1 Flap at the trailing edge

The blade trailing edge is flapped toward pressure side at an angle of 35° to 2 % of cord length of the airfoil as shown in *Figure 6.7* Cory *et al.*, (1998).

6.4 Results and Discussion

The various moments generated by the three blades with gurney flaps and the results are shown in *Table 6.1*

Table 6.1 Various moments generated by three blades with gurney flaps

Zone name	pressure moment N-m			viscous moment N-m			total moment N-m		
	X	Y	Z	X	Y	Z	X	Y	Z
Blade A	226578	51018	-123216	-105.422	1640.2	260.781	226472	52658	-122954
Blade B	3265.01	48279	184598	-124.04	1559.8	-130.357	3140.97	49839	184467
Blade C	-241204	64447	-142808	244.12	2233.6	171.73	-240959	66681	232875
Net	-11361	16374	-81425	14.662	5433.6	302.16	-11346.	169178	-81123

Power generated 443.25 kW6.1

Table 6.2 Various moments generated by three blades without gurney flaps

zone name	pressure moment N-m			viscous moment N-m			total moment N-m		
	X	Y	Z	X	Y	Z	X	Y	Z
Blade A	-324896.5	62489.9	-178696.3	263.12856	1619.77	125.14449	-324633.38	64109.7	-178571
Blade B	3625.0335	10285.3	157252.39	-153.159	1906.56	1.3196751	3471.8745	12191.8	157253
Blade C	234494.03	23070.5	-140078.8	-4.03433	1790.85	276.37126	234490	24861.4	-139802
Hub	16.01613	5.59581	-53.94856	0.0373684	0.15399	-0.494394	16.053498	5.7498	-54
Net	-86764.25	95849.8	-161575.2	105.99097	5317.36	402.26378	-86658.258	101167	-161172

Power generated 265 kW6.2

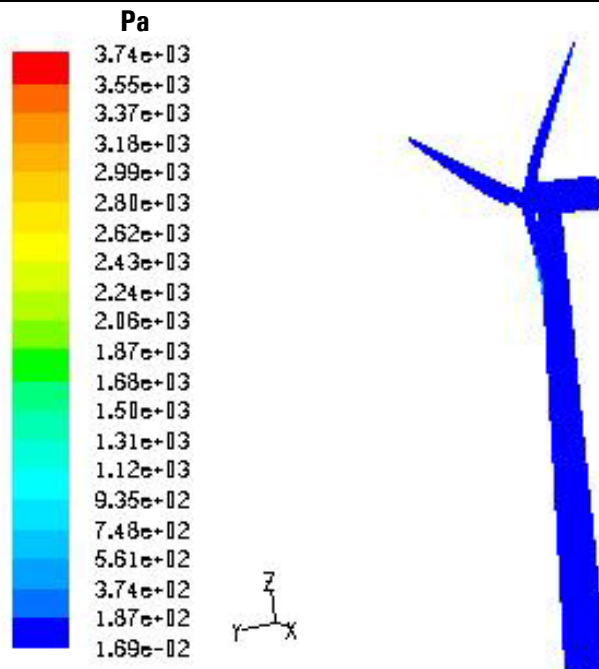


Figure 6.2 Contours of static pressure

Figure 6.2 shows the contours of static pressure over the entire model surfaces.

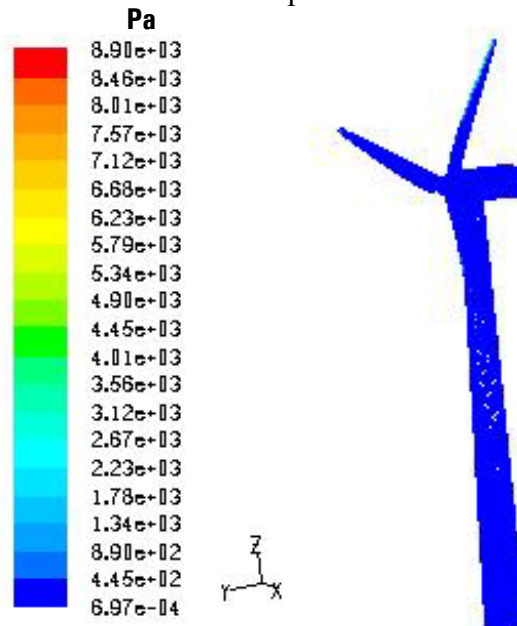


Figure 6.3 Contours dynamic pressures

Figure 6.3 depicts the dynamic pressures over the entire model. The tip region has relatively high dynamic pressure when compared to the other regions of model.

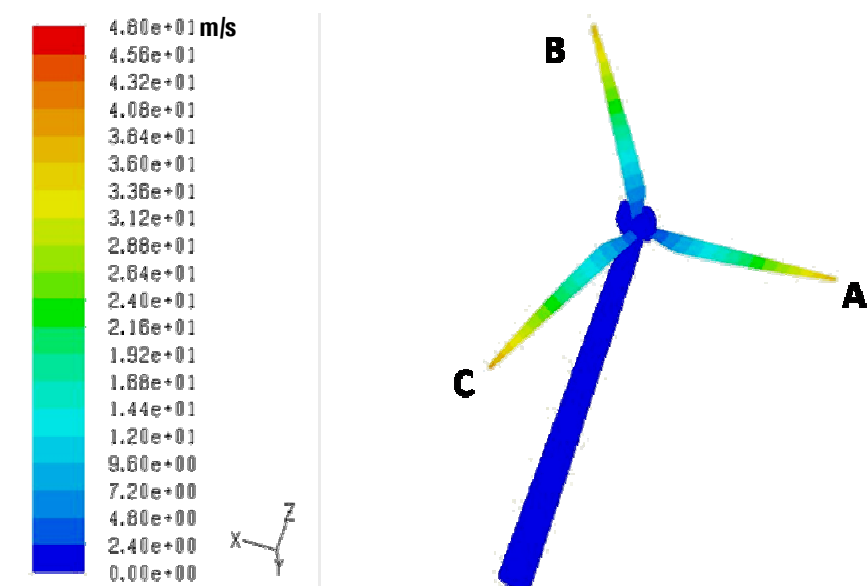


Figure 6.4 Contours of velocity magnitude over the three blades with gurney flaps.

Figure 6.4 shows the contours of velocity magnitude wherein it is clear that the tip has maximum velocity of 45 m/s.

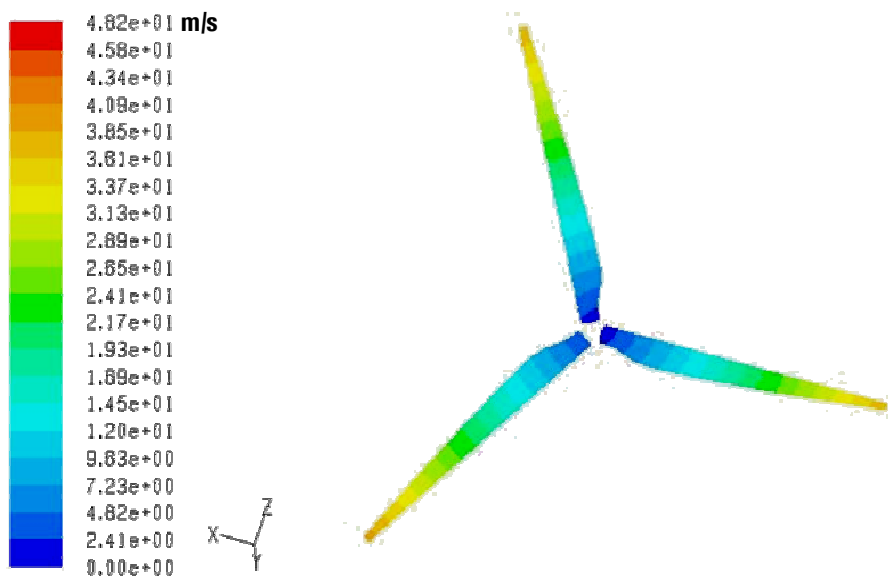


Figure 6.5 Velocity vectors colored by velocity magnitude (without tower)

Figure 6.5 shows the velocity vectors of the blade surfaces and it is well seen that the centre parts of all three blades have lower velocity compared to tip regions which have higher velocity.

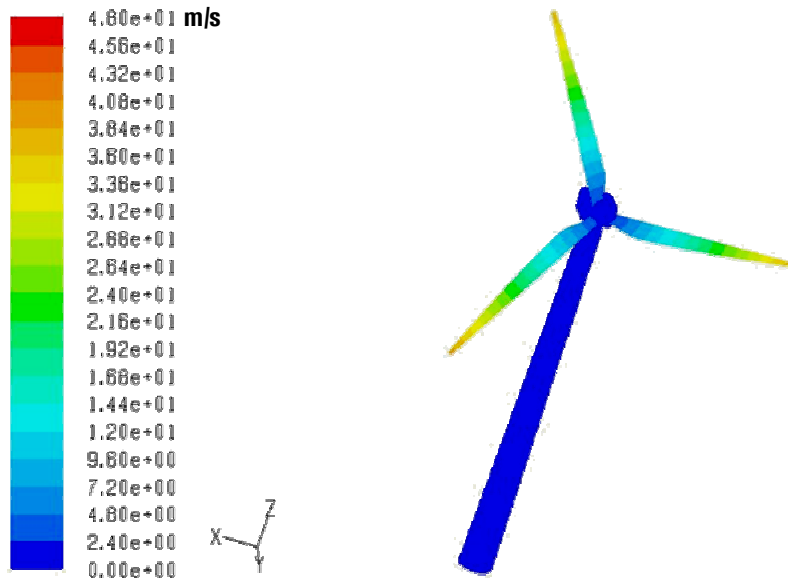


Figure 6.6 Contours of velocity magnitude

Figure 6.6 shows the contours of velocity magnitude over the entire model. Velocity at tip is high because of rotation of blades.

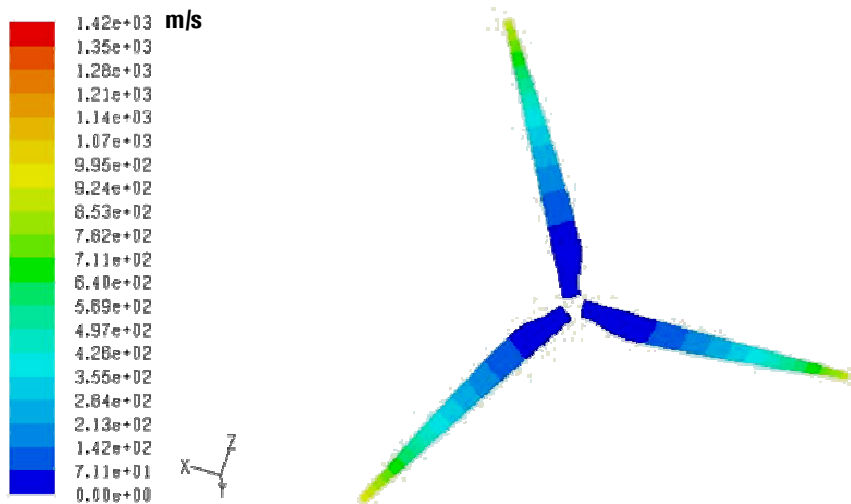


Figure 6.7 Velocity vectors colored by dynamic pressure

Figure 6.7 shows the velocity vectors colored by dynamic pressure among the three blades.

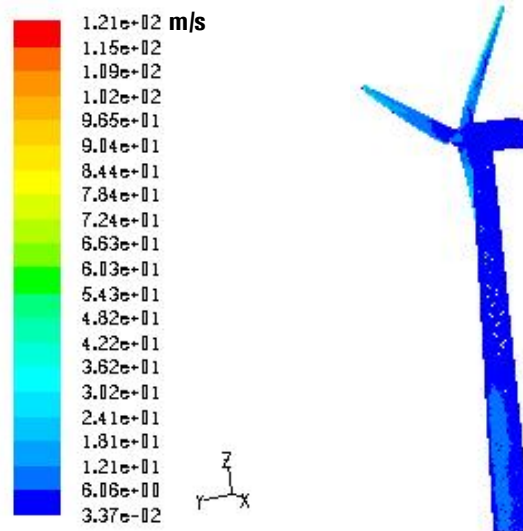


Figure 6.8 Velocity vectors colored by velocity magnitude (with tower)

Figure 6.8 shows the velocity vectors colored by velocity magnitude for the flapped blades.



Figure 6.9 Blade with winglet at the tip

Winglets are introduced at the top of the blade for avoiding the turbulence at the top region when it is rotation at high relative velocities. For avoiding tip region turbulence at tips when the rotating at high relative velocities the tips are introduced with winglets as shown in *Figure 6.9*. Further analysis is same as that followed in Chapter 4 except that the wing length is increased by one meter with S817 airfoil of same dimensions at tip and bent by 30° for a length of 0.5 m in counter clockwise direction (Gervois and Grenon, 2009).

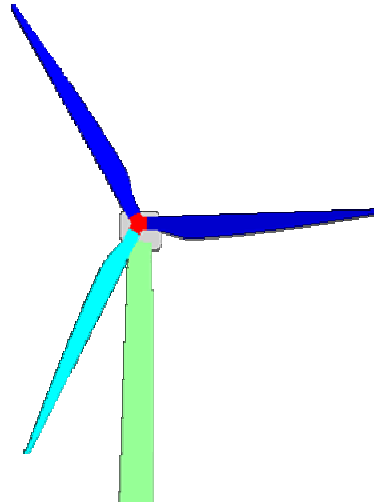


Figure 6.10 Blades with winglet at the tips on HAWT

Figure 6.10 shows the complete assembly of HAWT with winglets at the tips of each blades. The blades are rotating anti clockwise direction. The winglets are kept at tips of the blades pointing in the clockwise direction.

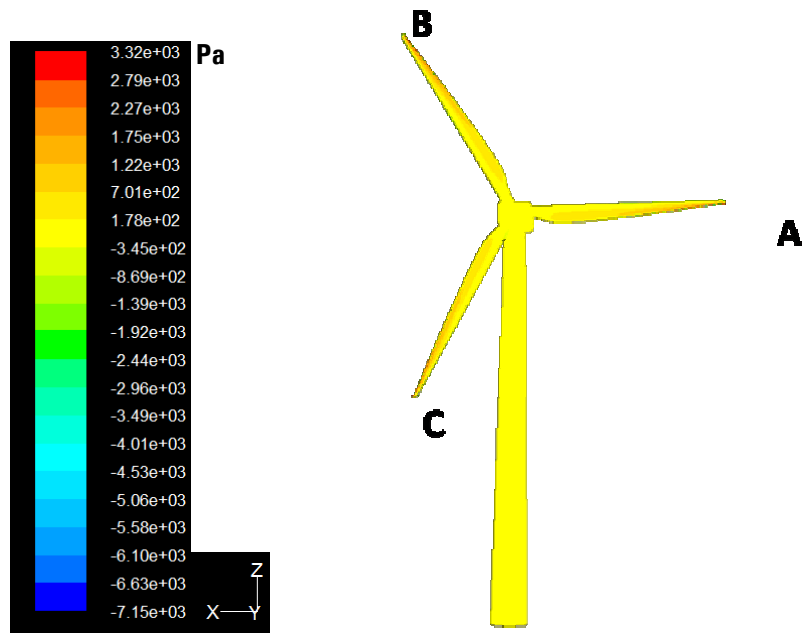


Figure 6.11 Static pressure contour over entire assembly of HAWT with winglets.

Static pressure contour over entire assembly of winglet introduced HAWT is shown in *Figure 6.11*. The tips of the blades have maximum static pressure compared to other areas.

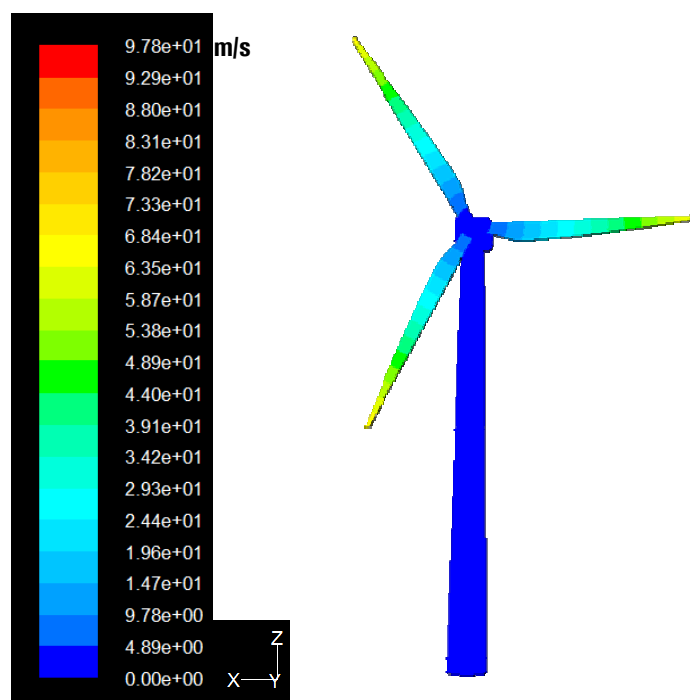


Figure 6.12 Velocity magnitude contour over entire assembly

The velocity magnitude contour over entire assembly of winglet introduced in HAWT is shown in *Figure 6.12*. As in the case of conventional HAWT the winglet introduced HAWT shows higher relative velocities at tips.

The study focused on evaluating the advantages of gurney flap geometry for the blade trailing edge and the complex mechanism of the winglet was investigated.

6.4.1 Effect of gurney flap

The introduction of gurney flap is focused to increase the aerodynamic power generation to 450 kW for 3 m/s wind speed in contrast to the existing generation of 233 kW at 3.5 m/s wind speed condition. Even though all blades are similar in size the moments generated by them differs with respect to their respective space positions. A broad description of the flow field past the rotating blade of a HAWT was given by post processing CFD data. Diagrams and plots of velocity, pressure, vortices, were presented which are suitable for understanding the physical problem. The flow field past the rotating blade of a wind turbine and the rotational effects on its boundary layer were investigated.

Table 6.3 Moments generated by three blades without winglets on Y axis

Zone	Pressure moment N-m	Viscous moment N-m	Total moment N-m
Blade A	215700	353.745	216054
Blade B	246483	320.828	246804
Blade C	273427	322.479	273749
Total	735610.2	997.0519	736607.3

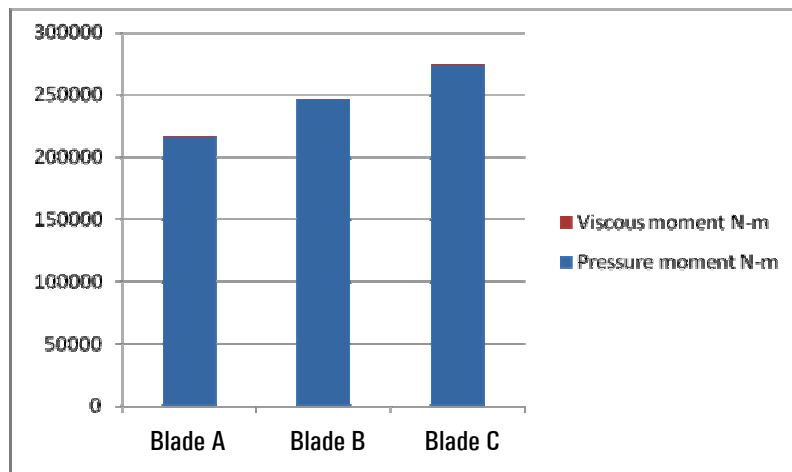


Figure 6.13 Moments generated on Y axis by three blades without winglets.

The blades of the HAWT with winglets are not generating uniform moments as the case of normal HAWT. The Blade 1 which generates lower pressure moment has small amount of higher viscous moment compared to the other two blades.

6.4.2 Effect of winglets.

Table 6.4 Moments generated by three blades with winglets on Y axis

Zone	Pressure moment N-m	Viscous moment N-m	Total moment N-m
Blade A	305583	282.609	305866
Blade B	189513	438.495	189952
BladeC	245269	345.064	245614
Total	740365.2	1066.168	741431.4

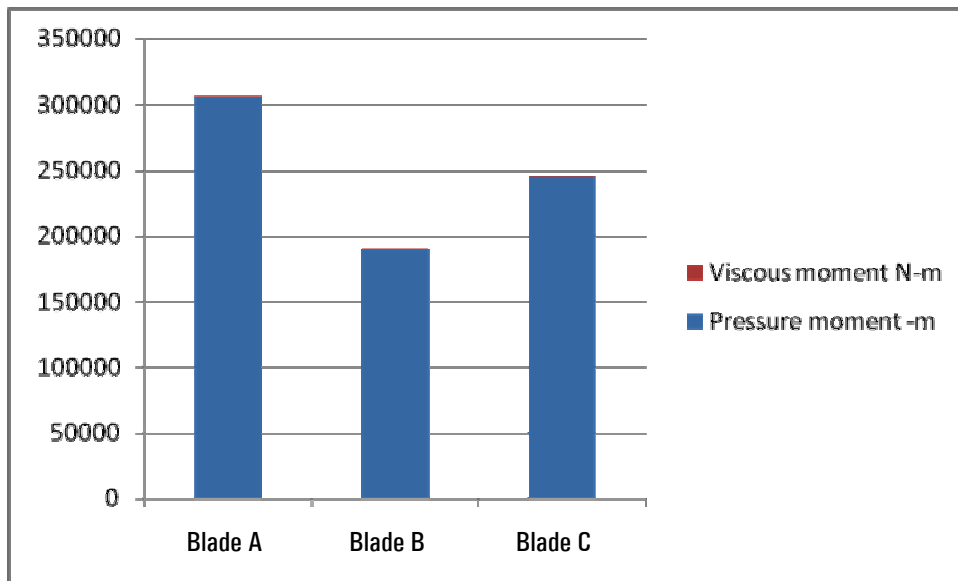


Figure 6.14 Moments generated on Y axis by three blades with winglet

Figure 6.14 shows the moments generated by the blades without winglets

Tables 6.3 and 6.4 show the pressure and viscous moments generated by the three blades without and with winglets respectively. There is substantial increase in the total moment generated by the HAWT with winglets.

6.5 Conclusions

From this Chapter 6 the following conclusions are arrived.

- A model of HAWT with flapped wings and winglets at the end of the blades can be effectively modeled for numerical simulation and analysis.
- The gurney flaps of the blades in the HAWT effectively changes the aerodynamic performances.
- At wind speeds lower than the cut in speed the gurney flapped blade of the HAWT generates excess moments.
- The introduction of gurney flaps increases the power generation from 233 kW to 450 kW for the wind speed range 3 m/s.
- The introduction of the winglets at the tip of the blades rotating at high tip speed ratio can be effectively modeled and analyzed.
- The total momentum generated by the HAWT was found to increase considerably by the introduction of winglets.



EFFECT OF VORTEX GENERATORS ON THE PERFORMANCE OF HAWT

7.1 Introduction

The wind turbine is intended for transformation of wind energy into electrical or mechanical energy and can be used in a wide range of wind velocities including storm winds. The vortex generator is an aerodynamic surface consisting of a small vane or bump that creates a vortex. The vortex generators can be found on many devices, but the term is most often used in aircraft design.

The vortex generators delay flow separation and aerodynamic stalling; they improve the effectiveness of control surfaces for swept-wing transonic designs; they alleviate potential shock-stall. The vortex generators are likely to be found on the external surfaces of vehicles where flow separation is a potential problem because vortex generators delay flow separation. On aircraft they are installed on the front third of a wing in order to maintain steady airflow over the control surfaces at the rear of the wing.

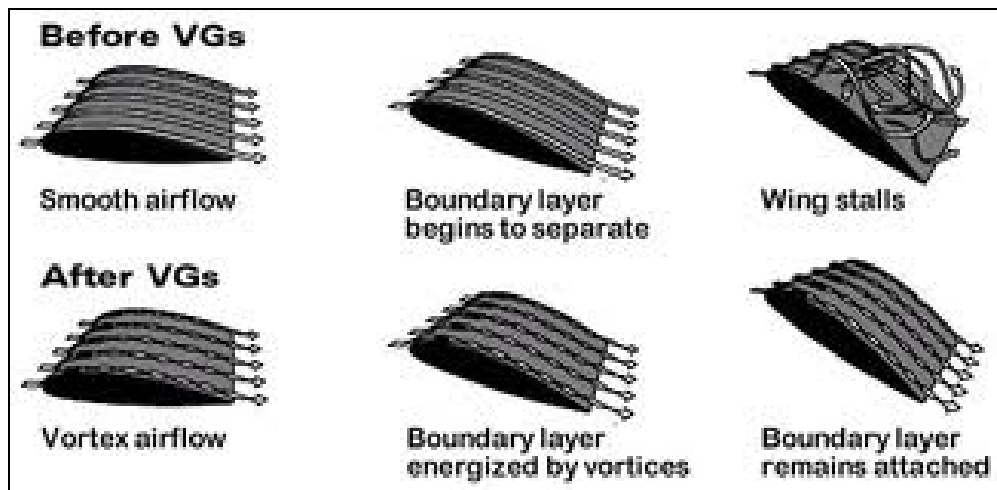


Figure 7.1 Comparison of airfoil with & without vortex generators.

(Source: aerospaceweb.org)

They are typically rectangular or triangular, about 80 % as tall as the boundary layer, and run in span wise lines near the thickest part of the wing. Vortex generators are positioned in such a way that they have an angle of attack with respect to the local airflow. The vortex generator creates a tip vortex which draws energetic, rapidly-moving air from outside the slow-moving boundary layer into contact with the aircraft skin. The boundary layer normally thickens as it moves along the aircraft surface, reducing the effectiveness of trailing-edge control surfaces; vortex generators can be used to remedy this problem, among others, by "re-energizing the boundary layer".

7.2 Problem Definition

The design of an optimal wind turbine is complex because of the many intertwined parameters such as blade profile, blade taper, tip loss, variable wind speed, rotation speed, as well as angle of attack.

The purpose of the present research is to have a better wind harnessing for the medium speed turbine with the proposed blade configuration.

The present research work focuses on obtaining smooth flow on the upper surface of the HAWT blade to reduce the turbulence effect. Maximum lift and power generation is obtained by introducing vortex generators over the blades.

The flow pass on the wind turbine blade is much more complicated than that of an aero-plane wing because of the changing angles of attack along the span, resulting in stall as the hub is approached; in addition, there is centrifugal force acting along the blade due to the rotation.

These complications proved the motivation to investigate the wind turbine blade for full utilization of the blade area to produce lift at low drag while providing a good starting ability and to generate power even at low speed conditions.

7.3 Studies on Vortex Generators

The linearized sheet motion was analyzed under conditions where the unforced sheet (in the absence of the line vortex) is stationary. The vortex passage above the sheet excites a resonance mode of motion, where the sheet oscillates at its least stable Eigen mode. The work describes the essential mechanism by which the sound is generated as a turbulent eddy was convected in a mean flow past a thin elastic airfoil. The vortex method had been extended to account for blade flexibility. The code had been validated previously under the assumption of rigid blades. The aerodynamics method distributes the flow vortices on rigid helicoidal surfaces defined uniquely by the flow parameters (tip speed ratio and average power extracted by the rotor) and the blade geometry (maximum radius and root lengths). The high twist of the wind turbine blades is responsible for induced velocities in the plane of the rotor as well as out of plane (Chung et al., 2005).

Rosen and Sheinman (1994) extended the vortex method to account for blade flexibility. The aerodynamics method distributes the flow vortices on rigid helicoidal surface defines the uniquely by the flow parameters (tip speed ratio and average power extracted by the rotor) and the blade geometry (maximum radius and root length). The high twist of the wind turbine blades was responsible for induced velocities in the plane of the root as well as out of panel.

The aerodynamic performance prediction of a unique 30 kW counter-rotating wind turbine system was investigated by Howell *et al.*, (2010) by using the quasi-steady strip theory. The near wake behavior of the auxiliary rotor that was located upwind of the main rotor was taken into consideration in the performance analysis of the turbine system.

An analysis of the evolution of turbulence characteristics in wind-turbine wakes has been carried out by Tangler (1995). Based on the experimental results and numerical results obtained with a CFD code, complemented with some theoretical considerations, simple analytical expressions are proposed for the estimation of the turbulent kinetic energy.

Wang *et al.*, (2008) carried out a systematic study on the development of a small domestic wind turbine for built up areas. As an outcome of this study, a small wind turbine with scoop was designed, tested and optimized using the methodology combining the theoretical, physical and computational (CFD) methods. The whole study focused only on the aerodynamic aspects of the wind turbine and the criteria for assessment was only on its power output.

A prototype of 750 kW direct-drive synchronous wind turbine generator systems with permanent magnets has been developed by Whales *et al.* (2000). The upwind 3-blade type machine employs variable speed and pitch control.

The operating ranges of wind and rotor speed are 3 to 25 m/s and 9 to 25 rpm, respectively. The tip speed ratio of rotor blade is 7.5 designed for a power coefficient 0.47. The blade pitch and torque are controlled with the predefined torque-speed curve according to the conditions of wind and public electric grid.

Experimental and numerical investigations were carried out by Rhoads *et al.*, (2000) for flow fields of a small wind turbine with a flanged diffuser. To elucidate the flow mechanism, mean velocity profiles behind a wind turbine were measured using a hot-wire anemometer. The experimental and numerical results give useful information about the flow mechanism behind a wind turbine with a flanged diffuser. In particular, a considerable difference was seen in the destruction process of the tip vortex between the bare wind turbine and the wind turbine with a flanged diffuser.

Rodrigo *et al.*, (2007) modeled the flow field inside bi-dimensional clear-cuts oriented perpendicular to the flow direction in a wind tunnel making use of foam-forest models and PIV measurements. The technical feasibility of wind turbine sitting in forest clear-cuts was studied according to the safety limits provided by the IEC-61400 norm.

Sicot *et al.*, (2008) investigated the aerodynamic properties of a wind turbine airfoil. Comparisons between pressure distributions and separation point position were performed, between rotating and non-rotating blades. In the presence of important free stream turbulence level, rotation seems to have no significant effects on the separation point position whereas, for the same angle of attack, the pressure on the suction surface is significantly lower for the rotating blade.

Abea and Ohwab (2004) carried out the wind tunnel tests consisting of surface pressure measurements on a horizontal axis wind turbine air foil which

was subjected to free stream turbulence levels. The results showed an influence of the free stream turbulence level on the separation point position. Experimental results showed lift augmentation for a rotating blade. The study of the separation point position coupled with the pressure distributions on the airfoil showed that this lift augmentation seems related to a lower value of the pressure in the separated area rather than to a stall delay phenomenon.

Kogaki *et al.*, (2004) studied the wind dynamics coupled with the turbine dynamic characteristics. The results revealed in a fairly complicated behavior. Thus, the common static model of calculating the average power which was based repeated on the turbine power curve and the average wind speed may result in increasing errors.

The development of special-purpose airfoils for horizontal-axis wind turbines (HAWTs) started from the time when nine airfoil families had been designed for various size rotors using the Eppler Airfoil Design and Analysis Code. A general performance requirement of the new airfoil families was that they exhibit a maximum lift coefficient for variable-pitch and variable-rpm rotors. The outboard airfoils having a high maximum lift coefficient lend themselves to lower blade solidity. The study of Wright and Wood (2004) revealed that airfoils having greater thickness result in greater blade stiffness and tower clearance and also airfoils of low thickness result in less drag which were better suited for downwind machines.

Jung *et al.*, (2005) found that the power output was significantly affected by the interval between the two rotors. Best performance was achievable when the interval remained at around one-half of the auxiliary rotor diameter.

The research done by Bermudez *et al.*, (2000) mostly concerned with solid (vane type) vortex generators and transpiration methods of suction and

blowing. They proposed to use air jets to generate stream wise vortices (AJVG) for interaction control. The effectiveness of air-jet vortex generators in controlling separation was proved. The focus was on the influence of AJVGs of various parameters on the separation region. The investigation results provided new guidelines for the design of AJVGs to obtain more effective separation control.

The effect of Reynolds number, height and interval of vortex generator were examined by the wind tunnel experiments carried out by Thumthae and Chitsomboon (2009). The preliminary CFD simulations were conducted to confirm the turbulent enhancement effect of the modified vortex generator.

Thumthae and Chitsomboon (2006) used CFD techniques to predict the optimal blade pitch angles that gave maximum power for wind turbine. For wind speeds 10.5 m/s and 7.2 m/s, optimal pitches occur at 8.82 degree and 4.2 degree respectively. Both values, when examined at 80 % span, correlate to the maximum lift point in pre-stall regions. This was used as a design criterion for an untwisted blade horizontal axis wind turbine.

By the numerical simulation of horizontal axis wind turbines with untwisted blade in steady state condition and investigating for the optimal pitch that produces the highest power output and relative velocity concept were obtained in the experimental investigation of Ohya *et al.*, (2005).

Jean and Chattot (2007) carried research on vortex model to account for blade flexibility to allow prediction of forces and bending moments along the blade and also to assess the fatigue life in operating conditions. When compared with the NREL experimental data, the results indicated that the code performs an accurate simulation of the coupled fluid structure interaction for attached flow conditions, at a computer cost that is acceptable for engineering purposes.

The power output, turbine availability, and other performance factors are either overestimated or underestimated. The errors were quantified by Wang *et al.*, (2008). Actual wind speeds were compared to projections based on long-term historical measurements. Turbine power curve measurements were compared with data provided by the manufacturers and loss assumptions were evaluated for accuracy. Overall, the projects performed well, particularly new commercial turbines in the first few years of operation.

Akcayoglu (2010) aimed to gain insights in the secondary flow field differences generated by common flow up (CFU) and common flow down (CFD) vortex generator configurations mounted on the equilateral triangular duct's slant surfaces with 30° angle of attack.

The starting performance of a three-bladed horizontal axis wind turbine was measured in field tests and compared with calculations employing a quasi-steady blade element analysis in the paper by Zwaba (2010). Accurate predictions of rotor acceleration were made for a large range of wind speeds, using a combination of interpolated aerofoil data and generic equations for lift and drag at high angles of incidence. The blade element calculations suggest that most of the starting torque was generated near the hub, whereas most power producing torque comes from the tip region.

Optimization of the rotor designs in the virtual wind tunnel was developed and annual power output of the wind turbine was calculated by Manela (2011).

Hernandez (1996) formulated a computational hydrodynamics method and implemented it for horizontal axis tidal turbines. Analysis and comparison were presented in terms of thrust coefficients, shaft torque/power coefficients, blade surface pressure distributions, and downstream velocity profiles. The key

implementation techniques and methodologies were provided in detail for the propeller based panel method tool. These measurements include downstream velocity profile which was essential for numerical wake vortices discretization.

7.4 Wind Turbine Blade Modeling

The HAWT is modeled as discussed in Chapter 4. The modeling of vortex generator shape and sizes are discussed in forth coming parts of this Chapter.

7.5 Design of Experiments

The design of experiments (DOE) is also referred to as designed experiments or experimental design. It can be used to reduce design costs by speeding up the design process. It reduces later engineering design changes, and reducing product material and labor complexity. Designed experiments are also powerful tools to achieve saving in manufacturing costs by minimizing process variation and reducing rework, scrap, and the need for inspection.

Factors influencing the experimental results can be classified as either controllable or uncontrollable variables. The controllable variables are generally referred to as factors.

The Design of an experiment addresses the questions outlined above by stipulating the following:

- The factors to be tested.
- The levels of those factors.
- The structure and layout of experimental runs, or conditions.

The *Table 7.1* shows a sample of combination containing various operational parameters of the HAWT with which the trials on the airfoil can be made to determine the localized flow separation (Wang *et al.*, 2008).

Experimenters often desire to avoid optimizing the process for one response at the expense of another. For this reason, important outcomes are measured and analyzed to determine the factors and their settings that will provide the best overall outcome for the critical-to-quality characteristics - both measurable variables and assessable attributes.

Table-7.1- Design of experiments –Combination

Section	Angle of attack(deg)	Wind speed(m/s)	Rotor speed (rpm)	Angular velocity(ω)	Relative velocity (m/s)	MACHNO
6	20	12	25	2.61666667	3.7	0.011212
7	20	12	25	2.61666667	6.31666667	0.019141
8	20	12	25	2.61666667	8.93333333	0.027071
13	20	12	25	2.61666667	22.01666667	0.066717
14	20	12	25	2.61666667	24.63333333	0.074646
15	20	12	25	2.61666667	27.25	0.082576
16	20	12	25	2.61666667	29.86666667	0.090505
17	20	12	25	2.61666667	32.48333333	0.098434
18	20	12	25	2.61666667	35.1	0.106364
19	20	12	25	2.61666667	37.71666667	0.114293
20	20	12	25	2.61666667	40.33333333	0.122222
21	20	12	25	2.61666667	42.95	0.130152
22	20	12	25	2.61666667	45.56666667	0.138081
23	20	12	25	2.61666667	48.18333333	0.14601
24	20	12	25	2.61666667	0.153939	

The DOE has been carried out using MINITAB software in order to find out the optimal combinations for all the sections of the air foils on which the analysis need to be focused.

Thus by using the DOE concept, the number of trials can be predicted along with the input values for the design foil tool. The number of trials has been found as (24*27=648) which is optimized to 181 trials using DOE.

7.6 Localized Flow Separation of the Wind over the Blade Surface

The tool used in this the part of study is DESIGN FOIL. This tool requires inputs in the form of:

- Angle of attack and
- Mach number (velocity parameter)

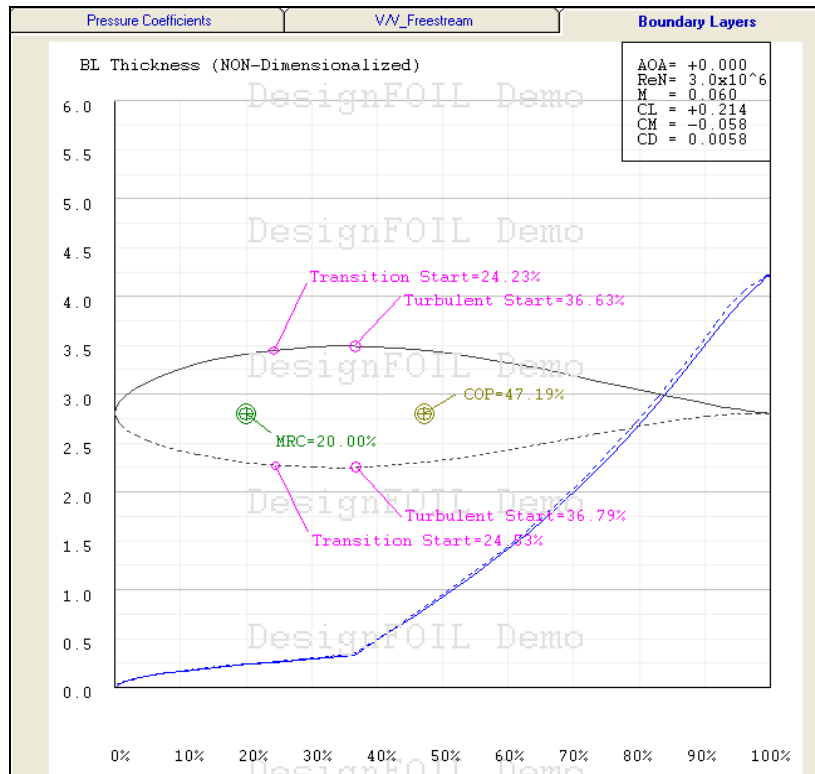


Figure 7.2 Flow Separation graph on airfoil

Table 7.2 Boundary Layer separation values at various points

INDEX	X-UPPER	Y-UPPER	BL-Thickness: Displacement
1	0.003970039	0.013805341	0.04326902
2	0.011503473	0.023222357	0.082315803
3	0.023153655	0.032642186	0.157784149
4	0.038728	0.041889	0.217407
5	0.058068	0.051091	0.276274
6	0.081014	0.060037	0.331005
7	0.107376	0.068479	0.387008
8	0.136939	0.076246	0.444695
9	0.169457	0.083213	0.501798
10	0.204664	0.089230	0.557404
11	0.242272	0.094086	0.614703
12	0.281973	0.097615	0.675603
13	0.323442	0.099650	0.742668
14	0.366337	0.099949	0.829300
15	0.410306	0.098395	1.326195
16	0.454981	0.095111	1.815072
17	0.499996	0.090289	2.319177
18	0.544979	0.084170	2.847337
19	0.589564	0.077034	3.402926
20	0.633389	0.069171	3.988500
21	0.676099	0.060875	4.604098
22	0.717353	0.052433	5.250898
23	0.756823	0.044128	5.923207
24	0.794195	0.036229	6.602769
25	0.829178	0.028949	7.272535
26	0.861495	0.022438	7.920586
27	0.890896	0.016793	8.528860
28	0.917150	0.012054	9.099771
29	0.940055	0.008237	9.592748
30	0.959431	0.005314	9.942072
31	0.975126	0.003171	10.170200
32	0.987012	0.001667	10.343637
33	0.994991	0.000678	10.532661
34	0.998997	0.000150	10.532661

This Design Foil tool is used to find the localized flow separation with respect to the (X, Y) coordinates system of the wing of HAWT. The vortex generated is located at the flow separation points on airfoil in such a way that it reduces the turbulence and maximizes the lift leading to more power generation.

The present study of the HAWT was carried out under the boundary conditions of

- Wind speed: 12 m/s.
- Rotor Speed: 25 rpm.

Considering the relative velocity at the various sections of the blade with angle of attack of 20° , the localized flow separation has been calculated.

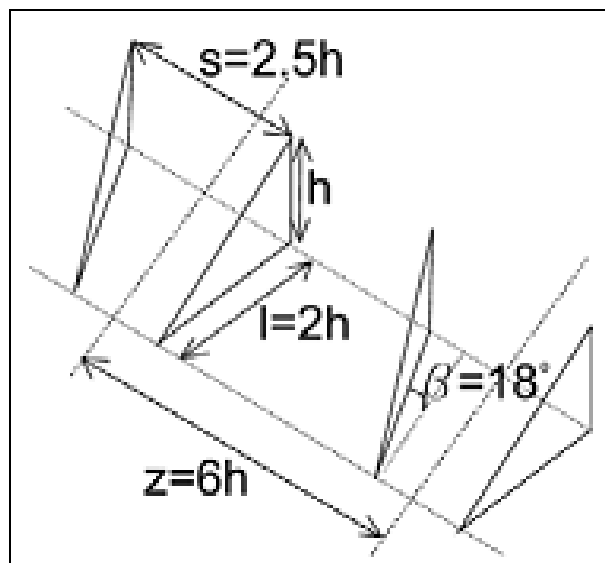


Figure 7.3 Configuration of Vortex generator (Source: lmwindpower.org, autospeed.com)

The general dimensions of a typical vortex generator are shown in *Figure 7.3*.

Table 7.3 Configuration of Vortex generator at various sections of the Blade

Section	Height h	S = 2.5h	L = 2h	Z = 6h
1	24.12	60.3	48.24	144.72
2	26.54	66.35	53.08	159.24
3	21.28	53.2	42.56	127.68
4	29.54	73.85	59.08	177.24
5	26.76	66.9	53.52	160.56
6	23.46	58.65	46.92	140.76
7	21.75	54.375	43.5	130.5
8	35.36	88.4	70.72	212.16
9	33.09	82.725	66.18	198.54
10	31.76	79.4	63.52	190.56
11	32.81	82.025	65.62	196.86
12	21.98	54.95	43.96	131.88
13	23.34	58.35	46.68	140.04
14	27.82	69.55	55.64	166.92
15	22.27	55.675	44.54	133.62
16	34.14	85.35	68.28	204.84
17	34.48	86.2	68.96	206.88
18	30.28	75.7	60.56	181.68
19	28.49	71.225	56.98	170.94
20	26.57	66.425	53.14	159.42
21	23.41	58.525	46.82	140.46
22	20.69	51.725	41.38	124.14
23	17.88	44.7	35.76	107.28
24	15.57	38.925	31.14	93.42
25	14.1	35.25	28.2	84.6
All dimensions are in mm				

Considering the span-wise station no 6 of the blade shown in Table 4.1, the corresponding airfoil's co-ordinates are given as input to the lab fit software and the curve is extracted as shown in Figure 7.5

The mathematical equation of the extracted curve in Equation (7.1) was obtained from the software result as shown in Figure 7.6

7.7 Mathematical Model

An attempt has been made to develop a mathematical model to determine the boundary layer thickness at the localized flow separation surfaces. The methodology for developing the model is given in Figure 7.4.

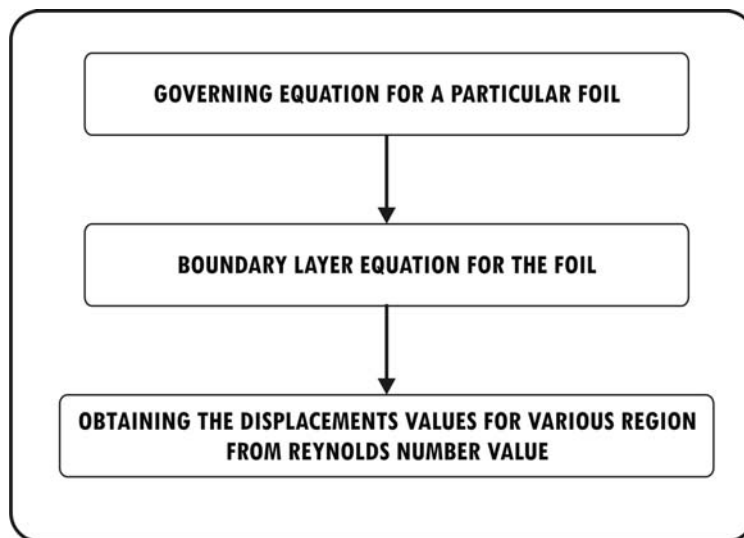


Figure 7.4 Methodology for developing the model

$$Y=Ax^2+B: A=0.493*10^{-2}; B=0.01345 \dots\dots\dots(7.1)$$

Equation on the curve at the station i.e spanwise distance of 6 m from the root of the blade is obtained by using the Lab Fit software

Governing equation of the 6th section of the blade is

$$Y = AX^2+B \text{ where } A = - 0.4693*E-2 \ \& \ B = 0.1345*e-1$$

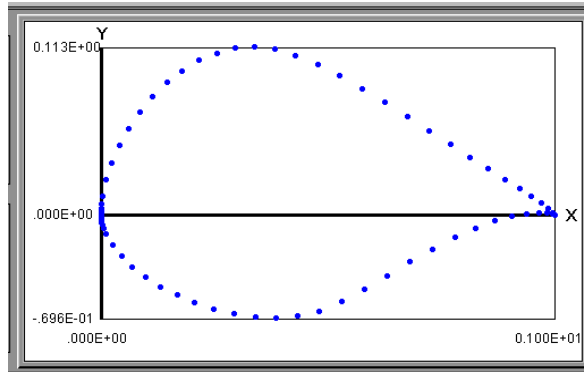


Figure 7.5 Airfoil curve extracted in LABFIT

Figure 7.5 shows the airfoil curve extraction in LABFIT software. The upper and lower curve co-ordinate values are given as input to the software. Then the curve is given as input to the LABFIT software to get the governing mathematical equation of the airfoil curves.

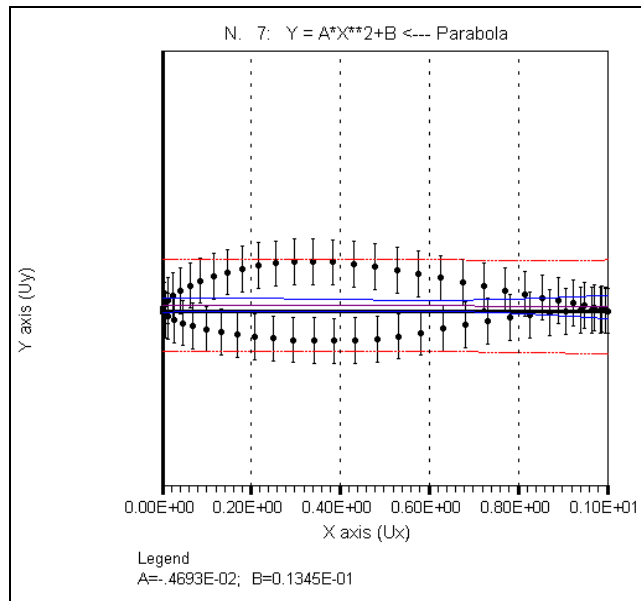


Figure 7.6 Curve equations in LABFIT

The LABFIT software gives the curve equation as shown in *Figure 7.6*. For the blunt surface, the boundary layer relation is obtained by (www.bakker.org)

$$d/dx \left(\int_0^\delta u(u_\infty - u) dy \right) = v \frac{du}{dx} \text{ at } y=0 \dots\dots\dots(7.2)$$

Velocity gradient:

$$\frac{u}{u_\infty} = \frac{y}{\delta} \dots\dots\dots(7.3)$$

$$\int_0^\infty \left[\frac{u_\infty^2}{\delta} - \frac{u_\infty^2}{\delta^2} y^2 \right] dy = \left[\frac{u_\infty^2}{2} - \frac{u_\infty^2}{3} \frac{\delta}{\delta} \right] \dots\dots\dots(7.4)$$

$$\frac{d}{dx} \left[\frac{u_\infty^2}{6} \delta \right] = V \frac{u_\infty}{\delta}$$

$$\frac{u_\infty^2}{6} \frac{d\delta}{dx} = V \frac{u_\infty}{\delta} \dots\dots\dots(7.5)$$

Using Variable of separation

$$\delta d\delta = \frac{6V}{u_\infty} dx \dots\dots\dots(7.6)$$

$$\delta^2 = \frac{12x^2}{V/u_\infty x} = \frac{12x^2}{Re}$$

$$\delta = \frac{3.464x}{Re} \dots\dots\dots(7.7)$$

Boundary layer displacement

$$\delta_d = \int_0^\delta \left[1 - y/\delta \right] dy \dots\dots\dots(7.8)$$

'dy' is obtained by differentiating the governing equation.

Sample calculation to predict the (δ) laminar boundary layer thickness of for section no 6 is given below.

$$Y = Ax^2 + B; A = 0.493 \times 10^{-2}; B = 0.01345$$

$$Y = 0.493 \times 10^{-2} x^2 + 0.01345$$

$$\int_0^{\delta} [1 - y/\delta] dy = 0$$

$$\left[(0.493 \times 10^{-2} x^2 + 0.01345) - \frac{(0.493 \times 10^{-2} x^2 + 0.01345)}{\delta} \right] = 0$$

$$4.93 \times 10^{-4} \delta^3 + 0.01345 \delta - 2.435 \times 10^{-7} \delta^2 + 1.81 \times 10^{-4} = 0$$

$$\delta = 6.814 \text{ mm}$$

Based on the total boundary layer thickness, the size of the vortex generators were calculated and the results are shown in *Table 7.3* (Whale et al., 2000, Wright and Wood, 2004).

7.8 Modeling of Blade with VG

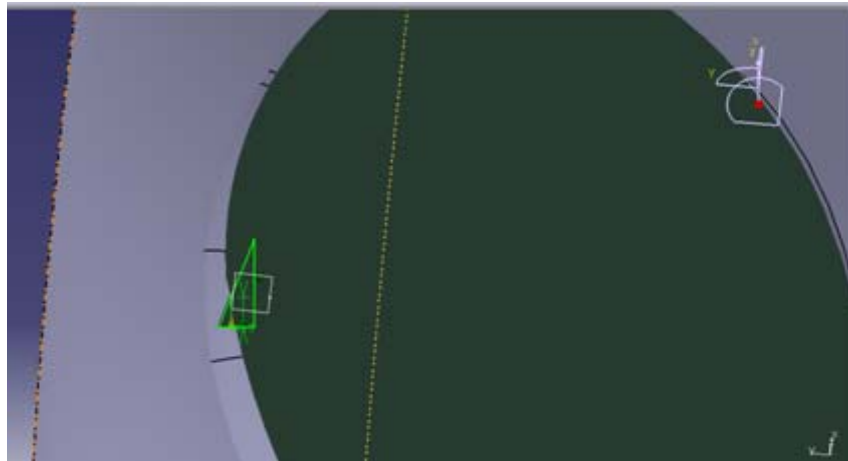


Figure 7.7 Construction of Vortex generator

The construction of a vortex generator on the airfoil of HAWT in modeled in CATIA V 5 as shown in *Figure 7.7*

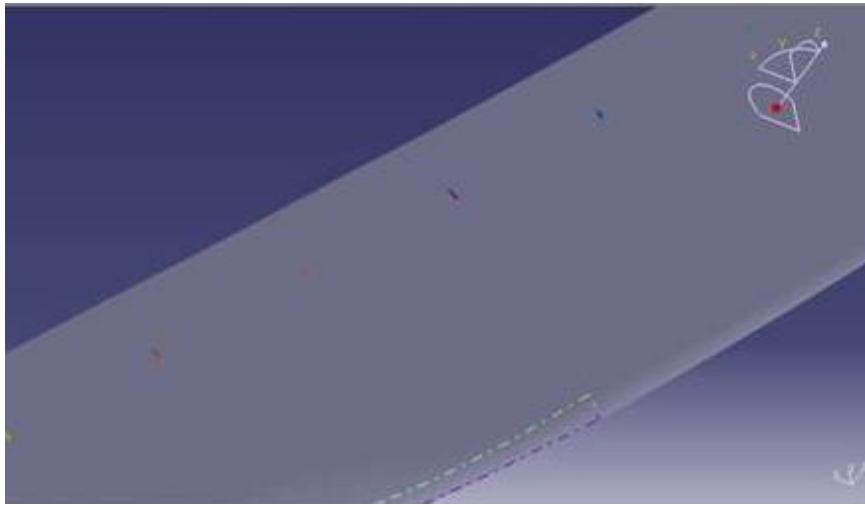


Figure 7.8 Array of VG on single blade

The layout of vortex generator on the blade is shown in *Figure 7.8*

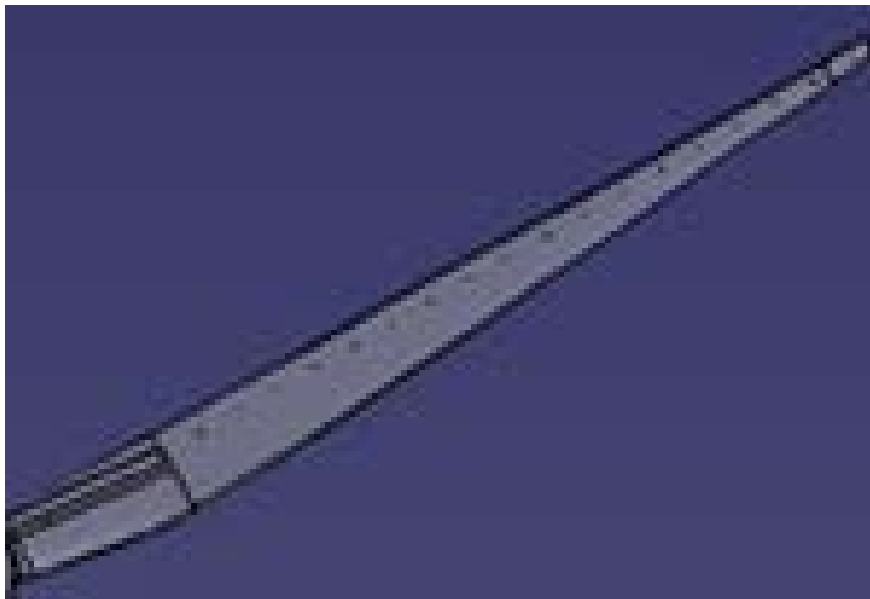


Figure 7.9 Array of VG on the Single blade at various sections

Figure 7.9 shows the space position of vortex generator of the blade.

7.9 CFD Analysis of HAWT Model with VGs

Very fine tetrahedrons meshes were made in and around the blade of the HAWT to capture the flow physics accurately. The meshing around the blade is shown in *Figure 7.10*.

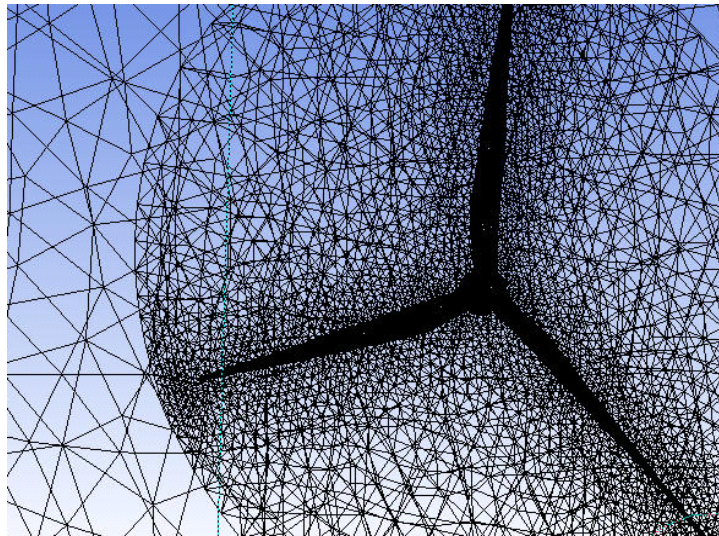


Figure 7.10 Meshing of the Blade

The iteration and residuals levels during numerical analysis are shown in *Figure 7.11*.

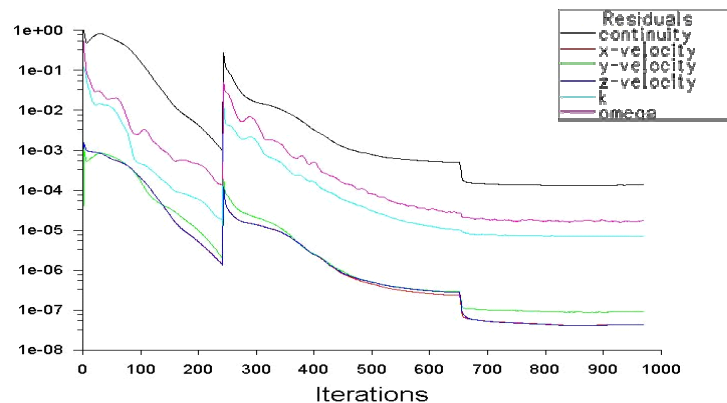


Figure 7.11 Iterations residuals

The residuals are kept as low as in the order of $1e-6$ to get accurate results.

7.10 Results & Discussion

Following results are obtained from this part of analysis.

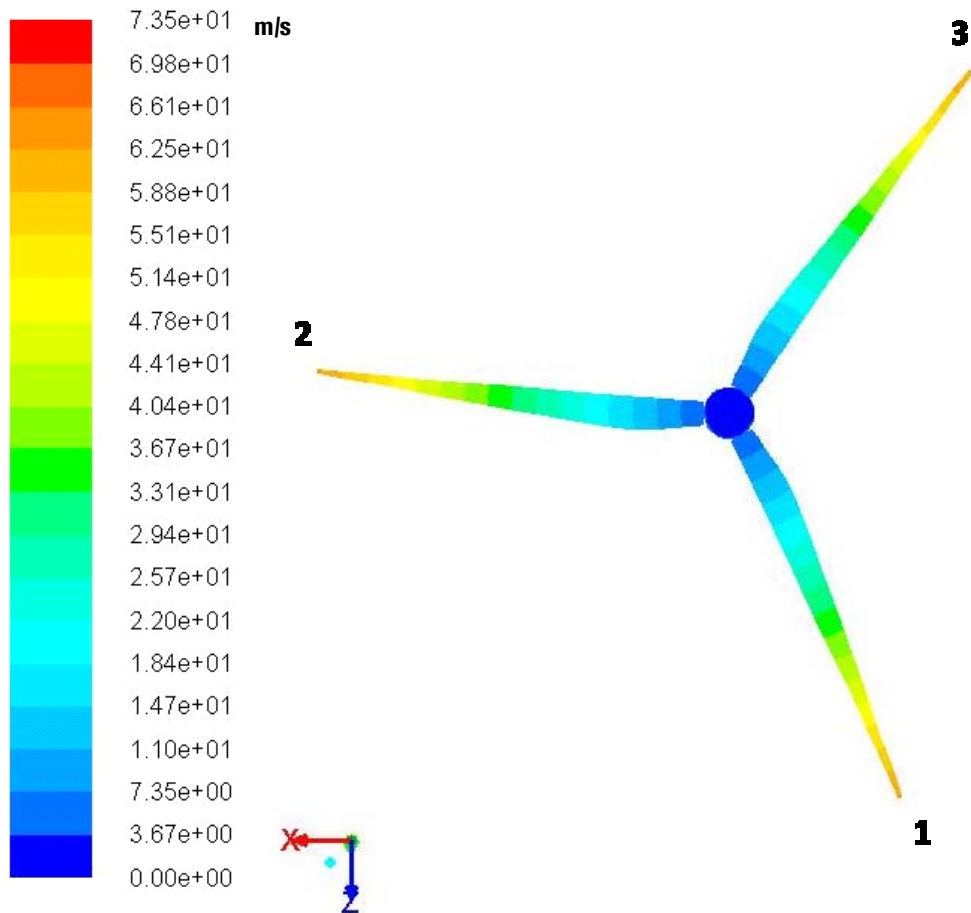


Figure 7.12 Velocity contour plots on the blades

Figure 7.12 shows the velocity contour on the three blade surface. The hub region and roots of blade have low velocity range of zero to 3.5 m/s and the velocity increases along the radii of blades and reaches maximum values around 60 m/s at tip region.

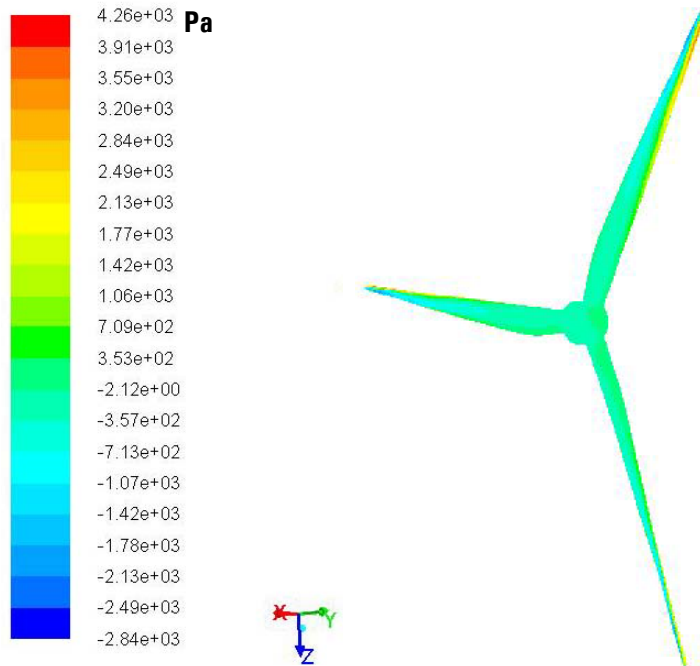


Figure 7.13 Pressure contour plots

Figure 7.15 shows the pressure contour over the three blades.

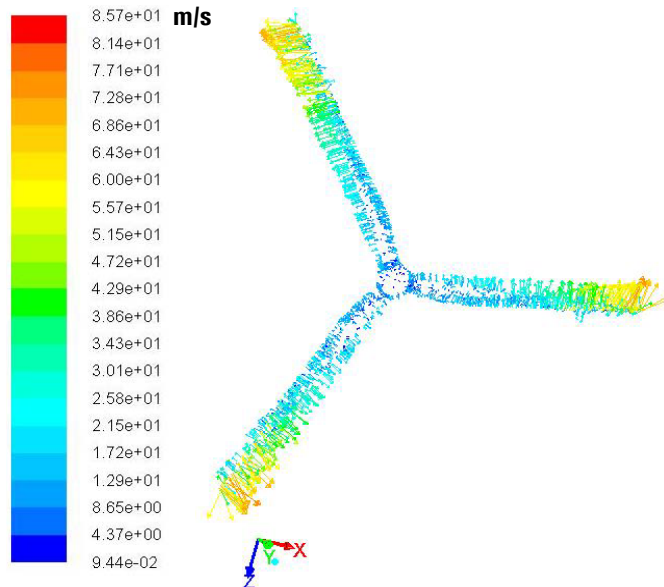


Figure 7.14 Velocity vector plot over the blades viewed from inlet

Figure 7.14 shows the velocity vector plotted around the three blades of HAWT.

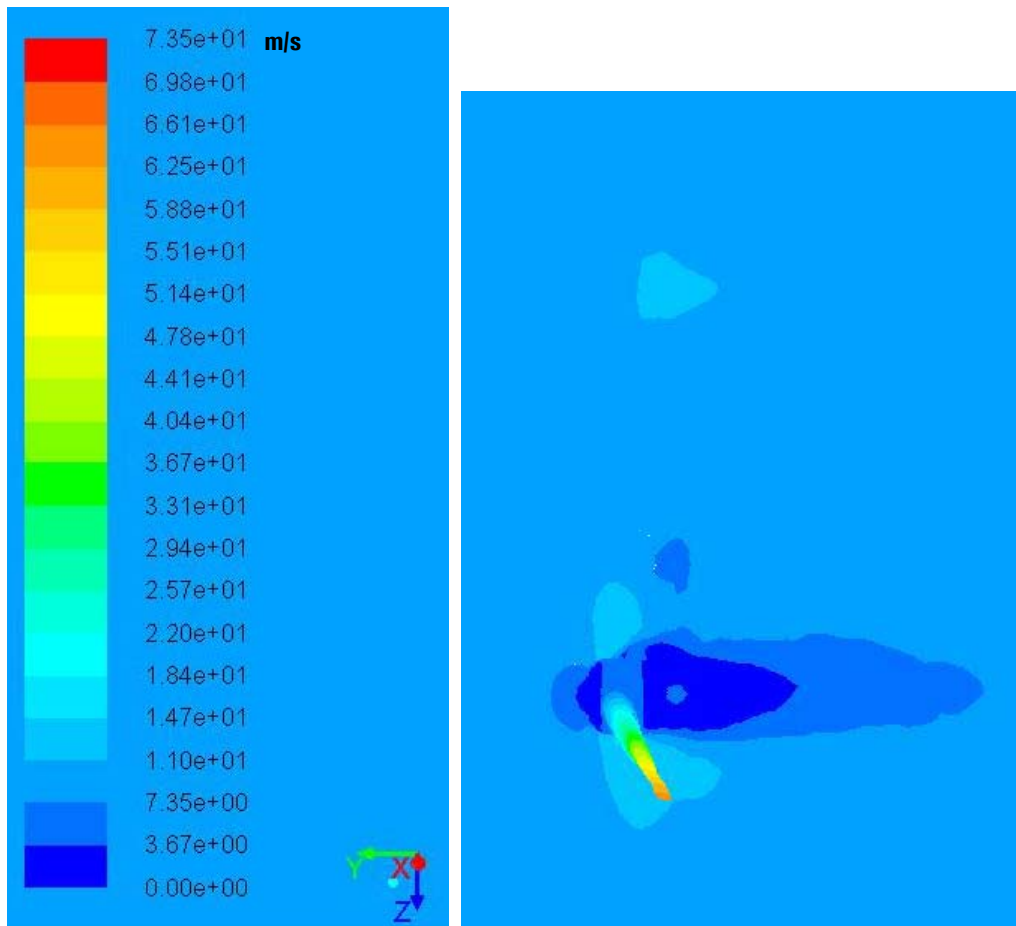


Figure 7.15 Velocity vector plot by sweep surface along X direction

Figure 7.15 shows the velocity vector along the sweep surface in X direction.

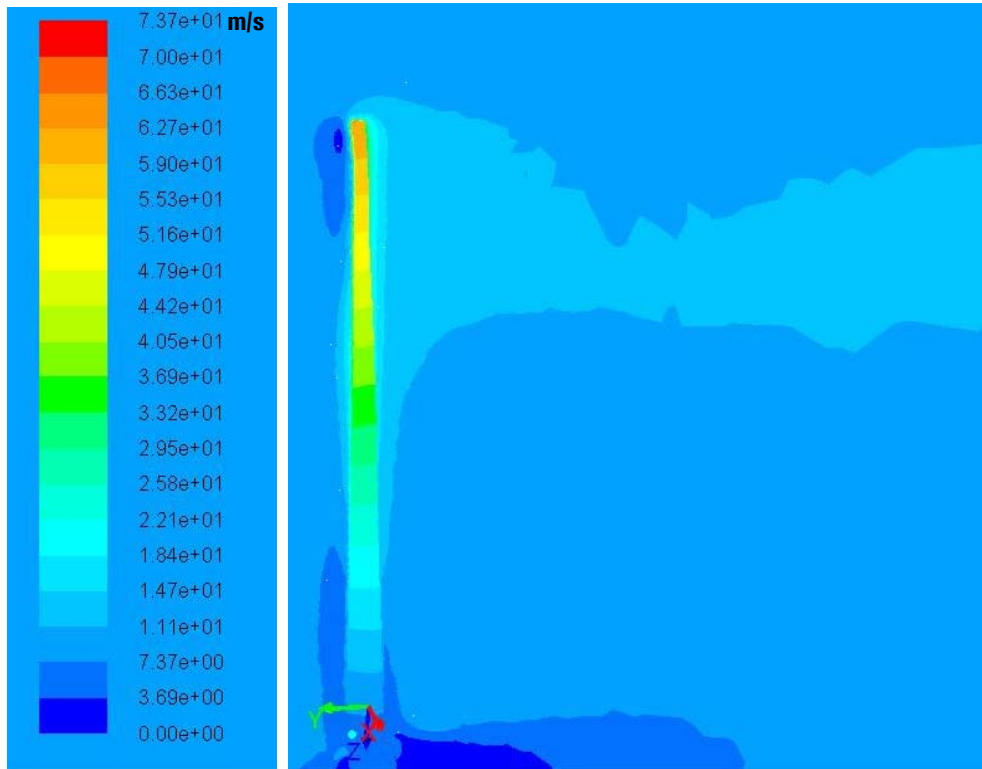


Figure 7.16 Velocity vector plot by sweep surface along Y direction

The velocity vector along the sweep surface in Y direction of the HAWT is shown in *Figure 7.16*.

It is clear from the figure that the velocity drops behind the HAWT.

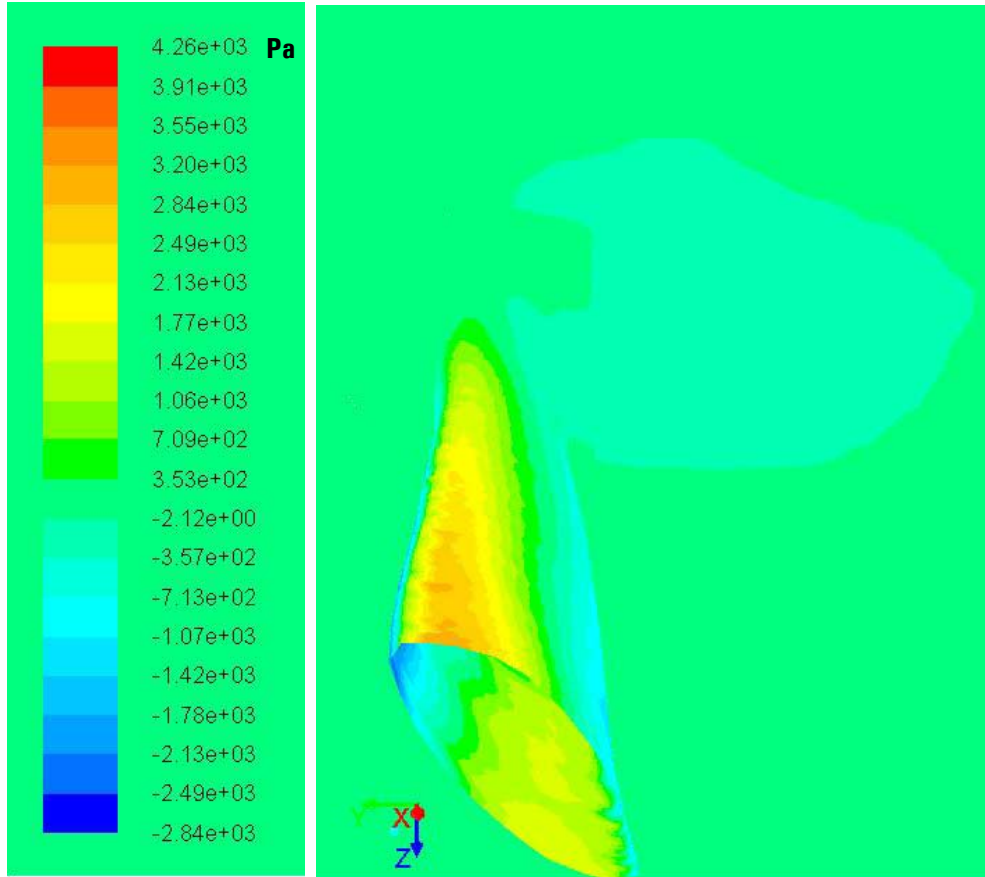


Figure 7.17 Total Pressure plot by sweep surface along Y direction.

The total pressure plot by sweep surface along the Y direction in depicted in the *Figure 7.17*. The leading edge of the blade experiences the maximum pressure in the range of 300 Pa.

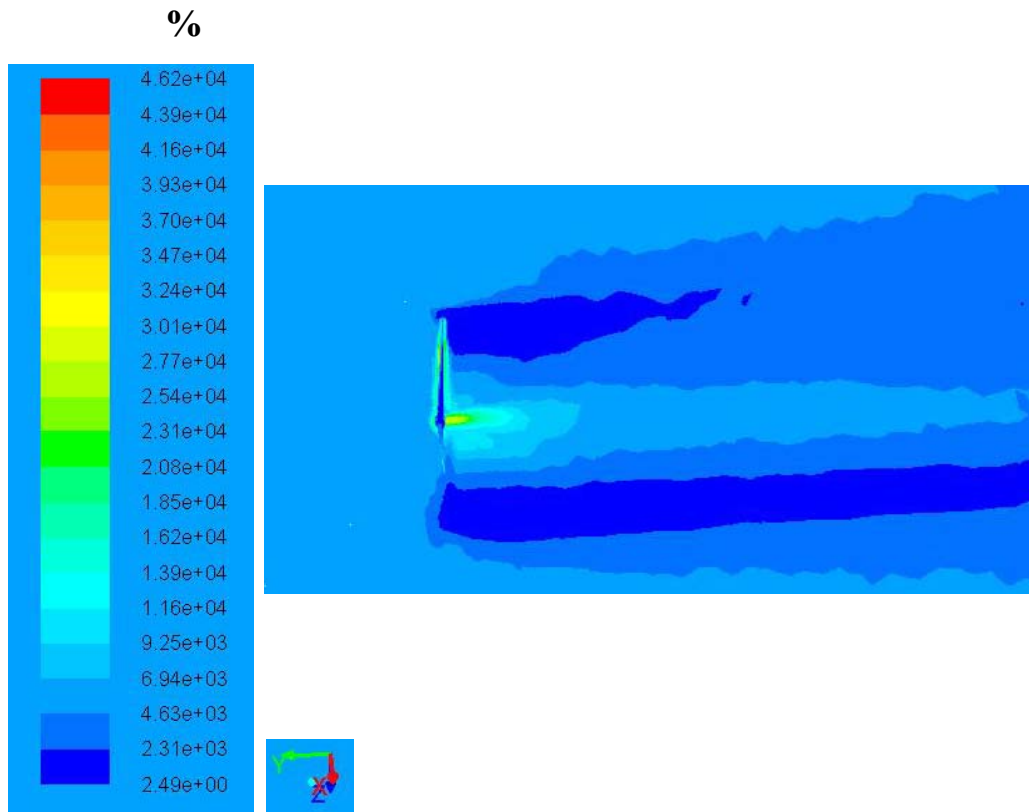


Figure 7.18 Turbulence plot by sweep surface along X direction.

Figure 7.18 shows the turbulence levels on the sweep surface along X direction in terms of %. The tips of the blades create minimum turbulence level behind them.

Higher level of turbulence in the middle sweep region is created.

Table 7.4 shows the moments generated by the rotating parts of the HAWT. The three blades generate pressure moment and viscous moments.

The numerical simulation results give the moments generated about all three X, Y and Z axis. Since the wind is flowing along Y axis the moment

generated along the Y axis alone taken for power generation. This table shows the moment generated by the three blades with VGs.

The *Table 7.5* shows the moment generated by the three blades without the VGs.

By comparing the *Table 7.4 and Table 7.5* the increase in power generated by the three blades because of introduction of VGs is established.

All the three blades generate additional pressure moments because of the introduction of VGs.

Table 7.4 Moments generated by three blades with VG

Zone	Pressure moment N-m			Viscous moment N-m			Total moment N-m		
	X	Y	z	x	Y	z	X	Y	z
Blade1	-356800	82590.36	-197092	276.434	1324.511	158.3966	-356523	83914.87	-196933
Blade2	4288.336	34219.87	389044.5	-82.2673	1360.867	-159.247	4206.069	35580.74	388885.2
Blade3	386019.5	100879.3	-218437	-218.452	1051.828	273.641	385801.1	101931.1	-218164
Total	33507.836	217689.53	-26484.5	-24.2853	3737.206	272.7906	33484.169	221426.71	-26211.8

Table 7.5 Moments generated by the three blades without VG

Zone	Pressure moment N-m	Viscous moment N-m	Total moment N-m
Blade1	80267.95	761.66	81029.62
Blade2	31301.67	901.53	32203.2
Blade3	98778.86	563.42	99342.28
Total	210348.5	2226.61	212575.1

Through this present study the technique of exploring the capabilities of CFD for enhancing energy generation has been addressed. The innovative

Vortex generator concept in wind turbines was studied, and the improvements were shown in terms power generated. The Mathematical equations were formulated for predicting the flow separation and determining the boundary layer thickness of a rotating aerofoil. For instance, 6 m away from hub the blade had a boundary layer thickness of about 6.125 mm starting laminar transitions under the wind speed of 10 m/s and a rotor speed of 25 rpm.

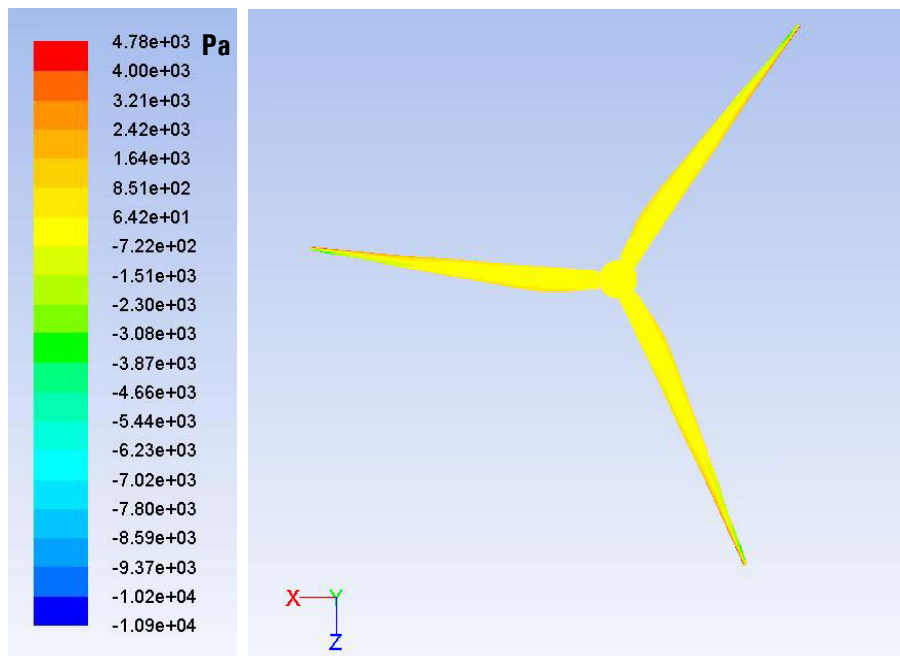


Figure 7.19 Pressure contour on the blade surfaces

Pressure contour of the three blade surfaces are shown in the *Figure 7.19*.

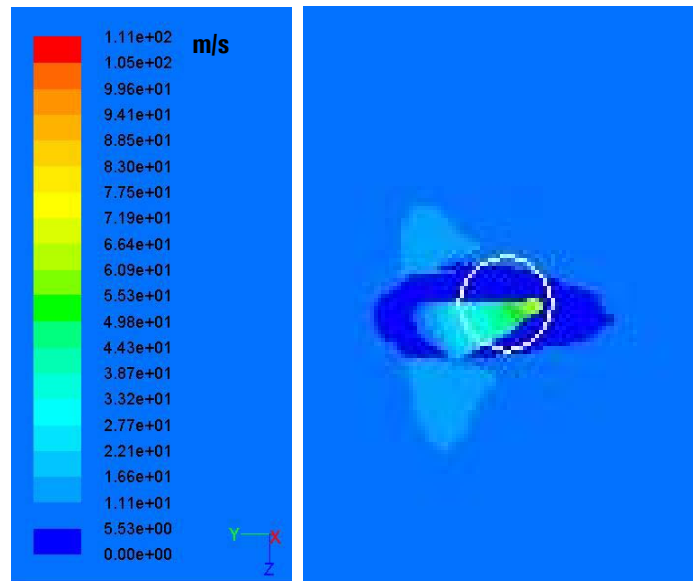


Figure 7.20-Velocity contour with sweep surface in X axis

Figure 7.20 shows the velocity contour along the sweep surface created along the Z axis of the domain created for analyzing the HAWT with VG.

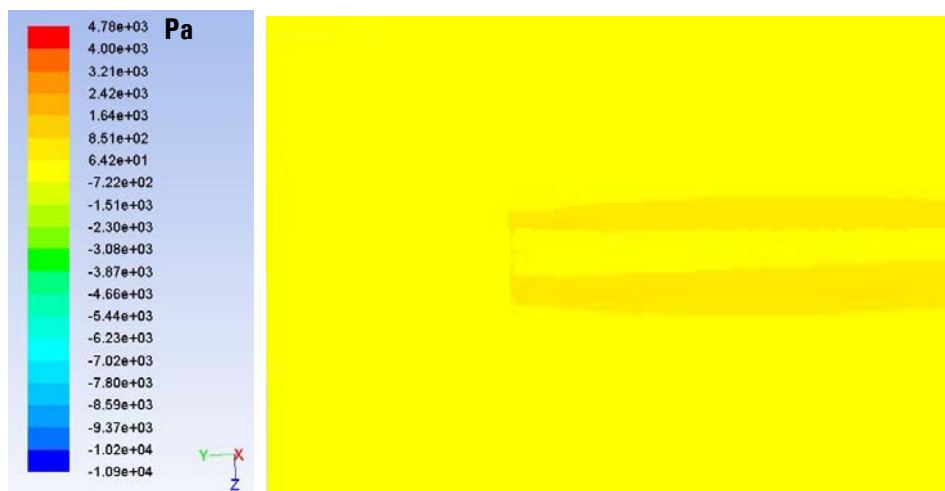


Figure 7.21 Pressure contour with sweep surface in X axis

Figure 7.21 shows the pressure contour along the sweep surface created along the Z axis of the domain created for analyzing the HAWT with VG.

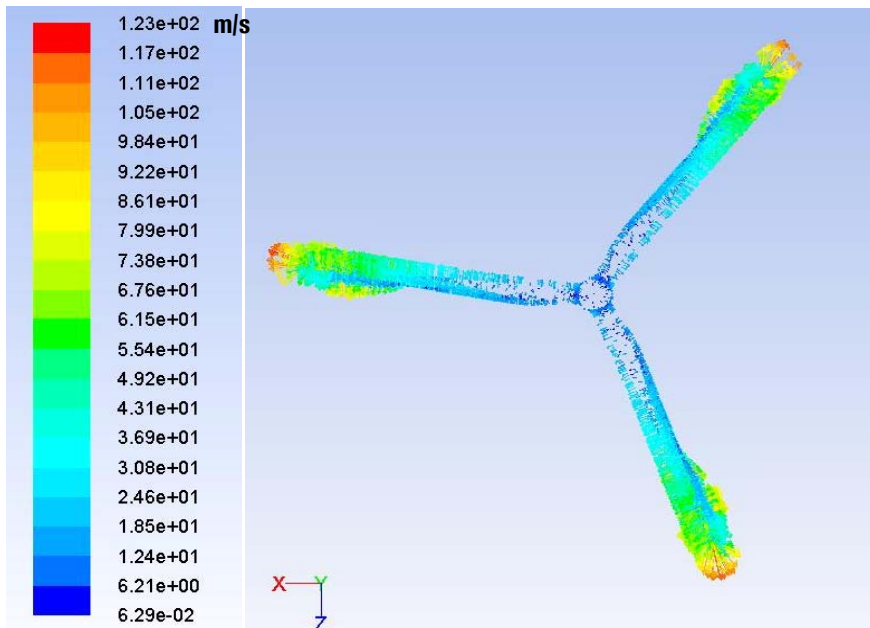


Figure 7.22 Velocity vector plot over the blades viewed from outlet

Figure 7.22 shows the velocity vector plot over the surfaces of the three blades of the HAWT.

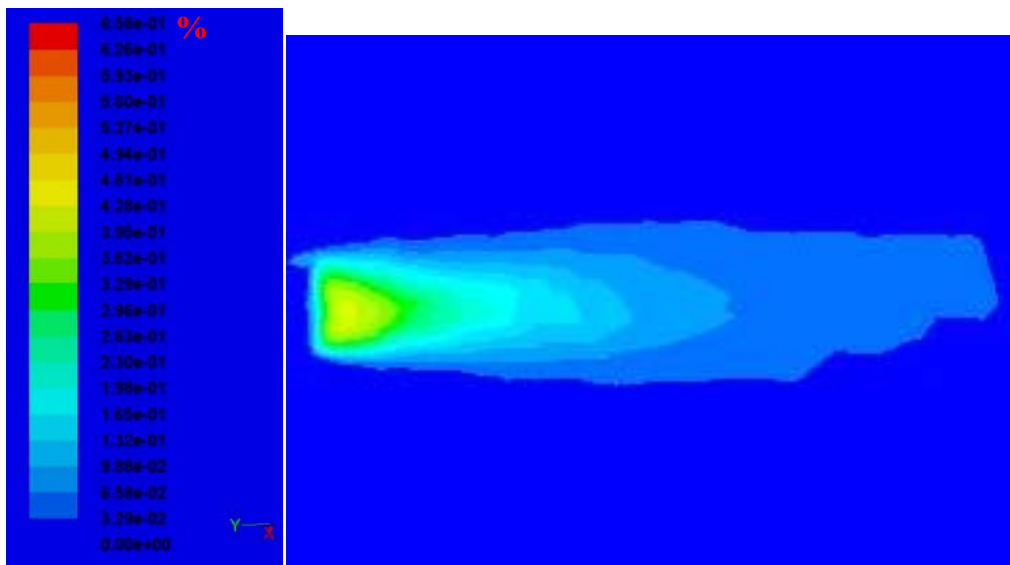


Figure 7.23 Turbulence plot of wake region

Turbulence plot is shown in the *Figure 7.23* and it is evident that near the HAWT the level of turbulence is of maximum and over the wake distance away from the HAWT it is dissipating.

7.10.1 Comparison Study

The Table 7.7 explains the blade performance with the proposed technique of introduction of the VGs to existing one without the VGs.

Table 7.6 Comparison of the moments generated.

Description	Moment without VGs in N-m	Moment with VGs in N-m
Wind blade performance	212576.84	221425.87

The introduction of Vortex generator at correct position helped to increase 4 % of power generation to the existing model at moderate wind speed of 10 m/s. Thus it is proved that the technique of introduction of the Vortex generators had a good result with the increase in the power generation.

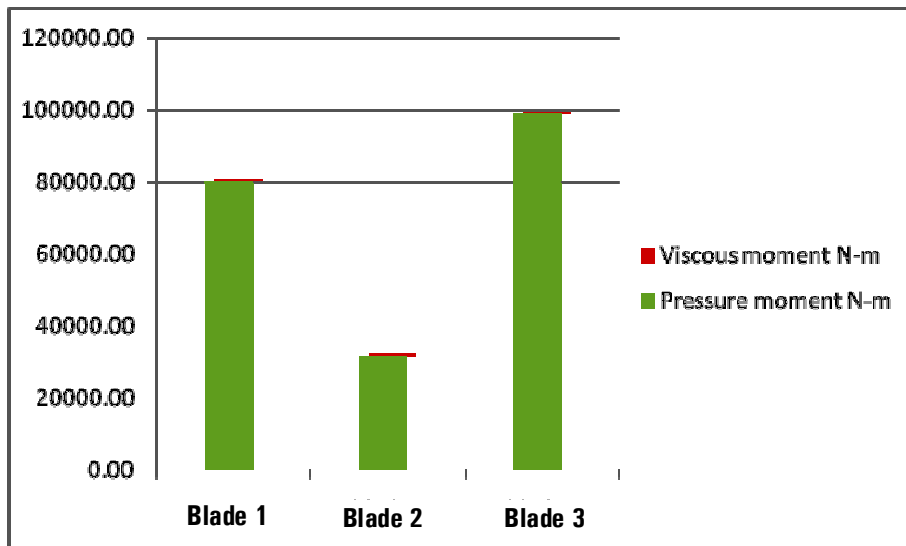


Figure 7.24 Moments generated by the three blades without VGs.

Figure 7.24 shows the viscous and pressure moments generated by the three blades without the VGs.

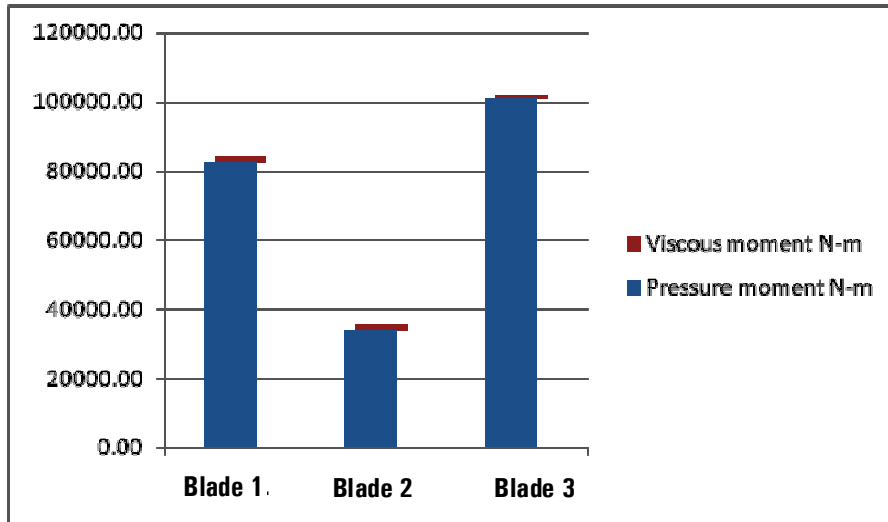


Figure 7.25 Pressure moment and viscous moment generated by the three blades with VGs.

Table 7.7 Moments generated by the three blades.

Zone	Pressure moment (with VG) Nm	Pressure moment (without VG) Nm	Viscous moment (with VG) Nm	Viscous moment (without VG) Nm	Total moment (with VG) Nm	Total moment (with VG) Nm
Blade1	82590.36	80267.95	1324.51	761.66	83914.87	81029.62
Blade2	34219.87	31301.67	1360.87	901.53	35580.74	32203.2
Blade3	100879.3	98778.86	1051.83	563.42	101931.1	99342.28
Total	217689.5	210348.5	3737.21	2226.61	221426.7	212575.1

The pressure and viscous moments generated by the three blades in N-m are tabulated and compared in the *Table 7.7*. It can be established from the above *Table 7.7* that the introduction of VGs increase both pressure and viscous moments unlike the surface roughness optimization technique discussed in Chapter 5 which increases only viscous moments.

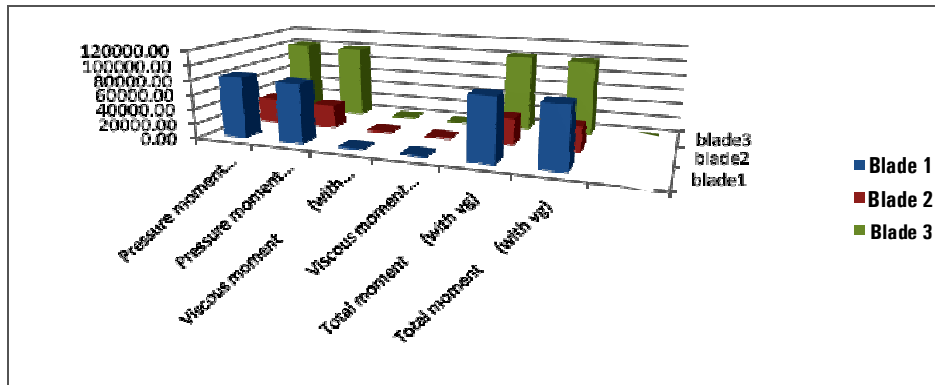


Figure 7.26 The comparison of pressure and viscous moments generated.

Figure 7.26 shows the comparison of pressure and viscous moments generated the three blades in which the viscous moments values are negligible when compared to the pressure moment values.

7.12 Conclusions

The numerical simulation of the effects of introduction of VG in the HAWT resulted in the following conclusions.

- The boundary layer thickness of the air flow over the blade of the HAWT can be predicting using software like LABFIT and DESIGNFOIL.
- A procedure has been attempted to find out the correct size of the VGs to be introduced on the blade of the HAWT.
- The introduction of correct size VGs at appropriate locations over the blades of the selected HAWT is found to increase the power production about 4 %.



Chapter -8

SUMMARY AND CONCLUSIONS

8.1 Summary

In chapter 1 the current wind current energy scenario of India is given. The motivation for the present research is given with reasons for selecting CFD approach for analyzing the Horizontal Axis Wind Turbine (HAWT). The overall objectives of the work and an over view of the thesis are given in Chapter 1.

The present status of wind power technology and the functioning of HAWT with its types and its components are discussed in Chapter 2. Various aspects of HAWT such as stall control, pitch control and active stall with operating conditions are discussed in the same Chapter. The aerodynamic models of wind mill blade theories are briefed in this Chapter. The performance appraisal techniques of airfoils namely BEM, lifting line, actuated disc, Paneled Vortex Methods and Navier Stokes Solvers are elaborately addressed. A detailed literature review on wind mill aerodynamics forms part of Chapter2.

In Chapter 3 the governing equations of CFD, particle approach and field approach are addressed. The continuity and momentum components of Navier Stokes equations are also discussed in this Chapter with solution procedures. A literature review on CFD approach to HAWT analysis is also given.

Chapter 4 discusses the performance evaluations of the selected Horizontal axis wind turbine. Its general aerodynamic behavior is also studied. This Chapter demonstrated the potential of an incompressible Navier–Stokes CFD approach for the analysis of horizontal axis wind turbines. The result obtained by CFD analysis has been validated against the experimental data of the NREL power performance testing activities. Comparisons are shown for the surface pressure distributions at several stations along the blades as well as for the field domain. They were availed from the post processing techniques through CFD. In addition to a comparison between measurements reported by NREL and CFD simulations, comparisons are made for the local flow angle at several stations ahead of the wind turbine blades. For attached and moderately stalled flow conditions the pressure distribution and torque predictions were seen fair, subsequently, the wind-field effects on the blade aerodynamics, as well as the blade/tower interaction were investigated. The selected case corresponded to 12.5 m/s up-wind HAWT at zero deg of yaw angle and a rotational speed of 25 rpm.

In Chapter 5, the design optimization of HAWT blades is discussed. The effects of surface roughness factor on the performances of HAWT are analyzed using CFD approach. The literature deals with surface roughness of wind mill blades and the CFD approach is reviewed in the Chapter.

The technique of achieving better power generation at low wind speed conditions lower than cut in speed of HAWT is discussed in Chapter 6. The performance of the gurney flaps is analyzed using CFD. An analysis of the introduction of winglets at the tip of the blades for avoiding turbulence at the tip region is also given in the Chapter.

Chapter 7 analyses the role of vortex generators introduced over the blades in obtaining maximum lift and power generation from HAWT.

8.2 Conclusions

The obtained results suggested that the present research method can cope well with the flows encountered around HAWT providing useful results for their aerodynamic performance and revealing flow details near and off the blades as well as around the tower.

- A whole assembly of wind turbine can be modelled to the real size with all the features like complete, cone angle and tilt angle. The complete profile of the blade can also be modelled without losing its geometry which contributes to flow physics. The finite and fine pitch angle can be modelled and performance could be studied. The power generation from a HAWT can be predicted for any pitch angle.
- The wind shear can be simulated for varied ground surface conditions and turbulence intensity levels and their effects on wind turbine performance could be studied. Static pressure over the surface of the HAWT structure can be analysed by visualising the static pressure contour. Similarly dynamic pressure, absolute pressure and relative velocities can be studied. The wind turbine solidity and its effects could also be studied.
- Turbulence levels and relative positions in the swept domains of HAWT using CFD can be well analysed. The vortices and wake generated could be well predicted over the wake region. The resultant moments generated by each blade at any position of rotation relative to the tower can be well predicted. This is very important in analysing the tower influence and shadow effects. The pressure load at any point on the surface of the blade can be predicted and this can be used to design aero elasticity effects.

- Interestingly the power generated by similar blades of the HAWT varies with respect to their space positions. It is found that power generation will be more when the blade is approaching the tower during rotation and the power generation by the same blade will be less when the blade moves away from the tower. This shows the significance of the CFD based multibody dynamics approach for the analysis of the HAWT performance. The study proved that when angle of attack increases the lift force keeps on maximizing and at a particular angle, flow over the air foil separates leading to stall.

The capability of numerical methods to solve the NS equation with the bound flow of air over the blades of HAWT with various surface roughness values is established.

- The analysis shows that the viscous moments generated by the blades increases with increase in surface roughness values. The velocity of air is not much changed by increase in surface roughness value and thus the pressure moment generated is not approachable changing.
- Because of the change in surface roughness value, the friction between the blade surface and flowing air increases, thus leading to increase in the viscous moment.
- The study shows that there is a sharp increase in viscous moment generation with increase in surface roughness value on the pressure sides of turbine blades.
- By optimizing the surface roughness value power generation from an HAWT can be increased by approximately 1.5 %.
- The concept of introducing the gurney flap is proved with increase in the aerodynamic power generation.

- A model of HAWT with flapped wings and winglets at the end of the blades can be effectively modeled for numerical simulation and analyses. The gurney flaps of the blades in the HAWT effectively changes the aerodynamic performances.
- At wind speeds lower than the cut in speed the gurney flapped blade of the HAWT generated excess moments.
- The introduction of gurney flaps increases the power generation from 233 kW to 450 kW wind speed range 3 m/s. The introduction of the winglets at the tip of the blades rotating at high tip speed ratio can be effectively modeled and analyzed. The total moments generated by the HAWT was found to increase considerably by the introduction of winglets.
- The boundary layer thickness of the air flow over the blade of the HAWT can be predicted using software like LABFIT and DESIGN FOIL.
- A procedure has been attempted to find out the correct size of the VGs to be introduced on the blade of the HAWT.
- The introduction of correct size VGs at appropriate locations over the blades to the selected HAWT is found increase the power production about 4%.

8.3 Scope for Future Research

The present work focuses on the performance appraisal of HAWT through CFD approach. This analysis can be extended to a vertical axis wind turbine (VAWT).

There is also scope for extending the study for localized surface roughness conditions on turbine blades.

The interaction between the turbine blades and the tower may be further examined to maximize the power generation while the blades approach and leave the tower during their rotation. The blade tower interaction can be further examined to minimize the unbalanced power production while approaching and leaving of a blade over the tower.

Further there is scope for effectively blending the aero elasticity behaviors of the blades with flexible gurney flaps techniques.



REFERENCES

1. Abea Ken-ichi, Yuji Ohyab-An investigation of flow fields around flanged diffusers using CFD- *Journal of Wind Engineering and Industrial Aerodynamics* 92(2004) 315–330
2. Akcayoglu Azize -Flow past confined delta-wing type vortex generators - *Experimental Thermal and Fluid Science* 35 (2010) 112–120
3. Amano R.S. , R.J. Malloy,' *CFD Analysis on Aerodynamic Design Optimization of Wind Turbine Rotor Blades'* *World Academy of Science, Engineering and Technology* Vol 60, 2009,
4. Amiralaei M.R., H.Alighanbarin, S.M.Hashemi, "An investigation in to the effects of unsteady parameters on the aerodynamics of a low Reynolds number pitching airfoil", *Journal of Fluids and Structures* 26(2010)979–993
5. Anderson J., *Computational Fluid Dynamics*, Mcgraw hill Inc 1995
6. Anon., *Wind Turbine generator System, part 1: Safety Requirements. IEC Standard 61400-1, International Electro technical Commission, geneva 1999.*
7. Baxevanou C.A., P.K. Chaviaropoulos, S.G. Voutsinas, N.S. Vlachos 'Evaluation study of a Navier– Stokes CFD aeroelastic model of wind turbine airfoils in classical flutter' *Journal of Wind Engineering and Industrial Aerodynamics* 96 (2008) 1425– 1443

8. *Bechert D. W., R. Meyer and W. Hage. Drag reduction of airfoils with Miniflaps. Published in AIAA -2000-2315.*
9. *Bennett M. Robert and John W. Edwards,' An Overview of Recent Developments in Computational Aeroelasticity 'AIAA 98-2421*
10. *Bermudez L., A. Velazquez and A. Matesanz-Numerical Simulation of Unsteady Aerodynamics effects in Horizontal-Axis Wind Turbines-Solar Energy Vol. 68, No. 1, (2000), pp. 9–21,*
11. *Bourdin P., A. Gatto, and M.I. Friswell. "The Application of Variable Cant Angle Winglets for Morphing Aircraft Control" published in AIAA 2006-3660.*
12. *Brown L. and A. Filippone. "Aerofoil at low speeds with gurney flaps" Published in Journal of Aircraft in September 2003.*
13. *Burton, David Sharpe, Ervin Bossanyi Wind Energy Handbook, John Wiley & Sons, Ltd, 2001.*
14. *Byung-Young Min, Lakshmi N. Sankar, Nischint Rajmohan and JVR Prasad. "Computational Investigation of the Effects of gurney Flap on the Forward Flight Characteristics of Helicopter Rotors" is published in AIAA, 2007*
15. *Castino F. , R.Festa, C.F. Ratto, 'Stochastic modeling of wind velocities time series' Journal of Wind Engineering and Industrial Aerodynamics 74-76,(1998), 141-151*
16. *Chattot Design and Analysis of Wing/Winglet Combinations Including Viscous Effects at Low Speeds published in Journal of Aircraft 12 July 2005.*

17. *Chattot. "Effects of blade tip modifications on wind turbine performance using vortex model" published in Elsevier Computers & Fluids Journal Volume38, Issue7, August 2009, Pages 1405-1410.*
18. *Choudhury D.. Introduction to the Renormalization Group Method and Turbulence Fluent Inc. Technical Memorandum TM-107, 1993.*
19. *Christian Bak, Peter Fuglsang, Sørensen N.Niels, Helge, Aagaard Madsen, Wen Zhong Shen, Jens Nørkær Sørensen, Airfoil Characteristics for Wind Turbines, Risø National Laboratory,1999.*
20. *Chung C. W., Y. U. Sohn, J. B. Son, I. S. Park, Y. C. Kim, K. R. Kim, S. J. Kwon, Ch. H. Chun - Design of a 750 kW Direct-drive Wind Turbine generator System UNISON Industrial Co., LTD, 330-882,2004.*
21. *Colman J., J.Marañón di leo, J. S. Delnero, M. Martínez, U. Boldes and F. Bacchi. "Lift and drag coefficients behaviour at Low reynolds number in an airfoil with gurney flap submitted to a turbulent flow" published in latin american applied research 38 (2008).195-200*
22. *Corbus D. and M. Meadors. 'Small Wind Research Technical Report' NREL-October 2005.*
23. *Dahl S. Kristian, Peter Fuglsang, Design of the Wind Turbine Airfoil Family,Risø,1998*
24. *Dai J.C., Y.P.Hu, D.S. Liu, X. Long- Aerodynamic loads calculation and analysis for large scale wind turbine based on combining BEM modified theory with dynamic stall model - Renewable Energy 36 (2011) 1095.*
25. *Dam C.P. van, R. Chow, J.R. Zayas, D.E. Berg. "Computational Investigations of Small Deploying Tabs and Flaps for Aerodynamic*

- Load Control*” journal published in *IOP Science Publishing Journal of Physics: Conference Series 75 (2007) 012027*.
26. Douglas S. Cairns, J.C. Blockey, and Jon Ehresman , *Design and Feasibility of Active Control Surfaces on Wind Turbine Blade Systems* , AIAA 2008
 27. Ebert P.R , D.H. Wood, ‘*The near wake of a model horizontal-axis wind turbine at runaway*’ *Journal of Renewable Energy Vol 25 (2002), 41–54*
 28. Farmer Richard, Ralph Pike, gary Cheng, ‘*CFD analyses of complex flows*’, *Journal of Computers and Chemical Engineering 29 (2005) 2386–2403*
 29. Ferrer E and X Munduate. “*Wind turbine blade tip comparison using CFD*” is published in *Journal of Physics: Conference Series 75 (2007) 012005*.
 30. Ferudnreich K., K.Kaiser,A.P.Schaffarczyk,H.Winkler, B.stahl, “*Reynolds Number and roughness effects on thick airfoil for wind Turbines*”, *wind Engineering, volume 28, NO.5,2004*
 31. Franck Bertagnolio, Sørensen N.Niels and Jeppe Johansen, *Profile Catalogue for Airfoil Sections Based on 3D Computations*, Riso National Laboratory, 2006
 32. Gaunaa Mac & Johansen Jeppe “*Determination of the Maximum Aerodynamic Efficiency of Wind Turbine Rotors with Winglets*” is published in *IOP publishing Journal of Physics: Conference Series 75 (2007) 012006*.
 33. Gervois J.-L Hantrais and R. grenon “*Downward pointing winglet design and assessment within the M-DAW research project*”

- published in the Aeronautical Journal April 2009 Volume 113 NO 1142.*
34. *Glauert H., The Elements of Aerofoil and Airscrew Theory, Cambridge Press,1948*
 35. *Grant, M.Mo, X. Pan, P. Parkin, J. Powell, H. Reinecke, K. Shuang, F. Coton, D. Lee- An experimental and numerical study of the vortex laminents in the wake of an operational horizontal-axis, wind turbine- Journal of Wind Engineering and Industrial Aerodynamics 85 (2000) 177 189*
 36. *Habali S. M., I. A. Salehr, “Design and testing of small mixed airfoil wind turbine blades”, Renewable Energy, Vol. 6, No. 2, (1995), pp. 161- 169.*
 37. *Hansen M.O.L. , J.N. Sørensen, S. Voutsinas, N. Sørensen, H.Aa. Madsen, 'State of the art in wind turbine aerodynamics and aeroelasticity; Science direct –Elsevier Progress in Aerospace Sciences Vol4(2006),,285–330*
 38. *Hernamdez. J, Crespo. A, - Turbulence characteristics in wind turbine wakes –Journal of Wind Engineering and Industrial Aerodynamics (1996)-71-85*
 39. *Hossain A., P.R. Arora, A.A. Jaafar, A.K.M.P. Iqbal, M. Arifin “Lift Analysis of an Aircraft Model with and without Winglet” published in ICME07-FL-05.*
 40. *Howell Robert, Ning Qin, Jonathan Edwards, Naveed Durrani-Wind tunnel and numerical study of a small vertical axis wind turbine- Renewable Energy 35 (2010) 412–422*

41. Hussain Syed Altaf, V. Pandurangadu, K. Palanikumar, "Surface Roughness Analysis in Machining of gFRP Composites by Carbide Tool (K20)", *European Journal of Scientific Research*. ISSN 1450-216X Vol.41 No.1 (2010), pp.84-98
42. Inam Ilias Mohammad, Mohammad Mashud, Abdullah-Al-Nahian and S. M. S. Selim ,*Induced Drag Reduction for Modern Aircraft without Increasing the Span of the Wing by Using Winglet , International Journal of Mechanical & Mechatronics ,Vol: 10 ,(2007) AIAA-2001-2407*
43. Inam Mohammad Ilias, Mohammad Mashud, Abdullah-Al-Nahian and S. M. S. Selim.*Induced Drag Reduction for Modern Aircraft without Increasing the Span of the Wing by Using Winglet" Published in International Journal of Mechanical & Mechatronics IJMME-IJENS Vol: 10 No: 03,2001.*
44. Iradi S. Gómez, R. Steijl, g. N. Barakos, 'Development and Validation of a CFD Technique for the Aerodynamic Analysis of HAWT' *Journal of Solar Energy Engineering ASME AUGUST 2009, Vol. 131 / 031009-1*
45. Jang S. Cory, James C. Ross, Russell M. Cummings "Numerical investigation of an airfoil with a gurney flap" Is published in Elsevier *Aircraft Design, Volume 1, and Issue 2, June 1, (1998), pages 75-88.*
46. Jean-Jacques Chattot-*Helicoidal vortex model for wind turbine aeroelastic simulation Computers and Structures 85 (2007) 1072–1079*
47. Johansen Jeppe , Niels N. Sørensen, Mads Reck, Martin O.L.Hansen, Arne Stuermer, Jan Ramboer, CharlesHirsch,John

- Ekaterinaris, Spyros Voutsinas and Yannis Perivolaris, KNOW-BLADE Task-3.3 report; Rotor Blade Computations with 3D Vortex generators, Riso National Laboratory, 2005*
48. *Johnson L Gary, Wind Energy Systems, Prentice –Hall, 1985.*
49. *Jun Zhu, gao Zhenghong, Zhan Hao, Bai Junqiang, “A High-speed Nature Laminar Flow Airfoil and Its Experimental Study in Wind Tunnel with Nonintrusive Measurement Technique”, Chinese Journal of Aeronautics 22(2009) 225-229.*
50. *Jung Nam Sung , Tae-Soo No, Ki-Wahn Ryu- Aerodynamic performance prediction of a 30 kW counter-rotating wind turbine system- Renewable Energy 30 (2005) 631–644*
51. *Khalfallaha, Aboelyazied M. Koliubb, “Effect of dust on the performance of wind turbines”, Desalination 209 (2007) 209–220*
52. *Knight & Carver Wind group, Sweep-Twist Adaptive Rotor Blade: Final Project Report, SANDIA, 2/1/2010*
53. *Koki Kishinamia, Hiroshi Taniguchib, Jun Suzukia, Hiroshi Ibanoc, Takashi Kazunoud, Masato Turuhamie, ‘Theoretical and experimental study on the aerodynamic characteristics of a horizontal axis wind turbine’ Journal of Energy 30 (2005) 2089–2100*
54. *Launder B. E.and D. B. Spalding. Lectures in Mathematical Models of Turbulence. Academic Press, London, England, 1972.*
55. *Lazim Mat Tholudin, Shabudin Mat, Huong Yu Saint Acta Polytechnica.’ Computational Fluid Dynamic Simulation (CFD) and Experimental Study on Wing-external Store Aerodynamic Interference of a Subsonic Fighter Aircraft’Vol. 44, 2004.*

56. Liu F. and A. Jameson, 'Multigrid Euler Calculations For Three-dimensional Cascades' AIAA January 8-11, 1990
57. Madsen AA. Helge, Peter Fuglsang, Ioannis Antoniou, Niels N. Sørensen Validation of a Wind Tunnel Testing Facility for Blade Surface Pressure Measurements, Risø National, 1998
58. Manela A. - Sound generated by a vortex convected past an elastic sheet - *Journal of Sound and Vibration* 330 (2011) 416–430
59. Manish K. Singh, K. Dhanalakshmi and S. K. Chakrabartty. "Navier-Stokes Analysis of Airfoils with gurney Flap" published by Nal Publications.
60. Mark D. Maughmer and gotz Bramesfeld. "Experimental Investigation of gurney Flaps" is published in *JOURNAL OF AIRCRAFT* Vol. 45, No. 6, November–December 2008.
61. Menter F. R. Two-Equation Eddy-Viscosity Turbulence Models for Engineering Applications. *AIAA Journal*, 32(8) (1994), 1598-1605, August
62. Merchant J., J. Matthew Bondy, Kenneth W. Van Treuren. "Wind Tunnel Analysis Of A Wind Turbine With Winglets". ASME, 2008.
63. Michael P. Kinzel and Mark D. Maughmer. "Numerical Investigation on the Aerodynamics of Oscillating Airfoils with Deployable gurney Flaps" is published in *AIAA JOURNAL* Vol. 48, No. 7, July 2010.
64. Miyakozawa Tomokazu, Robert E. Kielb, Kenneth C. Hall 'The Effects of Aerodynamic Asymmetric Perturbations on Forced Response of Bladed Disks' *Journal of Turbomachinery* ASME October 2009, Vol. 131 / 041008-1
65. Modeling. Fluent Inc. Technical Memorandum TM-107, 1993.

66. Myose Y. Roy, Jan-Christopher Lietsche, Dieter Scholz, Hartmut Zingel, Shigeo Hayashibara, Ismael Heron.-Flow Visualization Study on the Effect of a gurney Flap in a Low Reynolds Number Compressor Cascade” is published in AIAA (2006)-7809.
67. Nelson C. Robert, Thomas C. Corke and Hesham Othman, 'A Smart Wind Turbine Blade Using Distributed Plasma Actuators for Improved Performance' AIAA January 7-10, 2008,
68. Ng.K.C, Yusoff.M.Z, Yusaf.T.F and Hussein.I, 'Development status of indigenous Computational fluid dynamics software for arbitrary complex geometry' Journal - The Institution of Engineers, Vol. 66, December 2005.
69. Ohya Y. H. Kiharaa K. Sato K. Abea, M. Nishidab, A. Sakuraia- Experimental and numerical investigations of flow fields behind a small wind turbine with a flanged diffuser Journal of Wind Engineering and Industrial Aerodynamics 93 (2005) 951 – 970
70. Overgaard L.C.T., E. Lund, 'Structural collapse of a wind turbine blade. Part B: Progressive interlaminar failure models ' Composites- Elsevier Vol 41 (2010), 271–283
71. Patel Mukund R, Wind and Solar Power Systems, CRC Press, 1999
72. Patrick H. Reisenthel, John F. Love, Daniel J. Lesieutre, and Robert E. Childs, 'Cumulative global Metamodels with Uncertainty a Tool for Aerospace Integration' AIAA-2003-0352.
73. Peng fei Liu, A computational hydrodynamics method for horizontal axis turbine Panel method modeling migration from propulsion to turbine energy, Journal of Energy 35(2010)2843-2851.

74. Peng fei Liu, *A computational hydrodynamics method for horizontal axis turbine Panel method modeling migration from propulsion to turbine energy*, *Journal of Energy* 35(2010)2843-2851
75. Pilmoor M., W.J. Crowther and N.J. Wood; *Development of a Dynamic Wind Tunnel Model for Demonstration of Flow Control Maneuver Effectors' American Institute of Aeronautics and Astronautics* 2006
76. Ralf messing and markus j. Kloker. "Investigation of suction for laminar flow control of three-dimensional boundary layers" published in *J. Fluid Mech.* vol. 658, pp. 117–147.
77. Ren Nianxin, Ou Jinping, "Dust Effect on the Performance of Wind Turbine Airfoils", *J. Electromagnetic Analysis & Applications*, 1(2009), 102-107
78. Rhoads H., J. VandenBosche, T. McCoy, and A. Compton- *Comparison of Projections to Actual Performance in the DOE-EPRI Wind Turbine Verification Program- the American Wind Energy Association s WindPower 2000 Palm Springs, California April 30 May 5, 2000*
79. Robert Howell, Ning Qin, Jonathan Edwards, Naveed Durrani, *Wind tunnel and numerical study of a small vertical axis wind turbine Journal of Renewable Energy* 35 (2010) 412–422.
80. Rodrigo J. Sanz, J. van Beeck, g. Dezsó " -Weidinger- *Wind tunnel simulation of the wind conditions inside bidimensional forest clear-cuts. Application to wind turbine siting- Journal of Wind Engineering and Industrial Aerodynamics* 95 (2007) 609 – 634

81. Rosen A. and Y. Sheinman- *The average output power of a wind turbine in a turbulent wind –Journal of Wind Engineering and Industrial Aerodynamics. 51 (1994) 287-302*
82. Schatz M., B. Gaunther and F. Thiele. “Computational Modeling of the Unsteady Wake behind Gurney-Flaps” published in AIAA-(2004)-2417.
83. Selig M.S. Giguère, J.L. Tangler, *Blade Design Trade-Offs Using Low-Lift Airfoils for Stall-Regulated HAWTs • NREL/CP-500-26091 April 1999*
84. Sicot C., I. P. Devinant, S. Loye r, J. Hureau- *Rotational and turbulence effects on a wind turbine blade. Investigation of the stall mechanism - Journal of Wind Engineering and Industrial Aerodynamics 96 (2008) 1320 – 1331.*
85. Smith M. J., N. Komerath, R. Ames, O. Wong J. Pearson. “Performance Analysis of a Wing with Multiple Winglets” published in the AIAA-2001-2407.
86. Sohn Y. U., Ch. H. Chun, Y. C. Kim, C. W. Chung, Y. H. Kim, K. S. Han, *Blade Design of a 750 kW Direct-drive Wind Turbine generator System, UNISON Industrial Co., LTD, 330-882, 2005*
87. Somer, D. M., 2004, S816, S817 and S818 airfoils: October 1991-July 1992, Report SR-500-36333, National Renewable Energy Laboratory, Golden, Co.
88. Sørensen N. Niels , *3D CFD computations of transitional flows using DES and a correlation based transition model, Risø, 2009*
89. Tangler J. L. - *NREL Airfoil Families for HAWTs AWEA- 1995*

90. Tetsuya Kogaki, Hikaru Matsumiya, Kaori Kieda, Naofumi Yoshimizu and Yuusuke Yamamoto -Performance improvement of airfoils for Wind turbines by the modified Vortex generator - European Community Wind Energy Conference (Madrid), 2004.
91. Tholudin Mat Lazim, Shabudin Mat, Huong Yu Saint Acta Polytechnica.' Computational Fluid Dynamic Simulation (CFD) and Experimental Study on Wing-external Store Aerodynamic Interference of a Subsonic Fighter Aircraft'Vol. 44 2004.
92. Thumthae and Tawit Chitsomboon- Optimal Pitch for Untwisted Blade Horizontal Axis Wind Turbine - The 2nd Joint International Conference on "Sustainable Energy and Environment (2006)" B-034 (O) 21-23
93. Thumthae and Tawit Chitsomboon" "Optimal angle of attack for untwisted blade wind turbine published in Renewable Energy Volume 34, Issue 5, May 2009.
94. Thumthae, Tawit Chitsomboon -Optimal angle of attack for untwisted blade wind turbine-Renewable Energy 34 (20 09) 1279–1284
95. Timmer W.A. and R.P.J.O.M. van Rooij, Summary of the Delft University Wind Turbine Dedicated Airfoils, AIAA-2003
96. Tomokazu Miyakozawa, Kiel .E.Robert, Hall C.Kenneth 'The Effects of Aerodynamic Asymmetric Perturbations on Forced Response of Bladed Disks' Journal of Turbomachinery, ASME ,October 2009, Vol. 131 / 041008-1
97. Tony Burton, David Sharpe, Ervin Bossanyi Wind Energy Handbook, John Wiley & Sons, Ltd, 2001.

98. *Vanden Bosche .J,McNiff.B,Smith.B, Power Performance Testing Activity in TheDOE-EPRI Turbine Verification Program 2000.*
99. *Velte C M, M O L Hansen and D Cavar, 'Flow analysis of vortex generators on wing sections by stereoscopic particle image velocimetry measurements', IOP Publishing Environmental Research 2008*
100. *Vermeer L.J., J.N. Sorensen, A. Crespo, Wind turbine wake aerodynamics, Science direct -Progress in Aerospace Sciences Vol 39 (2003) 467–510.*
101. *Versteeg.H K and Malalasekera.W An Introduction to Computational Fluid Dynamics 2007.*
102. *Wang F., L. Baia, J. Fletcherb, J. Whitefordc, D. Cullenc- Development of small domestic wind turbine with scoop and prediction of its annual power output- Renewable Energy 33 (2008) 1637 – 1651*
103. *Watters Sibuet and Masson Christian “Recent advances in modeling of wind turbine wake vortical structure using a differential actuator disk theory” published in IOP publishing Journal of Physics: Conference Series 75 (2007) 012037.*
104. *Whale J., C.G. Anderson, R. Bareiss, S. Wagner- An experimental and numerical study of the vortex structure in the wake of a wind turbine- Journal of Wind Engineering and Industrial Aerodynamics 84.2000*
105. *Wind energy Technology-Course Material, Centre of wind Energy Technology, 2010*

106. Wright A.K., D.H.Wood-*The starting and low wind speed behavior of a small horizontal axis wind turbine- Journal of Wind Engineering and Industrial Aerodynamics* 92 (2004)1265–1279.
107. Yang Shuchi, Shijun Luo, Feng Liu, ‘*Computation of the Flows over Flapping Airfoil by the Euler Equations*’ AIAA, Jan. 10-13, 2005
108. Yang Shuchi, Shijun Luo, Feng Liu, *Trailing-Edge Flow about Unstalled Plunging Airfoil Computed by Euler Method, 36th AIAA Fluid Dynamics Conference and Exhibit, San Francisco, CA, Jun. 5-8, 2006*
109. Yen Shun C. a.,1, Lung-C. Huang b,2, “*Reynolds number effects on flow characteristics and aerodynamic performances of a swept-back wing*”, *Prn:28/10/2010; 14:16*) P.1 (1-10)
110. Yoo Neung-Soo “*Effect of the gurney Flap on a NACA 23012 Airfoil*” is published in *KSME International Journal, Vol. 14, No.9, 2000, pp. 1013-1019,*
111. Zwaba S Ryszard - *Comparison of the influence of different air-jet vortex generators on the separation region -Aerospace Science and Technology-2010*

1. <http://economictimes.indiatimes.com/news/news-by-industry/energy/power/electricity-for-all-by-2012-power-minister/articleshow/3836381.cms>
2. <http://economictimes.indiatimes.com/news/news-by-industry/energy/power/electricity-for-all-by-2012-power-minister/articleshow/3836381.cms> Report of Indian wind energy outlook.
3. <http://www.autospeed.com>
4. <http://www.aerospaceweb.org>
5. <http://www.bakker.org>
6. http://www.ewea.org/fileadmin/swf/factsheet/4_climate.pdf
7. <http://www.gwec.net/index.php?id=168> Report of Indian wind energy outlook.
8. [http://www.gwec.net/index.php?id=30&no_cache=1&tx_ttnews\[tt_news\]=279&tx_ttnews\[backPid\]=97&cHash=01e9c85e9f](http://www.gwec.net/index.php?id=30&no_cache=1&tx_ttnews[tt_news]=279&tx_ttnews[backPid]=97&cHash=01e9c85e9f) Report of Indian wind energy outlook.
9. [http://www.gwec.net/index.php?id=30&no_cache=1&tx_ttnews\[tt_news\]=279&tx_ttnews\[backPid\]=97&cHash=01e9c85e9f](http://www.gwec.net/index.php?id=30&no_cache=1&tx_ttnews[tt_news]=279&tx_ttnews[backPid]=97&cHash=01e9c85e9f) Report of Indian wind energy outlook.
10. <http://www.lmwindpower.org>
11. <http://www.mnre.gov.in/pdf/mnre-paper-direc2010-25102010.pdf>



LIST OF PUBLICATIONS

Journals

- C.Rajendran, G.Madhu. A CFD Based Multi Body Dynamics approach in Horizontal Axis wind Turbine, International Journal of Dynamics of Fluids (IJDF), volume 6, no. 2, pp 219-230, 2010.
- C.Rajendran, G.Madhu, P.S.Tide, K.Kandavel. Aerodynamic performance analysis of horizontal axis wind turbine using CFD technique, European Journal of Scientific Research (Submitted)

Patents

- C.Rajendran , High Efficiency Aerotowerfoil for Horizontal Axis Wind Mills, The Patent office Journal Part I Vol I, 22/7/2011, Page no 12163

Conferences

- M.Thiagarajan,C.Rajendran. Numerical Investigation on a Low Speed Wind Turbine Blade Performance Enhancement using Vortex Generator Concept, RTME 2011, Sri Ramakrishna Engineering College, Coimbatore.

Curriculum Vitae



Rajendran.C

S/o N. Chinnaswamy

193, Thirumalai Naicken Palayam

Jothipuram P.O, Coimbatore 641047

Email: rajpcra@gmail.com

Rajendran.C was born on 5th May 1968 at Coimbatore, Tamil Nadu, in India. He completed his schooling in 1983 at Pioneer Mills High School, Jothipuram. He Graduated in Mechanical Engineering from Kumaraguru College of Technology, Coimbatore under Bharathiyar University in the year 1989 and took his Masters degree in Energy Engineering in the year 2005 from Anna University, Chennai. He qualified as Member Mechanical in the energy auditing team approved by Tamil Nadu Electricity Board. He served as an external faculty member, empanelled by the **Petroleum Conservation Research Association under the ministry of Petroleum and Natural Gas, Govt. of India**. He has been awarded with the **BEST FACULTY Award** by the then **Minister for Petroleum and Natural Gas, Govt. of India in the year 2004**. He has more than a Decade of experience in the industries at various cadres. He is in the field of teaching for the last ten years. He is herewith submitting his thesis entitled *“Techniques for Enhancing Wind Energy Generation –A CFD Based Multibody Dynamics Approach in Horizontal Axis Wind Turbines”* in September 2011.